Steady-state behaviour of reduced dynamic systems with local nonlinearities

STEADY-STATE BEHAVIOUR OF REDUCED DYNAMIC SYSTEMS WITH LOCAL NONLINEARITIES

R.H.B. FEY

STEADY-STATE BEHAVIOUR OF REDUCED DYNAMIC SYSTEMS WITH LOCAL NONLINEARITIES

ISBN 90-9004680-1

Druk: Febodruk, Enschede

STEADY-STATE BEHAVIOUR OF REDUCED DYNAMIC SYSTEMS WITH LOCAL NONLINEARITIES

PROEFSCHRIFT

ter verkrijging van de graad van doctor
aan de Technische Universiteit Eindhoven
op gezag van de Rector Magnificus, prof.dr. J.H. van Lint,
voor een commissie aangewezen door het College van Dekanen
in het openbaar te verdedigen
op dinsdag 14 januari 1992 om 16.00 uur

door

ROBERTUS HENRICUS BARBARA FEY

geboren te Eindhoven

Dit proefschrift is goedgekeurd door de promotoren

prof.dr.ir. D.H. van Campen
prof.dr. R.M.M. Mattheij

Copromotor

dr.ir. A. de Kraker

Voor mijn ouders

Contents

Samenvatting

Het onderwerp van dit proefschrift betreft het lange termijn gedrag van complexe dynamische systemen met lokale niet-lineariteiten die worden geëxciteerd door een periodieke externe belasting.

Ter verkrijging van nauwkeurige informatie over verplaatsingen, rekken en spanningen is het vaak noodzakelijk om m.b.v. de eindige elementen methode grote modellen met veel vrijheidsgraden op te stellen. Het bepalen van het lange termijn gedrag op basis van een niet-lineair model met veel vrijheidsgraden is zeer kostbaar. Door toepassing van een component mode synthese methode gebaseerd op free-interface eigenmodes en residuele flexibiliteitmodes wordt het aantal vrijheidsgraden van de lineaire componenten van een systeem met lokale niet-lineariteiten gereduceerd. De nauwkeurigheid van berekeningen uitgevoerd op basis van het gereduceerde model kan worden gecontroleerd door onderzoek van het frequentiespectrum van de externe belasting minus de (interne) belasting veroorzaakt door de lokale niet-lineariteiten en door onderzoek van de invloed van hogere, weggelaten eigenmodes op dit frequentiespectrum.

Het lange termijn gedrag van een niet-lineair dynamisch systeem kan periodiek, quasi-periodiek of chaotisch van aard zijn. Periodieke oplossingen worden efficiënt berekend door het oplossen van een tweezijdig grenswaardeprobleem door toepassing van een tijdsdiscretisatiemethode (eindige differentiemethode). Een belangrijk voordeel van deze methode is dat zowel stabiele als (zeer) instabiele oplossingen probleemloos kunnen worden bepaald. D.m.v. een vertraagde correctiemethode kan de globale discretisatiefout in de oplossing worden geschat en kan de nauwkeurigheid van de oplossing worden verbeterd. Hoe de periodieke oplossing wordt beïnvloed ten gevolge van een verandering in een ontwerpvariabele van het systeem kan worden onderzocht door toepassing van een "path following" techniek. De lokale stabiliteit van een periodieke oplossing wordt onderzocht met behulp van Floquet theorie. Op takken met periodieke oplossingen kunnen een drietal typen lokale bifurcaties worden aangetroffen en wel de cyclic fold bifurcatie, de flip bifurcatie en de Neimark bifurcatie. Lange termijn oplossingen worden tevens geanalyseerd via standaard numerieke integratie. Door berekening van Lyapunov exponenten en de daarvan afgeleide Lyapunov dimensie wordt het karakter van de lange termijn oplossing (periodiek, quasi-periodiek of chaotisch) geïdentificeerd.

De gepresenteerde technieken worden toegepast op een harmonisch geëxciteerd balksysteem met verschillende niet-lineaire ondersteuningen zoals een verstijvende veer, een eenzijdig verstijvende veer en een eenzijdig lineaire veer. Superharmonische, subharmonische en interne resonanties worden berekend en genoemde bifurcaties worden veelvuldig aangetroffen. In de systemen met een eenzijdig lineaire veer worden drie verschillende transities naar chaos aangetroffen: een transitie via periodeverdubbeling, een intermitterende transitie en een "quasi-periodic-locked-chaotic" transitie.

Summary

The subject of this thesis is the long term behaviour - also called steady-state behaviour - of complex dynamic systems with local nonlinearities, which are excited by periodic, external loads.

Accurate information about displacements, strains and stresses often requires finite element models with many elements and thus many degrees of freedom. The determination of the steady-state behaviour for a nonlinear model with many degrees of freedom is very expensive. By applying the component mode synthesis method based on free-interface eigenmodes and residual flexibility modes the number of degrees of freedom of the linear components of a system with local nonlinearities is reduced. The accuracy of results obtained with the reduced model can be checked by investigating the frequency spectrum of the external loads minus the internal loads caused by the local nonlinearities and by investigating the influence of the deleted (higher) eigenmodes on this frequency spectrum.

The steady-state behaviour of a nonlinear dynamic system can have a periodic, quasi-periodic or a chaotic character. Periodic solutions will be calculated efficiently by solving a two-point boundary value problem by applying a time discretisation method (finite difference method). An important advantage of this method is the fact that stable as well as (very) unstable solutions can be determined easily. The global discretisation error in the solution can be estimated and the accuracy of the solution can be improved by means of a deferred correction method. How the periodic solution is influenced by a change in a so-called design variable of the system can be investigated by applying a path following technique. The local stability of a periodic solution is investigated using Floquet theory. On the branches of periodic solutions three types of local bifurcations can be found, namely the cyclic fold bifurcation, the flip bifurcation and the Neimark bifurcation. The steady-state behaviour also has been investigated by means of standard numerical integration. In this case the character of the steady-state behaviour (periodic, quasi-periodic or chaotic) is identified by calculation of the Lyapunov exponents and the Lyapunov dimension.

The methods presented are applied to a harmonically excited beam system with different nonlinear supports, such as a stiffening spring, a one-sided stiffening spring, a one-sided linear spring. Superharmonic, subharmonic and internal resonances are evaluated and the bifurcations mentioned above are met frequently. In systems with a one-sided linear spring three transitions to chaos are observed: a transition via period doubling, intermittency and a quasi-periodic-locked-chaotic transition.

Notation

General notation

a,A	Scalar
a	Column matrix
a_i	Scalar on row i of column matrix a
A	Matrix
a_i	Column i of matrix A
A_{ij}	Scalar on row i and column j of matrix A
$\ulcorner A \lrcorner$	Diagonal matrix
$\ulcorner a_i \lrcorner$	Diagonal matrix $\ulcorner A \lrcorner$ with scalar a_i on row i and column i

Greek lower-case letters represent scalars or column matrices
Greek upper-case letters represent matrices

j	Complex unity constant
$\Re(a)$	Real part of a
$\Im(a)$	Imaginary part of a
$\bar{a}$	Conjugate of a
0	Null column matrix
O	Null matrix
I	Unit matrix
Q	Orthonormal matrix
U, W	Upper triangular matrix
δa	Infinitesimally small perturbation of a
$\|a\|$	Absolute value of a
$\|\|a\|\|$	Euclidian norm of a
a^t, A^t	Transposed of column matrix a, transposed of matrix A
A^{-1}	Inverse of matrix A
rank A	Rank of matrix A
$< A >$	The linear subspace spanned by the columns of matrix A
$\dot{a}$	First time derivative of a
$\ddot{a}$	Second time derivative of a
a'	First dimensionless time derivative of a
a''	Second dimensionless time derivative of a
$a^{(k)}$	k-th dimensionless time derivative of a

Scalars

c_q	Convergence ratio for dof q
$c_{r,k,m}$	Increment for r in corrector step m of pf-step k
e_q	Mean global discretization error for dof q
f_c	Cut-off frequency
f_e	Frequency of external load
f_p	Frequency of periodic solution
f_r	Frequency of response
n_q	Number of dof of the system
n_y	Number of boundary dof of the system
n_τ	Number of time discretization points
$p_{r,k}$	Increment for r in predictor step of pf-step k
r	Design variable
t	Time
t_t	The time needed for transients to damp out
A	Area of cross-section
D_H	Hausdorff dimension
D_λ	Lyapunov dimension
E	Modulus of elasticity
I	Second moment of area
N_c	Number of linear components
T_e	Period of external load
T_p	Period of periodic solution
T_r	Period of response
β_1, β_2	Path following control parameters
ϵ_z	Convergence control parameter
η_i	i-th characteristic exponent
λ_i	i-th Lyapunov exponent
μ_i	i-th Floquet multiplier
ρ	Mass density
σ_k	Stepsize in the predictor step of pf-step k
τ	Dimensionless time
$\Delta\tau$	Time increment between two discretization points
ϕ	Phase angle of external load
ϕ_e	Phase angle of external load at t = 0
ϕ_P	Phase angle of Poincaré section
ω	Angular frequency
ω_c	Angular cut-off frequency

The following scalars are component dependent and have to be provided with the superscript [c]:

n_d	Number of deleted elastic free-/fixed-interface eigenmodes of the component
n_k	Number of kept elastic free-/fixed-interface eigenmodes of the component
n_p	Number of reduced dof of the component
n_x	Number of dof of the component
n_B	Number of boundary dof of the component
n_E	Rank of the stiffness matrix K of the component
n_G	Number of non-interface dof of the component
n_H	Number of interface dof of the component
n_I	Number of internal dof of the component
n_R	Number of rigid body modes of the component
ξ_i	Dimensionless damping factor of free-interface eigenmode i
ω_i	Angular eigenfrequency of free-interface eigenmode i
ω_i^{fx}	Angular eigenfrequency of fixed-interface eigenmode i

Column matrices

$c_{z,k,m}$	$((n_q * n_\tau) * 1)$	Increment for z in corrector step m of pf-step k
f_{ex}	$(n_q * 1)$	External load acting on the system
f_{in}	$(n_q * 1)$	Displacement and velocity dependent load
$f^*_{nl} = -f_{nl}$	$(n_q * 1)$	Loads caused by local nonlinearities
f_{yex}	$(n_q * 1)$	External load acting on the boundary dof of the system
f^*_{yml}	$(n_y * 1)$	Interface loads caused by adjacent local nonlinearities
g	$(n_q * 1)$	Equations of motion of the system
Δg	$((n_q * n_\tau) * 1)$	$0(\Delta\tau^2)$ local discretization error in the equations of motion
h	$((n_q * n_\tau) * 1)$	Discretized equations of motion
$p_{z,k}$	$((n_q * n_\tau) * 1)$	Increment for z in predictor step of pf-step k
q	$(n_q * 1)$	Dof of the system
δq	$(n_q * 1)$	Perturbation of q
s	$(2n_q * 1)$	State of the system
δs	$(2n_q * 1)$	Perturbation of s
y	$(n_y * 1)$	Boundary dof of the system
z, z_s, z_f	$((n_q * n_\tau) * 1)$	Discretized periodic solution, $0(\Delta\tau^2)$, $0(\Delta\tau^4)$
Δz_s	$((n_q * n_\tau) * 1)$	$0(\Delta\tau^2)$ global discretization error in the discretized periodic solution
ε_g	$(n_q * 1)$	Local discretization error in the equations of motion
$\varepsilon_{q'}$	$(n_q * 1)$	Local discretization error in the velocities
$\varepsilon_{q''}$	$(n_q * 1)$	Local discretization error in the accelerations

The following column matrices are component dependent and have to be provided with the superscript [c]:

f	$(n_x * 1)$	Loads acting on the component
f_{ex}	$(n_x * 1)$	External loads acting on the component
f_p	$(n_p * 1)$	Reduced column of loads
f^*_l	$(n_x * 1)$	Interface loads caused by adjacent linear components
f^*_{nl}	$(n_x * 1)$	Interface loads caused by local nonlinearities
p	$(n_p * 1)$	Reduced dof
x	$(n_x * 1)$	Dof referring to a set of local base vectors
y_B	$(n_B * 1)$	Boundary dof referring to a set of global base vectors
φ	$(n_x * 1)$	Free-interface eigenmode
φ^{fx}_G	$(n_G * 1)$	Fixed-interface eigenmode

Matrices

A_δ	$(2n_q * 2n_q)$	System matrix, resulting after linearization around a periodic solution
B_q	$(n_q * n_q)$	Damping matrix of linear system, non-negative definite
B_δ	$(n_q * n_q)$	Damping matrix of the system, resulting after linearization around a periodic solution
J	$((n_q * n_\tau) * (n_q * n_\tau))$	Jacobian
K_q	$(n_q * n_q)$	Stiffness matrix of linear system, non-negative definite
K_δ	$(n_q * n_q)$	Stiffness matrix of the system, resulting after linearization around a periodic solution
M_q, M_δ	$(n_q * n_q)$	Mass matrix of the system, positive definite
Θ	$(2n_q * 2n_q)$	Fundamental matrix
Θ_η	$(2n_q * 2n_q)$	Natural matrix logarithm of the monodromy matrix
Θ_μ	$(2n_q * 2n_q)$	Monodromy matrix
Ψ_η	$(2n_q * 2n_q)$	Matrix with eigenmodes of Θ_η
Ψ_μ	$(2n_q * 2n_q)$	Matrix with eigenmodes of Θ_μ

The following matrices are component dependent and have to be provided with the superscript [c]:

B	$(n_x * n_x)$	Damping matrix, non-negative definite
B_p	$(n_p * n_p)$	Reduced damping matrix, non-negative definite
G	$(n_x * n_x)$	Flexibility matrix of rank n_E
G_E	$(n_x * n_x)$	Elastic flexibility matrix of rank n_E
H	$(n_x * n_x)$	Matrix of frequency response functions
K	$(n_x * n_x)$	Stiffness matrix, non-negative definite
K_p	$(n_p * n_p)$	Reduced stiffness matrix of the component, non-negative definite
M	$(n_x * n_x)$	Mass matrix, positive definite
M_p	$(n_p * n_p)$	Reduced mass matrix, positive definite
R_H	$(n_x * n_x)$	High frequency residue matrix
R_L	$(n_x * n_x)$	Low frequency residue matrix
T	$(n_x * n_q)$	Component assemblage matrix
T_1	$(n_x * n_p)$	Ritz reduction matrix, dynamic component mode set
T_1^{D1}	$(n_x * n_p)$	Dynamic component mode set with free-interface eigenmodes
T_1^{D2}	$(n_x * n_p)$	Dynamic component mode set with fixed-interface eigenmodes
T_2	$(n_p * n_p)$	Regular transformation matrix, brings boundary dof explicitly in reduced dof set
T_3	$(n_p * n_p)$	Local-global vector base transformation matrix, regular
T_4	$(n_p * n_q)$	Matrix which localizes reduced component dof p in q
T^S	$(n_x * (n_B + n_R))$	Statically complete component mode set
Φ	$(n_x * n_x)$	Matrix of free-interface eigenmodes

Φ^{fx}	$(n_G * n_G)$	Matrix of fixed-interface eigenmodes
Φ_d	$(n_x * n_d)$	Matrix of deleted elastic free-interface eigenmodes
Φ_d^{fx}	$(n_G * n_d)$	Matrix of deleted fixed-interface eigenmodes
Φ_k	$(n_x * n_k)$	Matrix of kept elastic free-interface eigenmodes
Φ_k^{fx}	$(n_x * n_k)$	Matrix of kept fixed-interface eigenmodes
Φ^A	$(n_x * (n_E - n_I))$	Matrix of attachment modes
Φ^{C1}	$(n_x * (n_E - n_I))$	Matrix of (redundant) constraint modes defined for $\mathcal{V}$ set
Φ^{C2}	$(n_x * n_B)$	Matrix of constraint modes defined for $\mathcal{B}$ set
Φ^E	$(n_x * n_E)$	Matrix of elastic free-interface eigenmodes
Φ^F	$(n_x * n_B)$	Matrix of flexibility modes
Φ^G	$(n_x * n_B)$	Matrix of residual flexibility modes
Φ^M	$(n_x * n_R)$	Matrix of inertia relief modes
Φ^R	$(n_x * n_R)$	Matrix of rigid body modes
$\ulcorner \Xi \lrcorner$	$(n_x * n_x)$	Matrix with dimensionless damping factors of free-interface component
$\ulcorner \Omega \lrcorner$	$(n_x * n_x)$	Matrix with angular eigenfrequencies of free-interface component
$\ulcorner \Omega^{fx} \lrcorner$	$(n_x * n_x)$	Matrix with angular eigenfrequencies of fixed-interface component

Chapter 1

Introduction

In many cases the performance of a mechanical system depends on its dynamic behaviour, which can be defined as the time dependent response of the system caused by internal or external influences. In this thesis attention is focused on long term dynamic behaviour of mechanical systems with local nonlinearities excited by periodic loads.

Mechanical systems consisting of linear components and local nonlinearities are frequently met in engineering practice. From a spatial point of view, these local nonlinearities constitute only a small part of the mechanical system. However, their presence can have important consequences for the overall dynamic behaviour. The local nonlinearities considered here are assumed to originate from physically and not from geometrically nonlinear behaviour; examples of these local nonlinearities are nonlinear elastic springs, nonlinear viscous dampers, dry friction and backlash. Local nonlinearities can be introduced deliberately by the designer to avoid excessively high responses or stresses; examples of such applications are nonlinear springs supporting a piping system in a chemical plant and dry friction hinges connecting parts of the exhaust system of a road vehicle. On the other hand local nonlinearities can be undesirable, for example dry friction and backlash phenomena in certain connections.

The dynamic behaviour of a system can be predicted using mathematical models for system and excitation. In this thesis spatially discretized models will be used as an idealization of continuous models. The behaviour in space and time of such a model is described by a finite number of *degrees of freedom* (dof) referring to a fixed co-ordinate system. Basically there are two approaches by which a discrete model can be obtained:

1. *The theoretical approach.*
   If the physical and geometrical properties of a system are explicitly known, a model can be derived using Lagrange's equations of motion. The Finite Element Method (FEM) in conjunction with the digital computer enables the automatic derivation of these equations for (almost) any mechanical system.

2. *The experimental approach.*
   If the qualitative properties of an existing system are known, but it is not possible to quantify certain system parameters theoretically, an experimental approach can be

followed. Experimental data can be used to estimate the unknown system parameters by application of identification techniques. Experiments can be expensive and dangerous.

Actually both approaches should not be considered separately. In many cases a theoretical model is analysed to verify if the design of a (new) mechanical system satisfies requirements with regard to its dynamic behaviour. Usually the design and its model will be modified several times before the design will be accepted. Then a prototype can be build and experiments can be carried out to verify, if measured and calculated data match sufficiently accurate. If this is not the case, the model could be improved using an experimental approach.

Under the assumptions that no constraints among the system dof $q(t)$ exist, system properties are independent of time t and local nonlinearities expose only physically nonlinear behaviour, i.e. displacements and rotations are assumed to remain small, so that only vibrations around a static equilibrium position need to be considered, Lagrange's equations of motion will result in:

$$M_q\ddot{q}(t) + f_{in}(\dot{q}(t), q(t)) = f_{ex}(t) \tag{1.1}$$

M_q is the positive definite mass matrix, f_{ex} is the column matrix with external loads and f_{in} is the column matrix with displacement dependent and velocity dependent forces (a list of symbols, used in this thesis, is given under the header Notation at the beginning of this thesis). In a linear model of a mechanical system moreover linearly elastic and linearly viscous material behaviour is assumed. In case of a linear system the equations of motion (1.1) simplify to:

$$M_q\ddot{q}(t) + B_q\dot{q}(t) + K_q q(t) = f_{ex}(t) \tag{1.2}$$

B_q and K_q are the damping matrix and the stiffness matrix respectively, which are both non-negative definite. The modal parameters of (1.2) can be estimated experimentally by the well-developed modal analysis technique (LMS International [1990]). The experimental identification of parameters in nonlinear systems is a rapidly growing area of research. Hence it is expected, that the possibilities for an experimental approach of systems, consisting of linear components and local nonlinearities, will grow in the future.

In many applications mechanical systems are loaded by harmonic, or more general, continuous periodic external loads:

$$f_{ex}(t) = f_{ex}(t + 1/f_e) = a_0 + \sum_{k=1}^{\infty}[a_k \cos k(2\pi f_e t + \phi_e) + b_k \sin k(2\pi f_e t + \phi_e)] \tag{1.3}$$

In this equation f_e is the frequency of the external load and ϕ_e is the phase angle of the external load at $t = 0$. Some typical periodic excitation sources are engines, pumps and rotating mass unbalances. Now the *state* $s(t)$ of the system is introduced: it is defined by the position of the system and its first time derivative:

$$s(t) = \begin{bmatrix} q(t) \\ \dot{q}(t) \end{bmatrix} \tag{1.4}$$

The *augmented state* is formed by $s(t)$ and $\phi(t)$, the phase angle of the excitation:

$$\phi(t) = 2\pi f_e t + \phi_e \tag{1.5}$$

The state $s(t)$ (also called *response*, *solution*, *flow* or *trajectory*), of a system under periodic excitation (1.1) is fully determined by the initial augmented state of the system, i.e. the augmented state specified at one point in time. Under the assumption that the response of a periodically excited nonconservative dynamic system remains bounded, this response undergoes two stages. In the first transient stage the response will be irregular. After the transient response has damped out, a regular response will be reached representing long term behaviour, also called *steady-state* behaviour.

The long term behaviour or steady-state behaviour of a damped linear system is unique and periodic with the same period as the excitation. Periodic solutions of (1.2) can easily be calculated in the frequency domain by means of frequency response functions.

Nonlinear systems, however, exhibit three types of steady-state behaviour:

1. *Periodic behaviour.*
   The system keeps returning to the same state after a full period. However, the period of the solution does not need to be equal to the period of excitation.

2. *Quasi-periodic behaviour.*
   The solution is a function of two or more periodic signals, which have incommensurate frequencies. If there is one periodic external excitation, one of the frequencies of the periodic signals will be forced, whereas the others will be free.

3. *Chaotic behaviour.*
   A solution, which is neither periodic nor quasi-periodic.

In general steady-states coexist. The *local stability* of a steady-state can be determined by investigating the evolution in time of an infinitesimally small perturbation of the steady-state. The local stability of a steady-state can be (asymptotically) stable, marginally stable or unstable. A steady-state is called *asymptotically stable (unstable)* if an infinitesimally small perturbation of this steady-state converges to (diverges from) this steady-state with exponential rate. A stable (unstable) steady-state is called an *attractor (repellor)*. In reality the response will always settle to one of the attractors. In the augmented state space each attractor will have its *domain of attraction*. If the initial augmented state of a trajectory lies in the domain of attraction of a certain attractor, this trajectory will converge to this attractor. In case a steady-state is *marginally stable*, an infinitesimally small perturbation of this steady-state will neither grow nor damp out with exponential rate. An infinitesimally small perturbation of one of the system parameters, however, can change both the quantitative and qualitative steady-state behaviour drastically: the system is not structurally stable. A system is *(not) structurally stable* if, for any sufficiently small

perturbation of the defining equations of motion, the resulting flow is (not) topologically equivalent to the initial one. In the nonlinear case a marginally stable steady-state is called a *dynamic bifurcation point.*

Steady-states of (1.1) can be obtained by solving an initial value problem. Given an initial augmented state at $t = t_0$:

$$\begin{bmatrix} q(t_0) \\ \dot{q}(t_0) \\ \phi(t_0) \end{bmatrix} = \begin{bmatrix} q_0 \\ \dot{q}_0 \\ \phi_0 \end{bmatrix}$$

the equations (1.1) can be integrated numerically. Stable steady-states can be calculated by integrating forward in time. Conversely, only some unstable steady-states can be calculated by integrating backwards in time. Information about the domains of attraction of steady-state attractors can be obtained by solving a large number of initial value problems with slightly different initial states. If the system is slightly damped, its equations of motion must be integrated over a long period of time before transients become neglectable and the steady-state is reached. Moreover, if a system parameter, also called a *design variable*, changes in value, the calculations must be repeated. The conclusion is, that a huge amount of CPU-time will be needed to carry out all these calculations, especially if the model has many dofs.

Periodic steady-states, however, can be calculated much more efficiently by solving a two-point boundary value problem. The local stability of the calculated periodic solution can be evaluated afterwards by examining the so-called *Floquet multipliers.* This approach also offers the possibility to follow branches of solutions when a design variable is varied. On these branches local bifurcation points can be detected. The type of bifurcation can be determined by examining the Floquet multipliers. Of all three types of steady-state behaviour mentioned before the periodic behaviour is most frequently met in engineering practice. This supports the concentration on the solution of two point boundary value problems in this thesis.

Accurate information about displacements, strains, stresses, etc. often requires finite element models with many elements and thus many dof. Dynamic analyses based on large models can lead to excessive high CPU-times, despite the current state of computer technology.

In linear dynamics, this problem can easily be circumvented through applying the Ritz reduction method, which is based on the principle of superposition. The displacement field is approximated by a linear combination of a limited number of well chosen displacement functions or modes, whose coefficients act as the dof of the reduced system. Usually a number of eigenmodes with eigenfrequencies lying in a frequency range of interest is chosen. In this way the decrease in model accuracy due to the reduction is kept to a minimum. The frequency range of interest is determined by the frequency spectrum of the external loads. In practice the significant part of this spectrum often ranges from zero to some cut-off frequency f_c. The eigenmodes decouple the system equations. These decoupled equations can be solved separately and the approximate solution is calculated by adding all eigenmode contributions. The amount of CPU-time, which is saved by solving the

reduced system equations instead of the original equations, can be very large. The extra CPU-time needed to calculate the eigenfrequencies and the corresponding eigenmodes is quickly regained. In most analyses one wants to know the eigenfrequencies and eigenmodes of the system anyway.

Component mode synthesis (cms) methods are based on the Ritz reduction technique. With cms methods the linear system is first subdivided in a number of *subsystems*, also called *components, substructures* or *superelements.* A subdivision in components can be advantageous in many situations. These situations will be discussed later on. Subsequently the Ritz reduction method is carried out at component level. Cms methods distinguish themselves by the use of different types of component modes. In general a set of component modes consists of eigenmodes and static correction modes. After reduction, component models are coupled to obtain a compact system model. If desired, these reduced system equations can be decoupled again. Obviously, those cms methods are preferred, which lead to compact system models with eigenfrequencies, which are accurate up to the cut-off frequency, used to reduce the components.

In general the equations of motion of a nonlinear system cannot be decoupled with the exception of so-called linearly separable nonlinear systems, see Van der Varst [1982] . Therefore, in nonlinear dynamics the need to save CPU-time by means of reduction of the number of dof is even greater than in linear dynamics, because the equations have to be solved simultaneously. Unfortunately, it is very difficult to formulate a general procedure, by which a large nonlinear dynamic model can be reduced to a compact model, which is accurate in a prescribed frequency range. In literature two methods can be found by which (large) nonlinear models can be reduced using a simple frequency criterion: the *pseudo-load method* and the *local mode superposition method.* They will be evaluated later on. In this thesis, only the linear components of a system with local nonlinearities will be reduced by application of cms methods. This approach can be considered to be a variant of the pseudo-load method. The CPU-time profits versus the resulting accuracy and the effect of the elimination of high frequency eigenmodes on the accuracy of solutions below the cut-off frequency must be investigated. Usually, the costs involved in this investigation will be small compared to costs saved. Moreover, a better understanding of system behaviour is obtained.

This thesis has been arranged as follows. In the next chapter the reduced equations of motion of dynamic systems with local nonlinearities will be derived. At first the reduction of linear components by means of cms methods will be discussed. Then the local nonlinearities will be taken into account. Conditions for obtaining accurate solutions using reduced nonlinear models will be discussed. The following three chapters deal with numerical methods for the analysis of the periodic behaviour of nonlinear dynamic systems. In chapter three periodic solutions are calculated by solving a two-point boundary value problem using a *time discretization method*, which actually is a finite difference method. An important advantage of this method is the fact that stable as well as (very) unstable solutions can be determined easily. Once a periodic solution is calculated, a *path following method* can be applied to investigate how the periodic solution changes, if a design variable of the system is varied. Crooijmans [1987] successfully used a similar procedure to inves-

tigate the periodic behaviour of rotor-bearing structures. In this thesis the application of a *deferred correction technique* is added. In this technique local and global discretization errors of an approximate periodic solution can be estimated. These can be used to increase the accuracy of the solution. It is a fortunate coincidence that the extra amount of CPU-time, needed to carry out a deferred correction, is neglectable, if the technique is used in combination with path following. Another improvement is the development of a more robust path following method. Chapter four is concerned with the local stability of periodic solutions. In chapter five three types of local bifurcations, which can be found on branches of periodic solutions, will be discussed: the *cyclic fold bifurcation*, the *flip bifurcation* and the *Neimark bifurcation*. Chapter six deals with the calculation of *Lyapunov exponents*. These are used to identify the type of steady-state response (periodic, quasi-periodic or chaotic) which is reached in a numerical integration analysis. In chapter seven the numerical tools are employed to study the steady-state behaviour of a beam system with local nonlinear supports. Finally, in chapter eight a number of conclusions are drawn and some recommendations for further research are given.

All numerical computations made in this thesis were carried out on an Iris 4D/210GTXB computer of Silicon Graphics.

Chapter 2

System modelling and reduction

2.1 Introduction: component mode synthesis

Component mode synthesis (cms) methods are used for the modelling and analysis of large linear dynamic systems, which are undamped, proportionally damped or slightly damped. Their two major features are:

1. The subdivision of the system in a number of components, which can be advantageous in various situations:

   - The components originate from different subcontractors. Each of them is responsible for the dynamic performance of his component. The main contractor, who is responsible for the total system, has to check if requirements with regard to system dynamics are satisfied or not.
   - Some components can be modelled theoretically. Other components have to be identified experimentally, for example in case of unknown damping characteristics.
   - A system contains some or many identical components. Only one of these components needs to be modelled.
   - Several designs have to be analysed to evaluate which of them gives the best dynamic performance. In all designs, some components will be identical and other components will undergo some modifications.

   In general a component will have one or more interfaces. An interface will be part of two or more components and/or local nonlinearities.

2. The number of dof of every component is reduced using the Ritz method. The displacement field x of the component is approximated by a reduced number of component modes t_{1i}:

$$x = \sum_{i=1}^{n_p} t_{1i} p_i = T_1 p \tag{2.1}$$

The equations of motion of a free component are:

$$M\ddot{x} + B\dot{x} + Kx = f \tag{2.2}$$

As stated before, components are assumed to be undamped, proportionally damped or slightly damped, which imposes restrictions on the damping matrix B. In the formulation of component modes several sets of dof will be used. These sets and the relations between them are shown in tables 2.1 and 2.2. Columns x en f are partitioned as follows:

$$x = \begin{bmatrix} x_{\mathrm{B}} \\ x_{\mathrm{I}} \end{bmatrix} = \begin{bmatrix} x_{\mathrm{H}} \\ x_{\mathrm{G}} \end{bmatrix} = \begin{bmatrix} x_{\mathrm{R}} \\ x_{\mathrm{E}} \end{bmatrix} = \begin{bmatrix} x_{\mathrm{F}} \\ x_{\mathrm{S}} \end{bmatrix} = \begin{bmatrix} x_{\mathrm{R}} \\ x_{\mathrm{V}} \\ x_{\mathrm{I}} \end{bmatrix} = \begin{bmatrix} x_{\mathrm{B}} \\ x_{\mathrm{W}} \\ x_{\mathrm{S}} \end{bmatrix} \tag{2.3}$$

$$f = \begin{bmatrix} f_{\mathrm{B}} \\ 0_{\mathrm{I}} \end{bmatrix}_{\mathrm{ex}} + \begin{bmatrix} f_{\mathrm{H}} \\ 0_{\mathrm{G}} \end{bmatrix}_{\mathrm{l}} + \begin{bmatrix} f_{\mathrm{H}} \\ 0_{\mathrm{G}} \end{bmatrix}_{\mathrm{nl}} = f_{\mathrm{ex}} + f_{\mathrm{l}}^{\star} + f_{\mathrm{nl}}^{\star} \tag{2.4}$$

f_{ex} are external loads, $f_{\mathrm{l}}^{\star}$ are internal loads caused by adjacent linear components and $f_{\mathrm{nl}}^{\star}$ are internal loads caused by adjacent local nonlinearities. An optimal cms method should fulfil the following conditions:

1. Each component can be modelled and analysed independently.
2. The reduced system model provides the same (quasi-)static solution as the original, unreduced system model.
3. The set of dof of the reduced component explicitly contains the set of boundary dof. Then reduced component models can be coupled by means of the well-known direct stiffness method.
4. The reduced system model provides an accurate solution in the frequency range of interest. The eigenfrequencies of the reduced system model are accurate up to the cut-off frequency used to reduce components.
5. The costs for calculation of component modes and reduction of matrices can at least be regained by analysing and calculating the reduced system model instead of the original system model.
6. The reduced component models can be derived theoretically (finite element method) as well as experimentally (modal analysis).

2.2 Component modes

Examples in literature show that the accuracy of solutions at system level can not be guaranteed by only including component eigenmodes in the component mode set, see Benfield and Hruda [1971] and Herting [1985] . The accuracy can be improved considerably by

set	dofs	dimension	description
$\mathcal{X}$	x	$(\mathrm{n}_x * 1)$	All physical dof of the component.
$\mathcal{B}$	x_{B}	$(\mathrm{n}_{\mathrm{B}} * 1)$	Boundary dof: dof which are loaded either by internal loads caused by adjacent linear components and/or local nonlinearities or by external loads.
$\mathcal{I}$	x_{I}	$(\mathrm{n}_{\mathrm{I}} * 1)$	Internal dof: dof which are not loaded.
$\mathcal{H}$	x_{H}	$(\mathrm{n}_{\mathrm{H}} * 1)$	Interface dof: dof which are loaded by internal loads caused by adjacent linear components and/or local nonlinearities.
$\mathcal{G}$	x_{G}	$(\mathrm{n}_{\mathrm{G}} * 1)$	The complement of $\mathcal{H}$ in $\mathcal{X}$.
$\mathcal{R}$	x_{R}	$(\mathrm{n}_{\mathrm{R}} * 1)$	A minimal set of dof in $\mathcal{B}$ capable of suppressing all motions of the component as a rigid body.
$\mathcal{E}$	x_{E}	$(\mathrm{n}_{\mathrm{E}} * 1)$	The complement of $\mathcal{R}$ in $\mathcal{X}$.
$\mathcal{V}$	x_{V}	$((\mathrm{n}_{\mathrm{E}} - \mathrm{n}_{\mathrm{I}}) * 1)$	The complement of $\mathcal{R}$ in $\mathcal{B}$.
$\mathcal{S}$	x_{S}	$(\mathrm{n}_{\mathrm{R}} * 1)$	A minimal set of dof in $\mathcal{I}$ capable of suppressing all motions of the component as a rigid body.
$\mathcal{F}$	x_{F}	$(\mathrm{n}_{\mathrm{E}} * 1)$	The complement of $\mathcal{S}$ in $\mathcal{X}$.
$\mathcal{W}$	x_{W}	$((\mathrm{n}_{\mathrm{E}} - \mathrm{n}_{\mathrm{B}}) * 1)$	The complement of $\mathcal{S}$ in $\mathcal{I}$.

Table 2.1: Sets of dof of a component

$\mathcal{X} = \mathcal{B} \cup \mathcal{I}$	$\mathrm{n}_x = \mathrm{n}_{\mathrm{B}} + \mathrm{n}_{\mathrm{I}}$
$\mathcal{X} = \mathcal{R} \cup \mathcal{E}$	$\mathrm{n}_x = \mathrm{n}_{\mathrm{R}} + \mathrm{n}_{\mathrm{E}}$
$\mathcal{X} = \mathcal{S} \cup \mathcal{F}$	
$\mathcal{X} = \mathcal{H} \cup \mathcal{G}$	$\mathrm{n}_x = \mathrm{n}_{\mathrm{H}} + \mathrm{n}_{\mathrm{G}}$
$\mathcal{B} = \mathcal{R} \cup \mathcal{V}$	
$\mathcal{I} = \mathcal{S} \cup \mathcal{W}$	
$\mathcal{E} = \mathcal{I} \cup \mathcal{V}$	
$\mathcal{F} = \mathcal{B} \cup \mathcal{W}$	

Table 2.2: Relations between sets of dof of a component

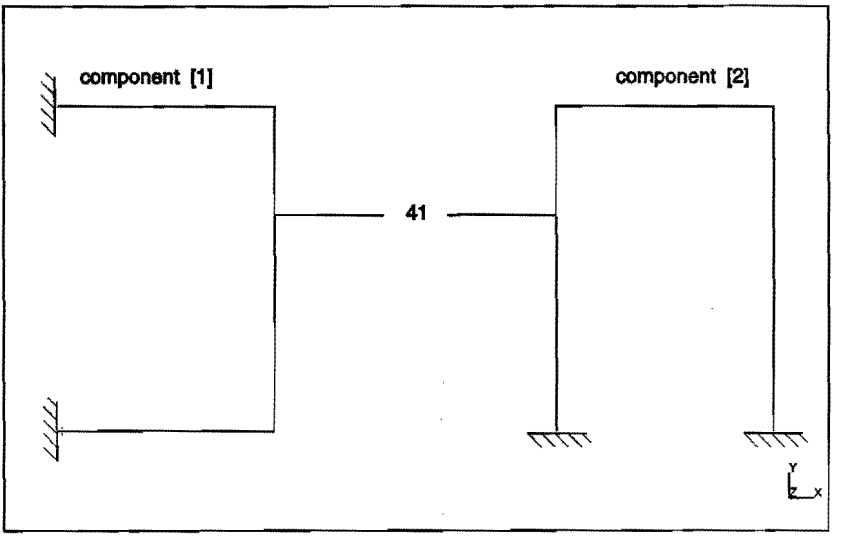

Figure 2.1: Beam system consisting of two components

adding static correction modes for component dof which are loaded by external or internal loads. Further improvement of accuracy can be obtained by introducing modes, which account for the inertia loading of a free component moving as a rigid body. In this context the following types of component modes will be discussed:

1. Rigid body modes
2. Free-interface eigenmodes
3. Flexibility modes
4. Residual flexibility modes

Figure 2.1 shows a 2D linear beam system (ρ = 7850 kg/m^3, E = 2.1 10^{11} N/m^2, A = 3.73 10^{-4} m^2, I = 1.055 10^{-7} m^4), consisting of two components [1] and [2]. These are coupled at the interface node (or boundary node) corresponding to node 41 of the original model of the total system. The system is modelled with 85 beam elements (component [1]: 40 elements, component [2]: 45 elements) with a length of 0.1 m. The resulting numbers of dof of the system and components [1] and [2] are n_q = 246, $n_x^{[1]}$ = 117 and $n_x^{[2]}$ = 132 respectively. This beam system will be used to illustrate several aspects of the cms method in the following sections.

2.2.1 Rigid body modes

A rigid body mode is defined as a motion with constant elastic energy level. It is assumed that no mechanisms can be distinguished in the component, so that the number of rigid body modes n_R will be six at most in the threedimensional space. This implies for the rank of the stiffness matrix:

$$n_x - 6 \leqslant \operatorname{rank} K = n_x - n_R \leqslant n_x \tag{2.5}$$

Rigid body modes, which are stored columnwise in the matrix Φ^R, are defined by:

$$K\Phi^R = \begin{bmatrix} K_{RR} & K_{RE} \\ K_{ER} & K_{EE} \end{bmatrix} \begin{bmatrix} \Phi_{RR} \\ \Phi_{ER} \end{bmatrix} = \begin{bmatrix} O_{RR} \\ O_{ER} \end{bmatrix} = O_R \tag{2.6}$$

The matrix Φ^R can be calculated from:

$$\Phi^R = \begin{bmatrix} \Phi_{RR} \\ \Phi_{ER} \end{bmatrix} = \begin{bmatrix} I_{RR} \\ -K_{EE}^{-1} K_{ER} \end{bmatrix} \tag{2.7}$$

Note that neither component [1] nor component [2] in figure 2.1 has rigid body modes.

2.2.2 Free-interface eigenmodes

Free-interface eigenmodes are calculated by solving the eigenvalue problem of the free component:

$$(-\omega_i^2 M + K)\varphi_i = 0 \qquad i = 1, \ldots, n_x \tag{2.8}$$

The angular eigenfrequency ω_i is related to the eigenfrequency f_i by:

$$\omega_i = 2\pi f_i \tag{2.9}$$

Actually, a solution of (2.8) for $\omega_i = 0$ is a rigid body mode. So rigid body modes form a subset of free-interface eigenmodes. The n_x angular eigenfrequenties ω_i and the corresponding free-interface eigenmodes φ_i are stored in $\ulcorner\Omega\lrcorner$ and Φ respectively:

$$\ulcorner\Omega\lrcorner = \ulcorner\omega_i\lrcorner = \begin{bmatrix} O_{RR} & O_{RE} \\ O_{ER} & \ulcorner\Omega_{EE}\lrcorner \end{bmatrix} \qquad \omega_i \leqslant \omega_{i+1} \tag{2.10}$$

$$\Phi = \begin{bmatrix} \Phi^R & \Phi^E \end{bmatrix} \tag{2.11}$$

The matrix Φ^E contains $n_E = n_x - n_R$ elastic free-interface eigenmodes with angular eigenfrequencies greater than zero. Elastic free-interface eigenmodes with eigenfrequencies smaller than some cut-off frequency f_c are stored columnwise in the matrix of kept free-interface eigenmodes Φ_k; the corresponding angular eigenfrequencies are stored on the diagonal of $\ulcorner\Omega_{kk}\lrcorner$. The remaining elastic free-interface eigenmodes are stored columnwise in the matrix of deleted free-interface eigenmodes Φ_d; the corresponding angular eigenfrequencies are stored on the diagonal of $\ulcorner\Omega_{dd}\lrcorner$:

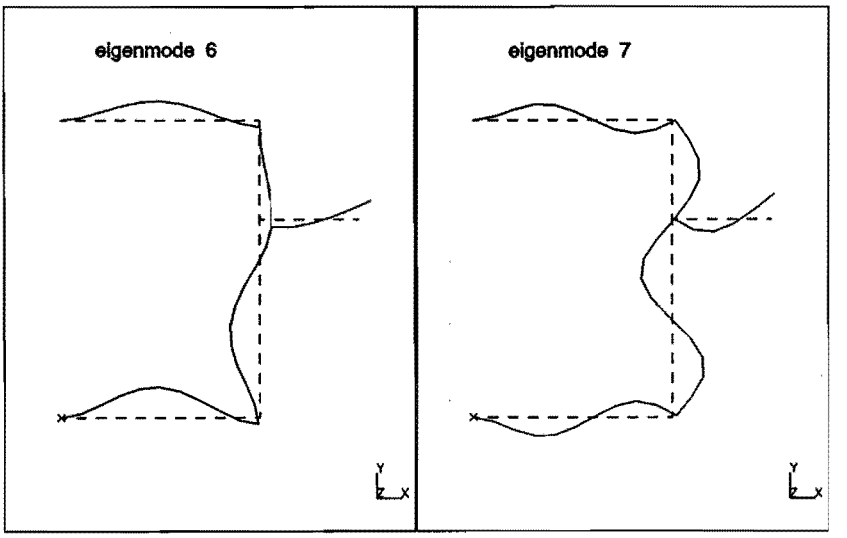

Figure 2.2: Free-interface eigenmodes 6 (left) and 7 (right) of component [1]

$$\Phi^{\mathrm{E}} = \left[\begin{array}{cc} \Phi_{\mathrm{k}} & \Phi_{\mathrm{d}} \end{array} \right] \tag{2.12}$$

$$\ulcorner \Omega_{\mathrm{EE}} \lrcorner = \left[\begin{array}{cc} \ulcorner \Omega_{\mathrm{kk}} \lrcorner & O_{\mathrm{kd}} \\ O_{\mathrm{dk}} & \ulcorner \Omega_{\mathrm{dd}} \lrcorner \end{array} \right] \tag{2.13}$$

$$\mathrm{n_E} = \mathrm{n_k} + \mathrm{n_d} \tag{2.14}$$

Free-interface eigenmodes are normalized on the mass matrix M:

$$\Phi^{\mathrm{t}} M \Phi = I \tag{2.15}$$

$$\Phi^{\mathrm{t}} K \Phi = \ulcorner \Omega \lrcorner^2 \tag{2.16}$$

Figure 2.2 shows the free-interface eigenmodes 6 ($\mathrm{f_6} = 331$ Hz) and 7 ($\mathrm{f_7} = 619$ Hz) of component [1] (cf. figure 2.1).

2.2.3 Flexibility modes

Flexibility modes are defined for the $\mathcal{B}$ set (cf. table 2.1). A flexibility mode is defined as the (quasi-)static elastic displacement field resulting from a unit load acting on one of the boundary dof. Moreover a flexibility mode is defined to be orthogonal to the rigid body modes Φ^{R} with respect to the mass matrix M. The set of $\mathrm{n_B}$ boundary unit loads is given by:

$$F_{\mathrm{B}} = \begin{bmatrix} I_{\mathrm{BB}} \\ O_{\mathrm{IB}} \end{bmatrix} \tag{2.17}$$

Every unit load will result in a displacement, which will be a sum of a displacement as a rigid body X_{r} and an elastic displacement X_{e} (X is used instead of x because the total set F_{B} is considered):

$$X = \begin{bmatrix} X_{\mathrm{B}} \\ X_{\mathrm{W}} \\ X_{\mathrm{S}} \end{bmatrix} = X_{\mathrm{r}} + X_{\mathrm{e}} \tag{2.18}$$

$$X_{\mathrm{r}} = \Phi^{\mathrm{R}} P_{\mathrm{R}} \tag{2.19}$$

Because rigid body modes have been normalized on the mass matrix, substitution of (2.19) in (2.2), followed by premultiplication with $(\Phi^{\mathrm{R}})^t$, yields:

$$\ddot{P}_{\mathrm{R}} = (\Phi^{\mathrm{R}})^t F_{\mathrm{B}} \tag{2.20}$$

Substitution of (2.17) and (2.18) in (2.2), using (2.19) and (2.20), gives:

$$M\ddot{X}_{\mathrm{e}} + B\dot{X}_{\mathrm{e}} + KX_{\mathrm{e}} = RF_{\mathrm{B}} \tag{2.21}$$

with:

$$R = I - M\Phi^{\mathrm{R}}(\Phi^{\mathrm{R}})^t \tag{2.22}$$

In general (quasi-)static elastic displacements ($\ddot{X}_{\mathrm{e}} = \dot{X}_{\mathrm{e}} = O$) can be calculated only relative to $\mathcal{S}$, because in general K is singular:

$$\begin{bmatrix} X_{\mathrm{BB}} \\ X_{\mathrm{WB}} \\ O_{\mathrm{SB}} \end{bmatrix}_{\mathrm{e}} = \begin{bmatrix} X_{\mathrm{FB}} \\ O_{\mathrm{SB}} \end{bmatrix}_{\mathrm{e}} = \begin{bmatrix} K_{\mathrm{FF}}^{-1} & O_{\mathrm{FS}} \\ O_{\mathrm{SF}} & O_{\mathrm{SS}} \end{bmatrix} RF_{\mathrm{B}} = GRF_{\mathrm{B}} \tag{2.23}$$

The matrix of flexibility modes Φ^{F} is found by requiring these elastic displacements to be orthogonal to Φ^{R} with respect to the mass matrix by premultiplation of (2.23) with R^t:

$$\Phi^{\mathrm{F}} = G_{\mathrm{E}} F_{\mathrm{B}} \tag{2.24}$$

with:

$$G_{\mathrm{E}} = R^t G R \tag{2.25}$$

An alternative formulation for the elastic flexibility matrix G_{E} follows from premultiplication of (2.15) with Φ^{-t}, followed by postmultiplication with Φ^t:

$$M\Phi\Phi^t = I \tag{2.26}$$

Substitution of this equation in (2.22), using (2.11) and (2.8), gives:

$$R = M\Phi\Phi^t - M\Phi^{\mathrm{R}}(\Phi^{\mathrm{R}})^t = M\Phi^{\mathrm{E}}(\Phi^{\mathrm{E}})^t = K\Phi^{\mathrm{E}} \lceil \Omega_{\mathrm{EE}} \rfloor^{-2} (\Phi^{\mathrm{E}})^t \tag{2.27}$$

Finally, substitution of (2.27) in (2.25) results into:

$$G_{\mathrm{E}} = \Phi^{\mathrm{E}} \lceil \Omega_{\mathrm{EE}} \rfloor^{-2} (\Phi^{\mathrm{E}})^t \tag{2.28}$$

For component [1] (cf. figure 2.1) three flexibility modes have to be defined. The left picture of figure 2.3 shows the flexibility mode, which results after application of a unit force at the boundary node in the direction of the Y-axis.

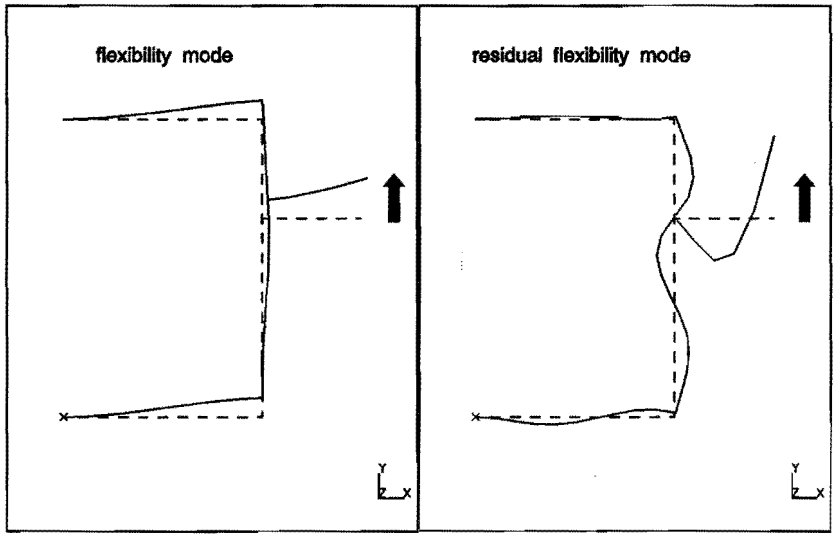

Figure 2.3: Flexibility mode (left) and residual flexibility mode (right) for the displacement of the boundary node in Y-direction

2.2.4 Residual flexibility modes

Just like flexibility modes residual flexibility modes are defined for the $\mathcal{B}$ set. Residual flexibility modes will always be accompanied by the kept free-interface eigenmodes Φ_k in the Ritz reduction matrix. In case of a (quasi-)static load, the residual flexibility modes represent that part of the (quasi-)static response, which originates from the deleted free-interface eigenmodes Φ_d. The matrix of residual flexibility modes Φ^G is defined by:

$$\Phi^G = \Phi^F - \Phi_k \lceil \Omega_{kk} \rfloor^{-2} \Phi_k^t F_B = \Phi_d \lceil \Omega_{dd} \rfloor^{-2} \Phi_d^t F_B \tag{2.29}$$

Residual flexibility modes are orthogonal to Φ_k with respect to both the mass matrix and the stiffness matrix. In appendix A it is shown by means of a simple example that (residual) flexibility modes are not only necessary for obtaining accurate results with reduced multi-component systems; they also can have a great positive influence on the accuracy of results of reduced one-component systems. This especially holds for strains and stresses.

From a numerical point of view, care should be taken in the calculation of residual flexibility modes, if they are computed by subtracting the kept free-interface eigenmode contribution from the flexibility modes. In practice this is always done, because it would be very expensive to compute Φ^G using deleted free-interface eigenmodes. The fact is that $\|\Phi^G\|$ becomes very small in comparison with $\|\Phi^F\|$, if $\omega^2_{n_R+n_k+1}$ becomes very large compared to ω_1^2. Since in computers numbers can only be represented with finite precision, the computed difference of two almost equal matrices will be erroneous if the real difference is in the order of machine precision.

The right picture of figure 2.3 shows the residual flexibility mode of component [1], defined for the displacement of the boundary node in the direction of the Y-axis, in case $f_c = 360$ Hz, resulting in $n_k^{[1]} = 6$. The shapes of this mode and the first deleted free-interface eigenmode (i.e. eigenmode 7, see figure 2.2) show similarity. This is understandable, since equation (2.29) shows a decreasing influence on the residual flexibility mode for deleted eigenmodes with increasing eigenfrequencies.

2.3 Component mode sets

2.3.1 Statically complete component mode sets

The (quasi-)static response of the original component model (2.2), caused by an arbitrary static load acting on the $\mathcal{B}$ set, can exactly be reproduced by a linear combination of the columns of the matrix of rigid body modes Φ^R and the matrix of flexibility modes Φ^F. Therefore condition 2 on page 24 will be fulfilled if the linear subspace of the statically complete component mode set T^S:

$$\left\langle T^S \right\rangle = \left\langle \begin{array}{cc} \Phi^R & \Phi^F \end{array} \right\rangle \tag{2.30}$$

will be a part of the linear subspace, spanned by the columns of the Ritz transformation matrix T_1. So the minimum number of columns of T_1 is equal to $n_B + n_R$.

Three equivalent formulations exist for the statically complete component mode set, in which different types of component modes are used:

$$\left\langle T^S \right\rangle = \left\langle \begin{array}{ccc} \Phi^R & \Phi^{C1} & \Phi^M \end{array} \right\rangle = \left\langle \begin{array}{cc} \Phi^{C2} & \Phi^M \end{array} \right\rangle = \left\langle \begin{array}{ccc} \Phi^R & \Phi^A & \Phi^M \end{array} \right\rangle \tag{2.31}$$

In appendix B the definitions of the redundant constraint modes Φ^{C1} (Hurty [1965]), the constraint modes Φ^{C2} (Craig and Bampton [1968]), the attachment modes Φ^A (Hintz [1975]) and inertia relief modes Φ^M (Hintz [1975]) are given. It is easy to see that, if there are no rigid body modes, flexibility modes become equal to attachment modes. For the proof of:

$$\left\langle \begin{array}{cc} \Phi^R & \Phi^{C1} \end{array} \right\rangle = \left\langle \Phi^{C2} \right\rangle$$

$$\left\langle \Phi^{C1} \right\rangle = \left\langle \Phi^A \right\rangle$$

$$\left\langle \begin{array}{cc} \Phi^A & \Phi^M \end{array} \right\rangle = \left\langle \Phi^F \right\rangle$$

is referred to Craig and Bampton [1968] , Craig [1985] and Chang [1977] , respectively. The main reason for using (2.30) as statically complete component mode set in this thesis is, that this set offers the possibility to determine the resulting reduced component model by means of experiments in contrast with the sets given in (2.31), see Craig [1985] and section 2.4.

2.3.2 Dynamic component mode sets

A dynamic component mode set T_1 is a statically complete component mode set supplemented with a number of elastic eigenmodes, selected on base of a frequency criterion. The eigenmodes can be of the type free-interface or fixed-interface. So two dynamic component mode sets (or Ritz transformation matrices) can be distinguished:

$$\left\langle T_1^{\mathrm{D1}} \right\rangle = \left\langle \begin{array}{cccc} T^{\mathrm{S}} & \Phi_{\mathrm{k}} \end{array} \right\rangle = \left\langle \begin{array}{cccc} \Phi^{\mathrm{G}} & \Phi^{\mathrm{R}} & \Phi_{\mathrm{k}} \end{array} \right\rangle \tag{2.32}$$

$$\left\langle T_1^{\mathrm{D2}} \right\rangle = \left\langle \begin{array}{cc} T^{\mathrm{S}} & \Phi_{\mathrm{k}}^{\mathrm{fx}} \end{array} \right\rangle \tag{2.33}$$

A dynamic component mode set contains $\mathrm{n}_p = \mathrm{n_B} + \mathrm{n_R} + \mathrm{n_k}$ columns.

With respect to the accuracy of reduced, undamped dynamic systems (condition four on page 24) it is concluded on empirical grounds and based on information from literature (Hintz [1975]) that:

- If the same reduced number of dof is used, T_1^{D1} demonstrates a more uniform distribution of the error percentage than T_1^{D2} when eigenfrequencies of the original system model are compared with eigenfrequencies of the reduced system model.
- In contrast with T_1^{D2}, T_1^{D1} usually results in a reduced system model which is accurate up to the cut-off frequency used to reduce the components; see section 2.5 for an example.

The columns of a component mode set have to be linearly independent to avoid ambiguous solutions. Thus a component mode set must be of full column rank, not only theoretically, but also numerically. This can be checked by a singular value decomposition of the Ritz transformation matrix T_1. A trivial remark is that the number of columns in a component mode set is not allowed to be greater than the original number of dof. Because reduction of the number of dof is one of the goals of cms, this condition will never be violated.

2.4 The reduced component model

After a dynamic component mode set has been determined, the original displacement field x will be approximated by:

$$x = T_1 p \tag{2.34}$$

with:

$$x = \begin{bmatrix} x_{\mathrm{B}} \\ x_{\mathrm{I}} \end{bmatrix} \; ; \; T_1 = \begin{bmatrix} T_{\mathrm{BB}} & T_{\mathrm{BJ}} \\ T_{\mathrm{IB}} & T_{\mathrm{IJ}} \end{bmatrix} \; ; \; p = \begin{bmatrix} p_{\mathrm{B}} \\ p_{\mathrm{J}} \end{bmatrix}$$

The reduced component model with dof p is derived by substitution of (2.34) in (2.2), followed by premultiplication with T_1^{t}:

$$M_p\ddot{p} + B_p\dot{p} + K_p p = f_p \tag{2.35}$$

with:

$$M_p = T_1^t M T_1 \quad ; \quad B_p = T_1^t B T_1 \quad ; \quad K_p = T_1^t K T_1 \quad ; \quad f_p = T_1^t f$$

If free-interface eigenmodes are used, it is trivial that the first $n_R + n_k$ eigenfrequencies and eigenmodes of the reduced component are equal to those of the original component. In general, the n_B highest "eigenfrequencies" will be inaccurate, because their corresponding eigenmodes will be linear combinations of residual flexibility modes. Therefore, these eigenfrequencies, referred to as artificial eigenfrequencies, will be greater than or equal to the lowest deleted genuine eigenfrequency. In linear dynamics, the artificial eigenfrequencies will not have a negative influence on the accuracy of the solution, because the external load signal does not contain these high frequencies. On the contrary, the low frequency contribution of these eigenfrequencies does improve the accuracy of the solution, see appendix A and frequency domain considerations below.

A closer investigation learns that only the set $T_1^{D1} = \left[\begin{array}{ccc} \Phi^G & \Phi^R & \Phi_k \end{array} \right]$ leads to a reduced component model, which can be determined (almost) entirely by means of modal analysis (condition six on page 24). For this set the matrices in (2.35) become:

$$M_p = \left[\begin{array}{ccc} M_{GG} & O_{GR} & O_{Gk} \\ O_{RG} & M_{RR} & O_{Rk} \\ O_{kG} & O_{kR} & I_{kk} \end{array} \right] \quad ; \quad B_p = \left[\begin{array}{ccc} B_{GG} & O_{GR} & O_{Gk} \\ O_{RG} & O_{RR} & O_{Rk} \\ O_{kG} & O_{kR} & 2^{\lceil}\Xi_{kk}{}^{\rfloor}{}^{\lceil}\Omega_{kk}{}^{\rfloor} \end{array} \right] \quad ;$$

$$K_p = \left[\begin{array}{ccc} K_{GG} & O_{GR} & O_{Gk} \\ O_{RG} & O_{RR} & O_{Rk} \\ O_{kG} & O_{kR} & {}^{\lceil}\Omega_{kk}{}^{\rfloor}{}^2 \end{array} \right] \quad ; \quad f_p = \left[\begin{array}{ccc} \Phi_B^G & \Phi_B^R & \Phi_{Bk} \end{array} \right]^t f_B$$

with:

$$M_{GG} = (\Phi^G)^t M \Phi^G = \Phi_{Bd}{}^{\lceil}\Omega_{dd}{}^{\rfloor}{}^{-4}\Phi_{Bd}^t$$

$$M_{RR} = (\Phi^R)^t M \Phi^R$$

$$B_{GG} = (\Phi^G)^t B \Phi^G = 2\Phi_{Bd}{}^{\lceil}\Omega_{dd}{}^{\rfloor}{}^{-3\lceil}\Xi_{dd}{}^{\rfloor}\Phi_{Bd}^t$$

$$K_{GG} = (\Phi^G)^t K \Phi^G = \Phi_{Bd}{}^{\lceil}\Omega_{dd}{}^{\rfloor}{}^{-2}\Phi_{Bd}^t = \Phi_{BB}^G$$

By transformation of (2.2) to the frequency domain the following matrix of frequency-response-functions can be derived:

$$H(\omega) = \sum_{r=1}^{n_R} \frac{\varphi_r \varphi_r^t}{-\omega^2} + \sum_{k=1}^{n_k} \frac{\varphi_k \varphi_k^t}{-\omega^2 + 2\xi_k \omega_k \omega j + \omega_k^2} + \sum_{d=1}^{n_d} \frac{\varphi_d \varphi_d^t}{-\omega^2 + 2\xi_d \omega_d \omega j + \omega_d^2} \tag{2.36}$$

If $\omega \ll \omega_c$, the boundary partition of the last term in (2.36) can be approximated by the following Maclaurin-series expansion up to the order ω^2:

$$\sum_{d=1}^{n_d} \frac{\varphi_{Bd}\varphi_{Bd}^t}{-\omega^2 + 2\xi_d\omega_d\omega j + \omega_d^2} \approx K_{GG} - \omega B_{GG} j + \omega^2 \sum_{d=1}^{n_d} \frac{\varphi_{Bd}\varphi_{Bd}^t(1-4\xi_d^2)}{\omega_d^4} \tag{2.37}$$

If (2.35) is transformed to the frequency domain the matrix of frequency-response-functions will be identical to (2.36) except for the last term. A Maclaurin-series expansion up to the order ω^2 of the boundary partition of this term is given by:

$$K_{GG} - \omega B_{GG} j + \omega^2 (M_{GG} - B_{GG} K_{GG}^{-1} B_{GG}) \tag{2.38}$$

If $\xi_d \ll 1$, the last terms of (2.37) and (2.38) are approximately equal to M_{GG}. Under the assumptions that Φ_{Bd} is regular and $n_d = n_B$, these terms can be shown to be equal.

In the experimental modal analysis the modal parameters ω_k, ξ_k and φ_k are usually estimated by a curve fit on the function:

$$H(\omega) = \frac{R_L}{-\omega^2} + \sum_{k=1}^{n_k} \frac{\varphi_k\varphi_k^t}{-\omega^2 + 2\xi_k\omega_k\omega j + \omega_k^2} + R_H \tag{2.39}$$

In case $n_R = 1$, we have $M_{RR} = 1$ and $R_L = \Phi^R(\Phi^R)^t$. In case $n_R > 1$, M_{RR} and Φ^R must be obtained using theoretical considerations. The column of the high frequency residue R_H, which corresponds to the excitation point, can be identified with the same column of K_{GG}. So, every boundary dof must be excited once to determine K_{GG} completely. As has been shown, it will be possible to determine M_{GG} and B_{GG} experimentally, once curve fitting procedures are available for a function with a high frequency residue of the form: $R_H(\omega) = R_{H1} + \omega R_{H2} j + \omega^2 R_{H3}$.

A cut-off frequency of 360 Hz resulted in a reduced model of 9 dof (6 free-interface eigenmodes and 3 residual flexibility modes) for component [1] and a reduced model of 10 dof (7 free-interface eigenmodes and 3 residual flexibility modes) for component [2]. Table 2.3 shows the eigenfrequencies of the reduced models and the corresponding eigenfrequencies of the original models.

2.5 Coupling of reduced component models

A reduced linear system model can be assembled by demanding compatibility of interface dof and equilibrium of interface loads of adjacent components. This is realized by application of the direct stiffness method.

Firstly the generalized dof p_B are replaced by the boundary dof x_B (condition three on page 24):

$$\begin{bmatrix} p_B \\ p_J \end{bmatrix} = T_2 \begin{bmatrix} x_B \\ p_J \end{bmatrix} \quad ; \quad T_2 = \begin{bmatrix} T_{BB}^{-1} & -T_{BB}^{-1}T_{BJ} \\ O_{JB} & I_{JJ} \end{bmatrix} \tag{2.40}$$

Subsequently the boundary dof x_B, referring to a component dependent set of local basis vectors, are replaced by the boundary dof y_B, referring to a set of global base vectors:

no.	Original [1]	Reduced [1]	Original [2]	Reduced [2]
1	33.37810	33.37810	21.47194	21.47194
2	74.80584	74.80584	87.23502	87.23502
3	157.2070	157.2070	120.7789	120.7789
4	224.3831	224.3831	163.0176	163.0176
5	267.0763	267.0763	222.0986	222.0986
6	331.4843	331.4843	323.5042	323.5042
7			358.0173	358.0173
7	619.4241	889.9338		
8	746.7665	1195.364	577.1514	867.4488
9	790.0817	3616.592	694.9540	1281.066
10			746.9802	3992.297

Table 2.3: Eigenfrequencies [Hz] of original and reduced models for components [1] and [2]

$$\begin{bmatrix} x_B \\ p_J \end{bmatrix} = T_3 \begin{bmatrix} y_B \\ p_J \end{bmatrix} \quad ; \quad T_3 = \begin{bmatrix} T_{BB}^{lg} & O_{BJ} \\ O_{JB} & I_{JJ} \end{bmatrix} \tag{2.41}$$

If y is defined as the column of all independent boundary dof of the system, a column q can be defined as the column of all independent reduced system dof:

$$q = \begin{bmatrix} y^t & p_J^{[1]t} & \dots & p_J^{[c]t} & \dots & p_J^{[N_c]t} \end{bmatrix}^t \tag{2.42}$$

The superscript [c] means belonging to component [c]. In fact almost all quantities discussed so far in this chapter belonged to a component and should have been provided with this superscript. However, because in the theory a single component has been discussed so far, this superscript has been omitted to enlarge readability. For every component a (Boolean) matrix T_4 can be formulated, which localizes the positions of the dof of the reduced component in q:

$$\begin{bmatrix} y_B \\ p_J \end{bmatrix}^{[c]} = T_4^{[c]} q \tag{2.43}$$

Finally, for every component the matrix $T^{[c]}$ can be calculated, which relates the reduced system dof to the original component dof:

$$x^{[c]} = T^{[c]} q \tag{2.44}$$

with:

$$T^{[c]} = \prod_{i=1}^{4} T_i^{[c]}$$

Now the reduced system model is derived by assembling the reduced component models:

$$M_q\ddot{q} + B_q\dot{q} + K_q q = f_{ex} + f_{nl}^{\star} \tag{2.45}$$

with:

$$M_q = \sum_{c=1}^{N_c} (T^{[c]})^t M^{[c]} T^{[c]}$$

$$B_q = \sum_{c=1}^{N_c} (T^{[c]})^t B^{[c]} T^{[c]}$$

$$K_q = \sum_{c=1}^{N_c} (T^{[c]})^t K^{[c]} T^{[c]}$$

$$f_{ex} = \sum_{c=1}^{N_c} (T^{[c]})^t f_{ex}^{[c]} = \left[\begin{array}{cccccc} f_{yex}^t & (0_J^{[1]})^t & \ldots & (0_J^{[c]})^t & \ldots & (0_J^{[N_c]})^t \end{array} \right]^t$$

$$\sum_{c=1}^{N_c} (T^{[c]})^t f_1^{\star[c]} = 0$$

$$f_{nl}^{\star} = \sum_{c=1}^{N_c} (T^{[c]})^t f_{nl}^{\star[c]} = \left[\begin{array}{cccccc} f_{ynl}^{\star t} & (0_J^{[1]})^t & \ldots & (0_J^{[c]})^t & \ldots & (0_J^{[N_c]})^t \end{array} \right]^t$$

Coupling of the reduced models of components [1] and [2] (cf. figure 2.1), which were described in the previous section, results in a reduced system model of 16 dof (= 9 (reduced component [1]) + 10 (reduced component [2]) - 3 (constraints)). The eigenfrequencies of this reduced model are compared with the eigenfrequencies of the original system model in table 2.4. The relative errors in the eigenfrequencies of the reduced system are very small up to the cut-off frequency. Note that all relative errors are positive, which means that all eigenfrequencies of the reduced system are upper-bounds for the exact eigenfrequencies; this fact is inherent in the use of the Rayleigh-Ritz method. The artificial eigenfrequencies above the cut-off frequency again have a positive influence on the accuracy in the low frequency range.

With respect to condition five on page 24 can be said that generally the derivation of a reduced system model will cost slightly more CPU-time if $T_1^{D1} = \left[\begin{array}{ccc} \Phi^G & \Phi^R & \Phi_k \end{array} \right]$ is used instead of $T_1^{D2} = \left[\begin{array}{ccc} \Phi^{C2} & \Phi^M & \Phi_k^{fx} \end{array} \right]$. Table 2.5 gives a somewhat subjective estimate of the costs.

Considering all conditions on page 24 it can be concluded that T_1^{D1} may be preferred to T_1^{D2}. A process control program has been developed for the commercial finite element package ASKA (ASKA [1986]), in which the cms method based on the dynamic component mode set T_1^{D1} has been implemented. The iterative Lanczos method or the simultaneous vector iteration method can be used to partially solve the eigenvalue problem (2.8).

no.	Original [Hz]	Reduced [Hz]	Relative error [%]
1	35.99628	35.99628	+0.00000
2	43.48293	43.48293	+0.00000
3	89.78558	89.78559	+0.00001
4	132.6038	132.6038	+0.00000
5	198.6461	198.6495	+0.00171
6	210.4793	210.4803	+0.00048
7	247.8246	247.8434	+0.00759
8	264.7874	264.7895	+0.00079
9	312.5953	312.6369	+0.01331
10	327.7563	327.8017	+0.01385
11	357.9971	357.9975	+0.00011
12	564.9868	652.9783	+15.6
13	606.7133	869.3160	+43.3
14	687.3464	1110.970	+61.5
15	717.5338	1276.873	+78.0
16	731.4784	2558.165	+250.

Table 2.4: Comparison of eigenfrequencies of original and reduced system model

T_1^{D1}			T_1^{D2}		
calculation of:		costs:	calculation of:		costs:
Φ^R,Φ_k	(2.7),(2.8)	very expensive	Φ_k^{fx}	(B.1)	very expensive
Φ^G	(2.22)	expensive	Φ^{C2},Φ^M	(B.7),(B.15)	very expensive
	(2.23)	very expensive			
	(2.24)	expensive			
	(2.29)	expensive			
T_2	(2.40)	cheap/expensive			
T_3	(2.41)	cheap	T_3	(2.41)	cheap
M, B, K	(2.45)	cheap	M, B, K	(2.45)	cheap

Table 2.5: Comparison of costs in the derivation of a reduced component model

2.6 Addition of local nonlinearities

By means of the cms method, discussed in the previous sections, it is possible to reduce the number of dof of a large linear system in such a way, that the decrease in accuracy of the reduced system model below the cut-off frequency f_c is acceptably small. A one-step reduction technique to reduce a large set of nonlinear system equations using a similar simple frequency criterion, is not available, because eigenvalues and eigenmodes are state dependent.

As stated in the introduction, however, two reduction methods are known from literature by which nonlinear dynamic models have successfully been reduced using a simple frequency criterion: the pseudo-load method and the local mode superposition method.

In the pseudo-load method (Stricklin and Haisler [1977] , Morris [1977] , Shah et al. [1979] , Bathe and Gracewski [1981] , Kukreti and Issa [1984]) nonlinearities are treated as pseudo-loads: they are placed on the right-hand side in the equations of motion. Reduction is carried out once on the remaining linear part on the left-hand side. As reduced dof those dof remain, which correspond to eigenmodes with eigenfrequencies below a chosen cut-off frequency. In general this cut-off frequency will be chosen higher than a cut-off frequency based on the frequency spectrum of the external load.

The local mode superposition method (Nickell [1976] and Remseth [1979]) is used in combination with numerical integration. System equations are linearized around the current state and reduced every time step. The eigenfrequencies and eigenmodes at the current state can be derived by updating the eigenfrequencies and eigenmodes of the previous time step using a subspace iteration technique. The cut-off frequency is based on the frequency spectrum of the external load.

It is clear that, if the same number of reduced dof would be used, the pseudo-load method will be much cheaper than the local mode superposition method, because no updating of eigenfrequencies and eigenmodes is required. On the other hand the local mode superposition method will provide a more accurate solution in this case. Differences in costs and accuracy will decrease if more dof are used (or put differently: a higher cut-off frequency is chosen) in the pseudo-load method than in the local mode superposition mode. Strictly speaking, the above comparison can not be made, because, if the local mode superposition method is used, the number of reduced dof may change in one numerical integration analysis.

In section 3.2 periodic solutions will be calculated by solving a two-point boundary value problem by means of a time discretization technique. In this technique the periodic solution is calculated for all time discretization points simultaneously. Therefore the local mode superposition method can not be applied there and a variation on the pseudo-load method will be used.

The reduced nonlinear system equations are derived by coupling the reduced linear system equations (2.45) to the local nonlinearities. Demanding compatibility of interface dof and equilibrium of interface loads $f_{nl}^{\star}$ results into:

$$M_q\ddot{q} + B_q\dot{q} + K_q q = f_{ex} - f_{nl}(\dot{y}, y) \tag{2.46}$$

with:

$$f_{nl}(\dot{y}, y) = -f_{nl}^{\star} \tag{2.47}$$

For simplicity, it is assumed that local nonlinearities are only a function of the boundary dof y and their first time derivatives $\dot{y}$.

The reduced system equations (2.46) still provide a static solution which is identical to the static solution of the unreduced system equations. If the system is dynamically loaded, however, accurate responses can not be guaranteed using a cut-off frequency based on the frequency spectrum of the external load alone. In general it can be stated, that an accurate reduced system model has been derived, if additional eigenmodes have a neglectable influence on the frequency spectrum of $f_{ex} - f_{nl}(\dot{y}, y)$ and if, at the same time, the contribution of this frequency spectrum above the cut-off frequency is neglectable (de Kraker et al. [1989]). It is expected that the nature of the local nonlinearity and the amount of damping in the system will have a great influence on the final cut-off frequency, which must be used to get an accurate reduced system model. A simple illustration is given in the next section.

2.7 A beam system with nonlinear support

Consider a 2D pinned-pinned steel beam. In the middle the beam is excited by a harmonic tranversal load and supported by a linear spring, a linear damper and a nonlinear element. Because of symmetry it is sufficient to consider the pinned-sliding beam system shown in figure 2.4. The pinned-sliding beam is modelled with 25 beam elements (pure bending) of equal size. This beam system will be referred to very often in forthcoming chapters of this thesis. In all calculations the values of the mass density ρ, the modulus of elasticity E, the area of the cross-section A and the second moment of area for the cross-section I are kept constant:

$\rho = 7850 \ \mathrm{kg/m^3}$

$\mathrm{E} = 2.1\,10^{11} \ \mathrm{N/m^2}$

$\mathrm{A} = 1.7593\,10^{-4} \ \mathrm{m^2}$

$\mathrm{I} = 1.7329\,10^{-8} \ \mathrm{m^4}$

The length of the beam l, the harmonic transversal force:

$\mathrm{f_{ex}} = \mathrm{F_{dy}} \cos(2\pi \mathrm{f_e t})$

the stiffness of the linear spring $\mathrm{k_l}$, the damping coefficient of the linear damper b and the force originating from the nonlinear element $\mathrm{f_n} = \mathrm{f_n}(\dot{\mathrm{y}}, \mathrm{y})$ are variable, however, and are specified at places, where is referred to this beam system. For static loads ($\mathrm{f_e} = 0$) the stiffness of the linear beam is:

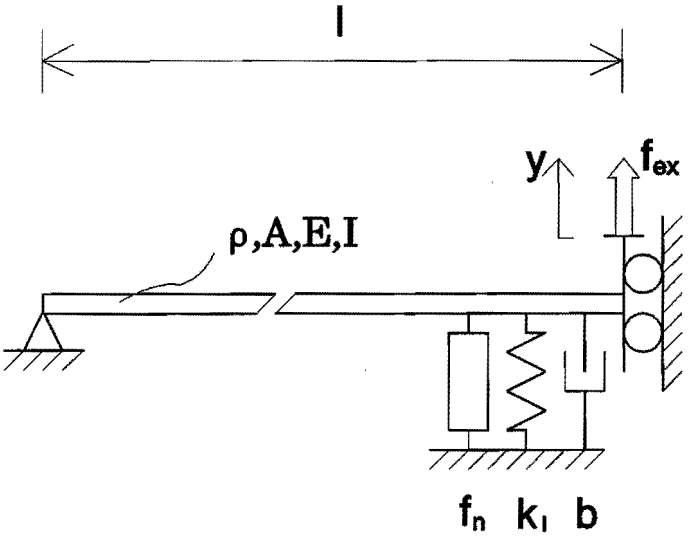

Figure 2.4: Harmonically excited beam system with a local nonlinearity

$$k_{beam} = \frac{F_{dy}}{y} = \frac{3EI}{l^3} = \frac{10917}{l^3} \tag{2.48}$$

In the example of this section the variable quantities are: $l = 1.5$ m, $k_l = 0$ N/m, $b = 0.117$ Ns/m, $f_n = 4.56\ 10^6\ y^3$, $f_{ex} = 19.69\cos(2\pi f_e t)$, $f_e = 23 - 27$ Hz. If only the first free-interface eigenmode is taken into account, the three non-zero parameters of the dimensionless equation of motion derived in appendix C become: $\xi = 0.001$, $\mu = 0.05$ and $\Omega = 2.57 - 3.01$. So in a first approximation the beam system may be identified with a very slightly damped, weakly nonlinear, 1 dof Duffing system, which is excited in the first harmonic resonance region. It is well-known (Stoker [1966]), that this system exhibits three periodic solutions for one value of f_e in this region: two stable solutions with maximum and minimum amplitude and one unstable solution. For the beam system three multi-dof models are made: a 3 dof, a 4 dof and a 6 dof model. The cut-off frequencies used are 100 Hz, 300 Hz and 750 Hz respectively. Note that the frequency range of the excitation is much lower than the cut-off frequencies. In the n dof model, the displacement field of the beam is approximated by n-1 free-interface eigenmodes and 1 residual flexibility mode. The eigenfrequencies of the reduced beam models are shown in table 2.6 (the 8 dof model is used in chapter 7).

Using the numerical methods ($o(\Delta\tau^4)$ scheme, $n_\tau = 800$), which will be introduced in the next chapter, a part of the branch with the maximum amplitude solutions is calculated for all models. The CPU-times for the 3 dof, 4 dof and 6 dof calculations are 206 s. (42 path following steps), 1095 s. (98 steps) and 2759 s. (98 steps) respectively. As can be seen in figure 2.5 the 4 dof and the 6 dof model give similar results. For both models the

No.	3 dof model	4 dof model	6 dof model	8 dof model
1	8.9592	8.9592	8.9592	8.9592
2	80.633	80.633	80.633	80.633
3	260.29	223.98	223.98	223.98
4		537.79	439.01	439.01
5			725.75	725.75
6			1416.1	1084.2
7				1514.6
8				2727.9

Table 2.6: Eigenfrequencies [Hz] of reduced beam models

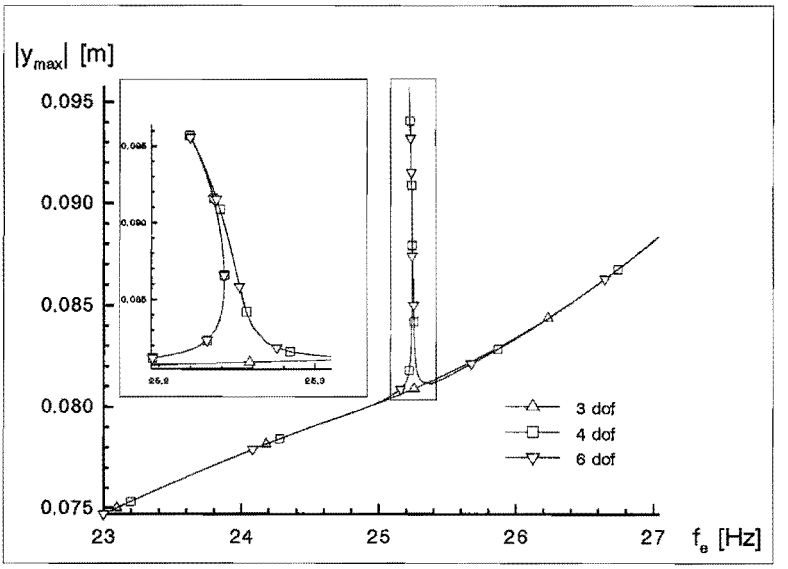

Figure 2.5: Amplitude-frequency plots for 3 dof, 4 dof and 6 dof model

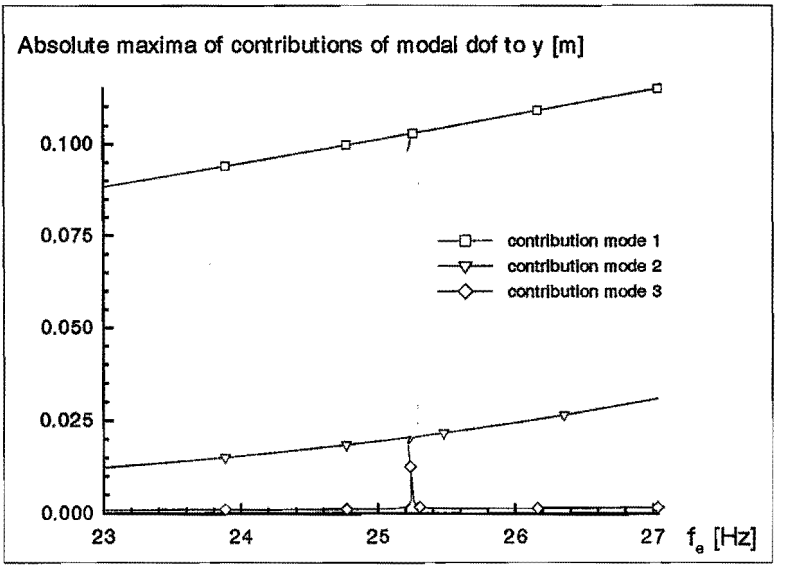

Figure 2.6: Absolute maxima of the contributions to y of the first 3 modes for the 6 dof model

calculated solutions are stable, except for a small frequency range near 25.25 Hz ($\approx f_3/9$), where multiple solutions and a superharmonic resonance peak, caused by the third free-interface eigenmode, see figure 2.6, are observed. It must be emphasized, that this peak will rapidly collapse, if the damping is only slightly enlarged. The (marginally stable) maximum amplitude (= 0.0956 m) solution of the 6 dof model at $f_e = 25.22$ Hz is given in figure 2.7, which also shows the contributions of the lowest 3 eigenmodes to that solution. The contributions of eigenmodes 4 and 5 and of the residual flexibility mode are low: the amplitudes are 7.14E-4 m, 1.93E-4 m and 2.00E-4 m respectively. For the most part, the branch with stable solutions obtained with the 3 dof model is comparative to the branches obtained with the two larger models. However, the superharmonic resonance obviously does not occur at 25.22 Hz, because the third free-interface eigenmode has been deleted, see also Fey et al. [1990] . Instead, a superharmonic resonance occurs near 30 Hz (not visible), which is about 1/9 of the artificial eigenfrequency corresponding to the residual flexibility mode. Tables 2.7 and 2.8 give the Fourier coefficients of $f_{ex} - f_{nl}$ ($f_{nl} = f_n + b\dot{y}$) and y respectively for the maximum amplitude solutions at $f_e = 25.22$ Hz. If CPU-times and accuracy are weighed against each other, it may be concluded that the 4 dof model may be preferred in the investigated frequency range.

Figure 2.8 shows that the 3 dof model may be preferred in the frequency range of 40-71 Hz, where an anti-resonance is found and the system behaves almost linearly. The results of the 3 dof model (140 s. CPU-time, 32 steps) and the 6 dof model (746 s. CPU-time, 32 steps) are fully comparative. The residual flexibility mode of the 3 dof model has a

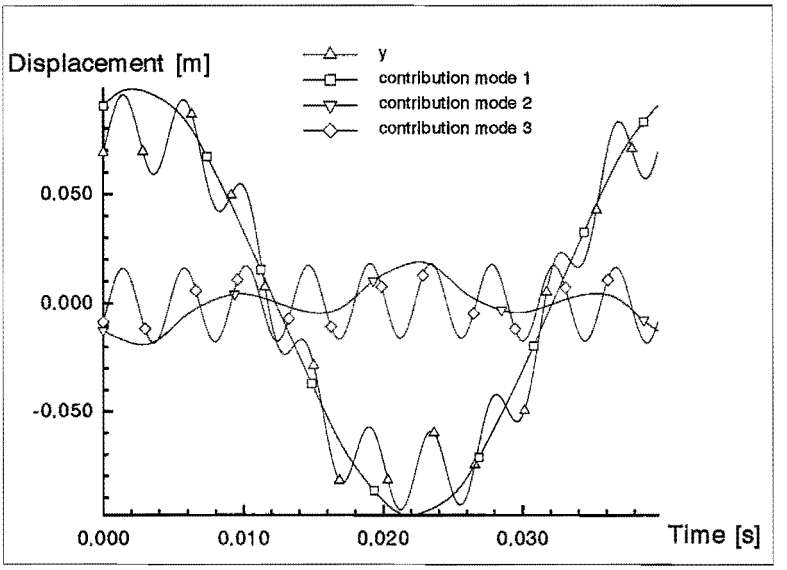

Figure 2.7: Superharmonic resonance near $f_3/9$, 6 dof model

Frequency [Hz]	3 dof model	4 dof model	6 dof model
25.22	1.620E+0	1.544E+0	1.544E+0
75.66	2.245E-1	2.016E-1	2.017E-1
126.10	1.927E-1	1.862E-1	1.872E-1
176.54	3.359E-3	2.569E-1	2.546E-1
226.98	2.735E-3	6.670E-1	6.646E-1
277.42		2.778E-1	2.780E-1
327.86		5.975E-2	5.967E-2
378.30		1.038E-2	1.332E-2
428.74		6.525E-2	5.997E-2
479.18		6.770E-2	6.988E-2
529.62		2.705E-3	
580.06			1.510E-3
630.50			1.599E-3
680.94		4.070E-3	3.681E-3
731.38			1.359E-3

Table 2.7: Fourier coefficients of $f_{ex} - f_{nl}(\dot{y}, y)$ for marginally stable high amplitude solution, $f_e = 25.22$ Hz

Frequency [Hz]	3 dof model	4 dof model	6 dof model
25.22	6.337E-5	6.040E-5	6.042E-5
75.66	6.264E-6	5.626E-6	5.629E-6
126.10	6.202E-7	5.954E-7	5.986E-7
176.54		6.194E-8	6.107E-8
226.98		1.256E-5	1.252E-5
277.42		3.539E-7	3.504E-7
327.86		3.235E-8	2.975E-8
378.30			
428.74		1.032E-8	1.449E-7
479.18		4.943E-8	6.129E-8
529.62		1.925E-8	

Table 2.8: Fourier coefficients of y for marginally stable high amplitude solution, $f_e = 25.22$ Hz

significant positive influence on the accuracy of the response.

The example presented above shows, that superharmonic resonance peaks may be missed, if the corresponding eigenmode has been deleted and may occur at frequencies where they do not belong, if they originate from artificial eigenfrequencies. However, the latter case is easily detected by examining the frequency spectrum of $f_{ex} - f_{nl}(\dot{y}, y)$ or q. Of course, high frequent eigenfrequencies of the unreduced system will be inaccurate due to finite element discretization and may also cause superharmonic resonances in the low frequency range of slightly damped systems.

To avoid resonances below the cut-off frequency, caused by artificial eigenfrequencies, the artificial eigenmodes could be artificially damped or their eigenfrequencies could be artificially enlarged by diminishing the modal masses of the artificial eigenmodes. Actually, Macneal [1971] proposed an inconsistent Ritz-reduction method for linear systems, in which the mass associated with the residual flexibility modes was totally neglected. This method was used in appendix A to formulate approximation (A.10). The static correction contribution of the artificial eigenmodes will hardly be influenced by these actions.

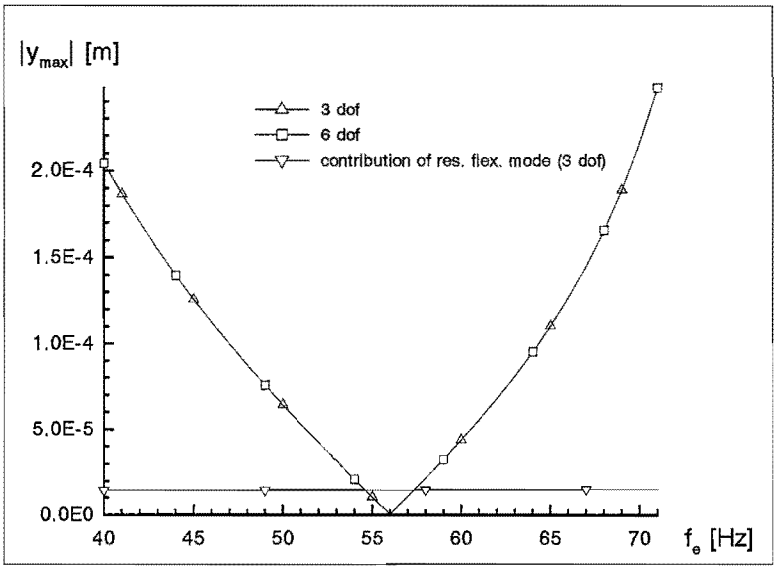

Figure 2.8: Frequency response near anti-resonance; 3 dof and 6 dof model and absolute maximum of the contribution to y of the residual flexibility mode (3 dof model)

Chapter 3

Periodic solutions

3.1 Introduction

The period $T_r = 1/f_r$ of the periodic response q of a nonlinear dynamic system does not need to be equal to the period $T_e = 1/f_e$ of the external excitation f_{ex}. The period of the periodic solution T_p is defined as the time in which the response and the excitation together repeat themselves:

$$T_p = e_T T_e = r_T T_r \tag{3.1}$$

$e_T \in \mathbb{N}$ and $r_T \in \mathbb{N}$ are the smallest possible integers which fulfil (3.1). The response is called *harmonic* if $e_T = r_T = 1$. The response is called *subharmonic of order* r_T/e_T if $r_T < e_T$. According to Thompson and Stewart [1986] the case $r_T > e_T$ (superharmonic response) does not normally occur, because this would imply an identical response under different loading conditions. The term superharmonic *response* should not be confused with the term superharmonic *resonance*. Superharmonic resonance is the phenomenon, in which one or more higher harmonics cause resonance in a (sub)harmonic response.

3.2 Time discretization

It is convenient to replace the real time t by the dimensionless time τ:

$$\tau = \frac{t}{T_p} = f_p t \tag{3.2}$$

The dimensionless time is discretized by n_τ equidistant points τ_i in one period T_p:

$$\tau_i = i\Delta\tau \qquad i \in \mathbb{Z} \tag{3.3}$$

$$\Delta\tau = 1/n_\tau \tag{3.4}$$

For a quantity $Q(\tau)$ the following abbreviation will be used:

$$Q_i = Q(\tau_i) \tag{3.5}$$

In case of a periodic solution a quantity $Q(\tau)$ will repeat itself every T_p seconds:

$$Q_i = Q_{i+n_\tau} \tag{3.6}$$

Therefore it is sufficient to consider the interval $\tau \in [0,1>$, so that $i \in \{0,1,\ldots,n_\tau - 1\}$. Differentiation with respect to the dimensionless time τ is denoted by a prime ($' = d/d\tau$) or as follows:

$$Q_i^{(k)} = \frac{d^k Q_i}{d\tau^k} \tag{3.7}$$

Numerical approximations of $Q_i^{(k)}$ will be denoted by $\tilde{Q}_i^{(k)}$ and $\hat{Q}_i^{(k)}$. The following approximations $\tilde{q}_i'$ and $\tilde{q}_i''$ are used for the velocities and accelerations respectively at τ_i:

$$\tilde{q}_i' = \frac{\tilde{q}_{i+1} - \tilde{q}_{i-1}}{2\Delta\tau} \tag{3.8}$$

$$\tilde{q}_i'' = \frac{\tilde{q}_{i+1} - 2\tilde{q}_i + \tilde{q}_{i-1}}{\Delta\tau^2} \tag{3.9}$$

These relations are known as the central difference scheme with a consistency of order $\Delta\tau^2$. By means of the formal Taylor-series expansions:

$$q_{i-1} = \sum_{k=0}^{\infty} (-1)^k \frac{q_i^{(k)}}{k!} \Delta\tau^k \tag{3.10}$$

$$q_{i+1} = \sum_{k=0}^{\infty} \frac{q_i^{(k)}}{k!} \Delta\tau^k \tag{3.11}$$

the local discretization errors in the velocities and accelerations can be expressed as:

$$\varepsilon_{q_i'} = \frac{q_{i+1} - q_{i-1}}{2\Delta\tau} - q_i' = \sum_{k=1}^{\infty} \frac{q_i^{(2k+1)}}{(2k+1)!} \Delta\tau^{2k} = O(\Delta\tau^2) \tag{3.12}$$

$$\varepsilon_{q_i''} = \frac{q_{i+1} - 2q_i + q_{i-1}}{\Delta\tau^2} - q_i'' = \sum_{k=1}^{\infty} \frac{q_i^{(2k+2)}}{(2k+2)!} \Delta\tau^{2k} = O(\Delta\tau^2) \tag{3.13}$$

Writing equation (2.46) as:

$$g(\ddot{q}, \dot{q}, q, t) = g(f_p^2 q'', f_p q', q, \tau/f_p) = g(q'', q', q, \tau) = 0 \tag{3.14}$$

the following shorthand notations can be introduced:

$$g_i := g(q_i'', q_i', q_i, \tau_i) = 0 \tag{3.15}$$

$$\tilde{g}_i := g(\tilde{q}_i'', \tilde{q}_i', \tilde{q}_i, \tau_i) = 0 \tag{3.16}$$

The local discretization error in the forces ε_{g_i} is given by:

$$\varepsilon_{g_i} := g\left(\frac{q_{i+1}-2q_i+q_{i-1}}{\triangle\tau^2}, \frac{q_{i+1}-q_{i-1}}{2\triangle\tau}, q_i, \tau_i\right) = \left(\frac{\partial g}{\partial q'}\right)_i \varepsilon_{q_i'} + \left(\frac{\partial g}{\partial q''}\right)_i \varepsilon_{q_i''} + \frac{1}{2!}\left(\left(\frac{\partial^2 g}{\partial q'^2}\right)_i \varepsilon_{q_i'}^2 + 2\left(\frac{\partial^2 g}{\partial q' \partial q''}\right)_i \varepsilon_{q_i'}\varepsilon_{q_i''} + \left(\frac{\partial^2 g}{\partial q''^2}\right)_i \varepsilon_{q_i''}^2\right) + \ldots \tag{3.17}$$

Using periodicity of the discretized solution an $0(\triangle\tau^2)$ approximation of the periodic solution $q(\tau) = q(\tau+1)$ can be derived by solving the following algebraic set of equations:

$$\tilde{g}_i = 0 \qquad i = 0, 1, \ldots, n_\tau - 1 \tag{3.18}$$

$$\tilde{q}_{-1} = \tilde{q}_{n_\tau - 1} \tag{3.19}$$

$$\tilde{q}_0 = \tilde{q}_{n_\tau} \tag{3.20}$$

All discretized dof q_i are collected in a column z, which represents the discretized periodic solution:

$$z := [\tilde{q}_0^t, \tilde{q}_1^t, \ldots, \tilde{q}_{n_\tau - 1}^t]^t \tag{3.21}$$

After elimination of the constraints (3.19) and (3.20), the equations (3.18)-(3.20) can be reduced to:

$$h(z) = h_1(z) - h_2 = 0 \tag{3.22}$$

where the column h_2 only contains the contribution of the external load f_{ex}.

It should be noted that it is also possible to calculate periodic solutions of autonomous systems. However, the period T_p of a periodic solution of an autonomous system is unknown in advance. In this case an extra equation must be added to make the set of equations solvable. Because the periodic solution of an autonomous system can be shifted over an arbitrary time interval, an equation can be formulated, which fixes the phase. This can be achieved by setting one of the components of $\tilde{q}'$ equal to zero at a certain time τ_i. In this thesis, however, attention will be paid to non-autonomous systems only.

Starting with an initial estimate z_0, equation (3.22) is solved using a damped Newton iteration scheme:

$$z_{j+1} = z_j + (1/2)^{\zeta_j} \triangle z_j \tag{3.23}$$

$$\frac{\partial h}{\partial z}(z_j) \triangle z_j = -h(z_j) \tag{3.24}$$

During the iteration process, the norm of the residue is required to decrease monotonically:

$$\|h(z_{j+1})\| < \|h(z_j)\| \tag{3.25}$$

The exponent ζ_j is the lowest value of the set $\{0, 1, \ldots, \zeta_{max}\}$, which fulfils this requirement. The column z_j is accepted as solution z_s of (3.22) if the following convergence criterion is satisfied:

$$\|h(z_j)\| < \epsilon_z \|h_2\| \tag{3.26}$$

where ϵ_z is a small number. In calculations $\epsilon_z = 10^{-9}$ unless stated otherwise. z_s is an $O(\Delta\tau^2)$ approximation of the exact periodic solution. The iteration process fails if:

1. (3.25) is not satisfied for $\zeta_j \in \{0, 1, \ldots, \zeta_{max}\}$
2. the Jacobian $\partial h/\partial z$ becomes singular
3. the maximum number of iteration steps j_{max} is exceeded

A lot of CPU-time can be saved in the decomposition of the Jacobian $\partial h/\partial z$, if use is made of its special structure, see appendix D.

3.3 A deferred correction

By means of a deferred correction technique the $O(\Delta\tau^2)$ solution z_s can be improved to an $O(\Delta\tau^4)$ solution z_f. Moreover both the local and the global discretization error can be estimated.

Substitution of (3.12) and (3.13) in (3.17) gives:

$$\varepsilon_{gi} = \left(\frac{\partial g}{\partial q'}\right)_i \frac{q_i^{(3)}}{6}\Delta\tau^2 + \left(\frac{\partial g}{\partial q''}\right)_i \frac{q_i^{(4)}}{12}\Delta\tau^2 + O(\Delta\tau^4) =: \Delta g_i(z_s) + O(\Delta\tau^4) \tag{3.27}$$

Using Taylor-series expansions it can be derived that the difference schemes:

$$\tilde{q}_i^{(3)} = \frac{\tilde{q}_{i+2} - 2\tilde{q}_{i+1} + 2\tilde{q}_{i-1} - \tilde{q}_{i-2}}{2\Delta\tau^3} \tag{3.28}$$

$$\tilde{q}_i^{(4)} = \frac{\tilde{q}_{i+2} - 4\tilde{q}_{i+1} + 6\tilde{q}_i - 4\tilde{q}_{i-1} + \tilde{q}_{i-2}}{\Delta\tau^4} \tag{3.29}$$

have a consistency of $O(\Delta\tau^2)$:

$$q_i^{(3)} - \frac{q_{i+2} - 2q_{i+1} + 2q_{i-1} - q_{i-2}}{2\Delta\tau^3} = O(\Delta\tau^2) \tag{3.30}$$

$$q_i^{(4)} - \frac{q_{i+2} - 4q_{i+1} + 6q_i - 4q_{i-1} + q_{i-2}}{\Delta\tau^4} = O(\Delta\tau^2) \tag{3.31}$$

By noting that:

$$\left(\frac{\partial \tilde{g}}{\partial q'}\right)_i := \left(\frac{\partial g}{\partial q'}\right)(\tilde{q}_i'', \tilde{q}_i', \tilde{q}_i, \tau_i) = \left(\frac{\partial g}{\partial q'}\right)_i (q_i'', q_i', q_i, \tau_i) + O(\Delta\tau^2) \tag{3.32}$$

$$\left(\frac{\partial \tilde{g}}{\partial q''}\right)_i := \left(\frac{\partial g}{\partial q''}\right)(\tilde{q}_i'', \tilde{q}_i', \tilde{q}_i, \tau_i) = \left(\frac{\partial g}{\partial q''}\right)_i (q_i'', q_i', q_i, \tau_i) + O(\Delta\tau^2) \tag{3.33}$$

the $O(\Delta\tau^2)$ term of the local discretization error ε_{g_i} can be estimated by substitution of (3.28)-(3.33) in (3.27):

$$\Delta\tilde{g}_i(z_s) = \left(\frac{\partial \tilde{g}}{\partial q'}\right)_i \frac{\tilde{q}_i^{(3)}}{6}\Delta\tau^2 + \left(\frac{\partial \tilde{g}}{\partial q''}\right)_i \frac{\tilde{q}_i^{(4)}}{12}\Delta\tau^2 + O(\Delta\tau^4) = \Delta g_i(z_s) + O(\Delta\tau^4) \tag{3.34}$$

Let $\Delta\tilde{h}(z_s)$ be defined as:

$$\Delta\tilde{h}(z_s) := [\Delta\tilde{g}_0^t(z_s), \Delta\tilde{g}_1^t(z_s), \ldots, \Delta\tilde{g}_{n_\tau-1}^t(z_s)]^t \tag{3.35}$$

Then the solution Δz_s of the *linear* set of equations:

$$\frac{\partial h}{\partial z}(z_s)\Delta z_s = -\Delta\tilde{h}(z_s) \tag{3.36}$$

is an estimate of the $O(\Delta\tau^2)$ term of the *global discretization* error. Now an $O(\Delta\tau^4)$ approximation z_f of the periodic solution can be obtained by subtracting this deferred correction from z_s (Pereyra [1966]):

$$z_f = z_s - \Delta z_s \tag{3.37}$$

Of course an approximation z_f can also be obtained by the direct application of a central difference scheme with a consistency of $O(\Delta\tau^4)$:

$$\hat{q}_i' = \frac{-\hat{q}_{i+2} + 8\hat{q}_{i+1} - 8\hat{q}_{i-1} + \hat{q}_{i-2}}{12\Delta\tau} \tag{3.38}$$

$$\hat{q}_i'' = \frac{-\hat{q}_{i+2} + 16\hat{q}_{i+1} - 30\hat{q}_i + 16\hat{q}_{i-1} - \hat{q}_{i-2}}{12\Delta\tau^2} \tag{3.39}$$

In appendix D a partitioning of the Jacobian $J := \partial h/\partial z$ is introduced. It can easily be seen that for the choice (3.38), (3.39) the bandwidth of the upper left block $J_{\alpha\alpha}$ is n_q larger than the bandwidth of $J_{\alpha\alpha}$ for the choice (3.8), (3.9). Consequently the amount of CPU-time needed for decomposition of this matrix will approximately increase by a factor $(6n_q - 1)^2/(4n_q - 1)^2$ (≈ 2.25 for large n_q), see appendix D. Moreover no estimates of local and global discretization errors are obtained.

The following example illustrates the benefits of the deferred correction procedure. Consider the beam system presented in section 2.7 ($l = 1$ m, $k_l = 1000$ N/m, $b = 2$ Ns/m, $f_n = 3.0\,10^9$ y^3, $f_{ex} = 15\cos(2\pi f_e t)$, $f_e = 8$ Hz). If only the first free-interface eigenmode of the linear undamped system (i.e. the beam and the linear spring) would be taken into account, the three non-zero parameters in the dimensionless equation of motion in appendix C would be: $\xi = 0.011$, $\mu = 0.38$, $\Omega = 0.38$. So one may call this a slightly damped, moderate nonlinear system. In the following calculations the linear undamped system model was reduced to 10 dof including the 9 lowest free-interface eigenmodes plus one

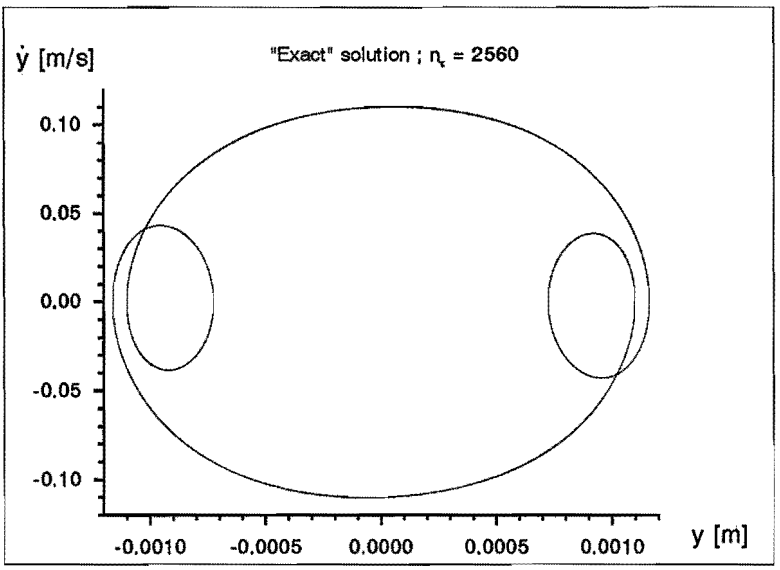

Figure 3.1: Phase portrait

residual flexibility mode. This reduced model was coupled to the damper and the nonlinear spring ($f_{nl} = f_{in} + b\dot{y}$). Periodic solutions were calculated using the $O(\Delta\tau^2)$ scheme, the deferred correction (dc) procedure and the $O(\Delta\tau^4)$ scheme for several values of n_τ. Starting with an initial estimate $z_0 = 0$, it took 6 Newton iterations for convergence ($\epsilon_z = 10^{-10}$) in each of the calculations but the deferred correction calculations, which needed one iteration more, see equations (3.36) and (3.37). Figure 3.1 shows the phase portrait of the stable harmonic solution for the right end of the beam; this solution ($O(\Delta\tau^4)$, $n_\tau = 2560$) is considered to be the exact solution. Figure 3.2 shows the convergence ratio and figure 3.3 the mean global discretization error for the right end of the beam as a function of n_τ. The convergence ratio c_q and the mean global discretization error e_q for dof q are defined as:

$$c_q = \frac{\sum_{i=0}^{N_\tau-1} |q_{4i}^{4N_\tau} - q_{2i}^{2N_\tau}|}{\sum_{i=0}^{N_\tau-1} |q_{2i}^{2N_\tau} - q_i^{N_\tau}|} \tag{3.40}$$

$$e_q = \frac{1}{N_\tau} \sum_{i=0}^{N_\tau-1} |q_i^{N_\tau} - q^{exact}(i\Delta\tau)| \tag{3.41}$$

where the superscript N_τ in $q_i^{N_\tau}$ denotes the number of discretization points. As N_τ increases, the convergence ratio approaches the theoretical values 1/4 for the $O(\Delta\tau^2)$ scheme and 1/16 for the $O(\Delta\tau^4)$ scheme and the deferred correction procedure. Figure 3.4 shows that the total amount of CPU-time needed to calculate the solution grows proportionally with n_τ. The CPU-time needed for decomposition of $J_{\alpha\alpha}$, see appendix D, was approximately 2.25 times higher if the $O(\Delta\tau^4)$ scheme was used instead of the $O(\Delta\tau^2)$ scheme.

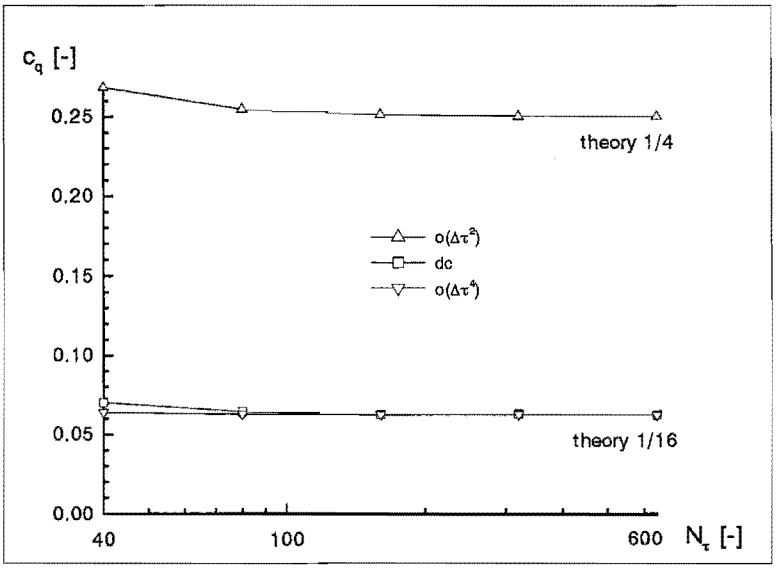

Figure 3.2: Convergence ratio

Deferred correction calculations with twice as many discretization points needed approximately the same amount of CPU-time as $0(\triangle\tau^4)$ calculations, but resulted in a mean global discretization error, which was 5 times lower, see figure 3.3. This means that 1.5 times as many discretization points ($1.5^4 \approx 5$) and thus 50% more CPU-time would be needed to achieve the same accuracy with a direct $0(\triangle\tau^4)$ calculation. Moreover, the deferred correction procedure provided an estimate of the global discretization error of the $0(\triangle\tau^2)$ solution.

3.4 Path following

The designer of a dynamic system often needs to investigate how a periodic solution is influenced by a change in a *design variable* r. This amounts to calculating solutions of:

$$h(z,\mathrm{r}) = h_1(z,\mathrm{r}) - h_2(\mathrm{r}) = 0 \tag{3.42}$$

The design variable r is assumed to be independent of τ. The number of equations in (3.42) is one less than the number of unknowns. Therefore solutions of (3.42) in general will appear as one dimensional branches. These branches can be followed by application of a path following (pf) method. In pf-step k a neighbouring solution $z_{s,k+1}, \mathrm{r}_{s,k+1}$ is determined starting from a known solution $z_{s,k}, \mathrm{r}_{s,k}$ via a predictor-corrector mechanism. This implies that the first solution $z_{s,1}, \mathrm{r}_{s,1}$ must be calculated by the Newton process before pf-step 1 can be carried out. The pf-process is stopped if $\mathrm{r}_{s,k}$ exceeds a user prescribed value.

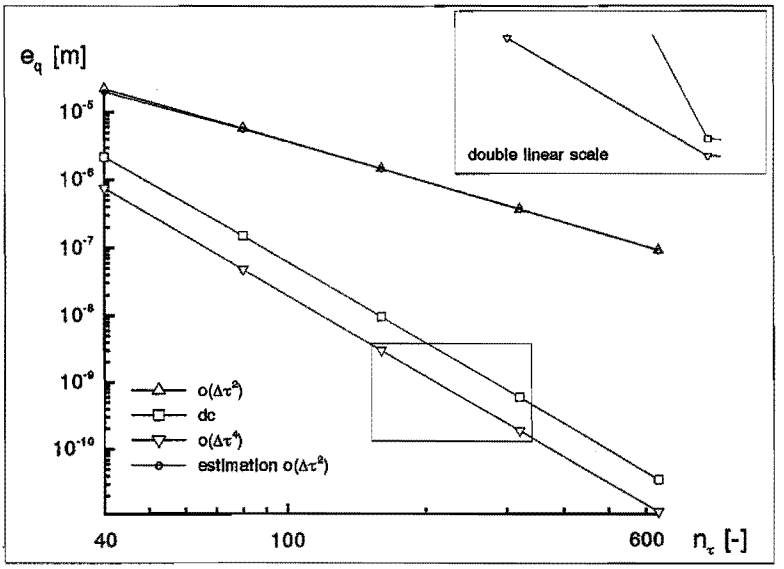

Figure 3.3: Mean global discretization error

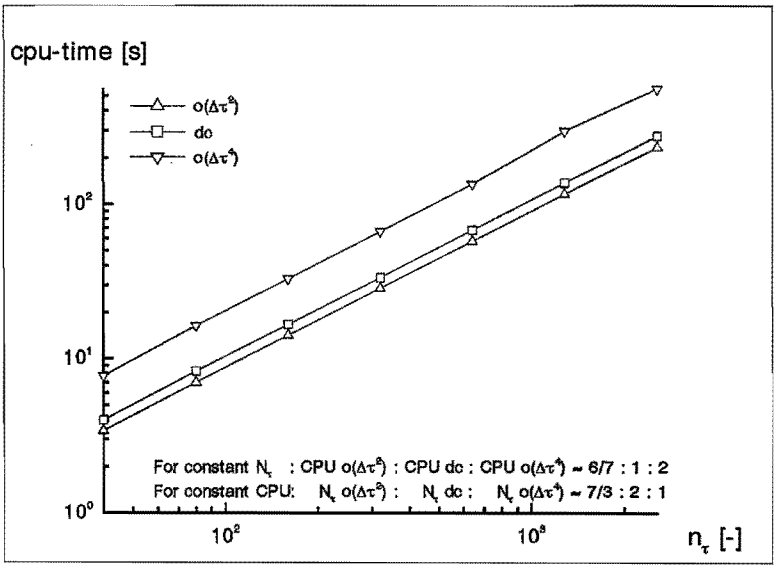

Figure 3.4: CPU-time

In the predictor step the tangent $[p_{z,k}^t, \mathrm{p_{r,k}}]^t$ to the solution branch at $z_{s,k}, \mathrm{r_{s,k}}$ is determined as follows:

$$\frac{\partial h}{\partial z}(z_{s,k}, \mathrm{r_{s,k}})p_{z,k} = -\frac{\partial h}{\partial \mathrm{r}}(z_{s,k}, \mathrm{r_{s,k}})\mathrm{p_{r,k}} \tag{3.43}$$

In pf-step 1 $\mathrm{p_{r,k}}$ is set to 1, if r must increase initially, and set to -1, if r must decrease initially. Now (3.43) can be solved for $p_{z,1}$. The tangent will be scaled by a factor $\sigma_{p,1} > 0$, which is subject to the elliptical constraint:

$$\sigma_{p,k}^2(p_{z,k}^t p_{z,k} + \mathrm{p_{r,k}^2}) = \sigma_k^2 \tag{3.44}$$

σ_k is the stepsize, which lies in a user defined interval:

$$0 < \sigma_{min} \leqslant \sigma_k \leqslant \sigma_{max} \tag{3.45}$$

The prediction $[z_{p,k}^t, \mathrm{r_{p,k}}]^t$ is given by:

$$\begin{bmatrix} z_{p,k} \\ \mathrm{r_{p,k}} \end{bmatrix} = \begin{bmatrix} z_{s,k} \\ \mathrm{r_{s,k}} \end{bmatrix} + \sigma_{p,k} \begin{bmatrix} p_{z,k} \\ \mathrm{p_{r,k}} \end{bmatrix} \tag{3.46}$$

In following pf-steps, the sign of $\sigma_{p,k}$ will be chosen so that the scaled tangents of two succeeding pf-steps form a sharp angle:

$$\mathrm{sign}(\sigma_{p,k+1}) = \mathrm{sign}(\sigma_{p,k}(p_{z,k}^t p_{z,k+1} + \mathrm{p_{r,k}p_{r,k+1}})) \tag{3.47}$$

This ensures that the solution path is travelled in the same direction all the time, provided that σ_k is not too large, see figure 3.5.

Note that in equations (3.36) and (3.43) the decomposition of the same Jacobian is required. So the effort required to obtain an $O(\triangle\tau^4)$ approximation z_f is reduced to calculating $\triangle\tilde{h}(z_s)$, see (3.35).

In general the prediction will not satisfy the convergence criterion:

$$\|h(z, \mathrm{r})\| < \epsilon_z \|h_2(\mathrm{r})\| \tag{3.48}$$

and an iterative correction process will be needed. Correction step m is given by:

$$\begin{bmatrix} z_{c,k,m+1} \\ \mathrm{r_{c,k,m+1}} \end{bmatrix} = \begin{bmatrix} z_{c,k,m} \\ \mathrm{r_{c,k,m}} \end{bmatrix} + \begin{bmatrix} c_{z,k,m} \\ \mathrm{c_{r,k,m}} \end{bmatrix} \tag{3.49}$$

In the first correction step (m=1), the first term on the right hand side of (3.49) is set equal to the prediction (3.46). Corrections $[c_{z,k,m}^t, \mathrm{c_{r,k,m}}]^t$ are calculated by solving the following Newton-like equations:

$$\frac{\partial h}{\partial z}(z_{c,k,m}, \mathrm{r_{c,k,m}})c_{z,k,m} = -\frac{\partial h}{\partial \mathrm{r}}(z_{c,k,m}, \mathrm{r_{c,k,m}})c_{r,k,m} - h(z_{c,k,m}, \mathrm{r_{c,k,m}}) \tag{3.50}$$

supplemented by the equation (Fried [1984]):

$$c_{r,k,m} = \left(\left(\frac{\partial h}{\partial z}(z_{c,k,m}, r_{c,k,m}) \right)^{-1} \frac{\partial h}{\partial r}(z_{c,k,m}, r_{c,k,m}) \right)^t c_{z,k,m} \tag{3.51}$$

This last equation forces the correction to be orthogonal to the solution space of:

$$h(z, r) = h(z_{c,k,m}, r_{c,k,m}) \tag{3.52}$$

As proposed in Allgower [1981] , the new step size σ_{k+1} is determined by the ratio γ_k between the Euclidian norm of the first and the second correction. If $\gamma_k < \gamma_{min}$ the step size will be increased in the next prediction. If $\gamma_k > \gamma_{max}$ the last prediction will be rejected and a new prediction will be calculated after decreasing the step size. γ_{min} and γ_{max} are user defined values.

Further, during the iterative correction process it is required that the norm of the residue is decreasing monotonically:

$$\|h(z_{c,k,m+1}, r_{c,k,m+1})\| < \|h(z_{c,k,m}, r_{c,k,m})\| \tag{3.53}$$

If (3.53) is violated, the last prediction will be rejected and a new prediction will be calculated using a smaller step size σ_k. $[z^t_{c,k,m+1}, r_{c,k,m+1}]^t$ is accepted as solution $[z^t_{s,k+1}, r_{s,k+1}]^t$ of (3.42), if the convergence criterion (3.48) is satisfied.

If the step size is too large, the pf-process may return to the part of the solution curve already passed through, because of (3.47). Often this will occur in areas, where the solution branch is heavily curved, see figure 3.5. This phenomenon can be prevented by requiring that the angle β_1 between the scaled tangent in pf-step k and the line pointing from the solution of pf-step k to the solution of pf-step k + 1 is smaller than a user defined angle β_{1max}:

$$\beta_1 = \arccos \frac{[p^t_{z,k}, p_{r,k}][(z_{s,k+1} - z_{s,k})^t, (r_{s,k+1} - r_{s,k})]^t}{\|[p^t_{z,k}, p_{r,k}]^t\| \|[(z_{s,k+1} - z_{s,k})^t, (r_{s,k+1} - r_{s,k})]^t\|} \leqslant \beta_{1max} \tag{3.54}$$

Furthermore it is possible that the pf-process accidentally jumps over to another branch or a remote part of the same branch if the step size is too large. Usually this can be prevented by requiring that the shape of the increment in the predictor step $p_{z,k}$ does not differ much from the shape of the difference of the two successive solutions $z_{s,k}$ and $z_{s,k+1}$:

$$\beta_2 = \arccos \frac{p^t_{z,k}(z_{s,k+1} - z_{s,k})}{\|p_{z,k}\| \|z_{s,k+1} - z_{s,k}\|} \leqslant \beta_{2max} \tag{3.55}$$

Note that β_2 is independent of the design variable in contrast with β_1, which can be dominated by the design variable.

Again, if condition (3.54) or (3.55) is not fulfiled, the solution of pf-step k + 1 will be rejected, and a new prediction will be calculated using a smaller step size σ_k.

A hard failure of the pf-process occurs if:

1. σ_k becomes smaller than σ_{min}

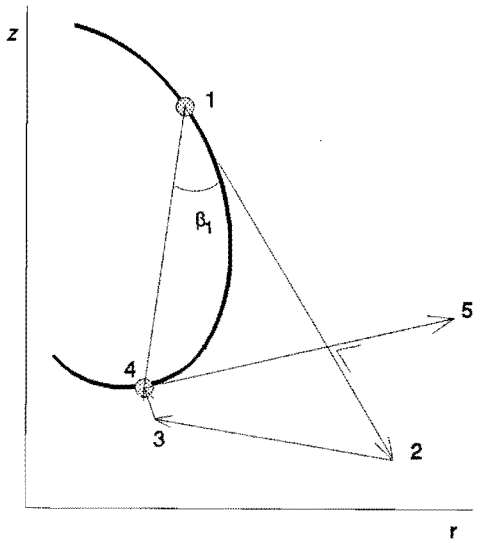

Figure 3.5: A too large step size results in returning to the part of the branch already passed through

2. the iterative correction process does not converge

3. $\partial h/\partial z$ or $\partial h/\partial z + \partial h/\partial \mathrm{r}((\partial h/\partial z)^{-1}\partial h/\partial \mathrm{r})^{\mathrm{t}}$ becomes singular in a dynamic bifurcation point

The following example illustrates the positive effect of conditions (3.53), (3.54) and (3.55). At first a harmonic solution of the beam system introduced at page 51 was calculated using the damped Newton method ($n_\tau = 400$) for $f_e = 9.9$ Hz. The displacement field of the linear, undamped system was approximated by a linear combination of four eigenmodes and one residual flexibility mode. Then a branch of harmonic solutions was calculated for excitation frequencies decreasing from 9.9 to 3 Hz using the path following method. Table 3.1 shows the different conditions under which four calculations (C1-C4) were made. Figure 3.6 shows the amplitude-frequency plot for the right end of the beam. Calculation C1 failed at point E1 because the excitation frequency jumped from 9.3 to 8.5 Hz in the predictor step of the fourth pf-step; subsequently the correction process did not converge anymore. In calculation C2 the superharmonic resonance peak at 3.6 Hz (point E2) was missed. Calculation C3 failed at point E3; the pf-process returned to the already travelled part of the branch. Calculation C4 succeeded in travelling the whole branch. Figure 3.7 shows the uncontrolled angles β_1 in calculation C3 and β_2 in calculation C2.

Calculation	Condition (3.53)	Condition (3.54)	Condition (3.55)
C1	inactive	$\beta_{1max} = 10°$	$\beta_{2max} = 10°$
C2	active	$\beta_{1max} = 10°$	inactive
C3	active	inactive	$\beta_{2max} = 10°$
C4	active	$\beta_{1max} = 10°$	$\beta_{2max} = 10°$

Table 3.1: Path following under different conditions

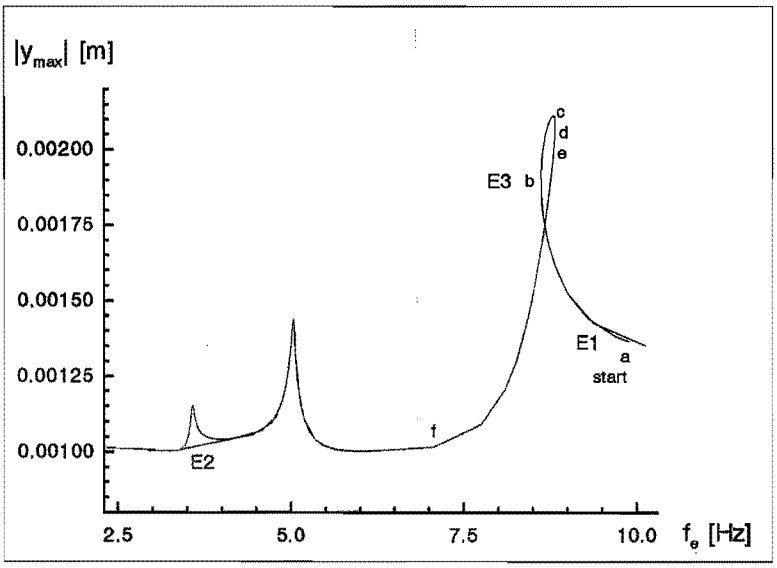

Figure 3.6: Frequency response

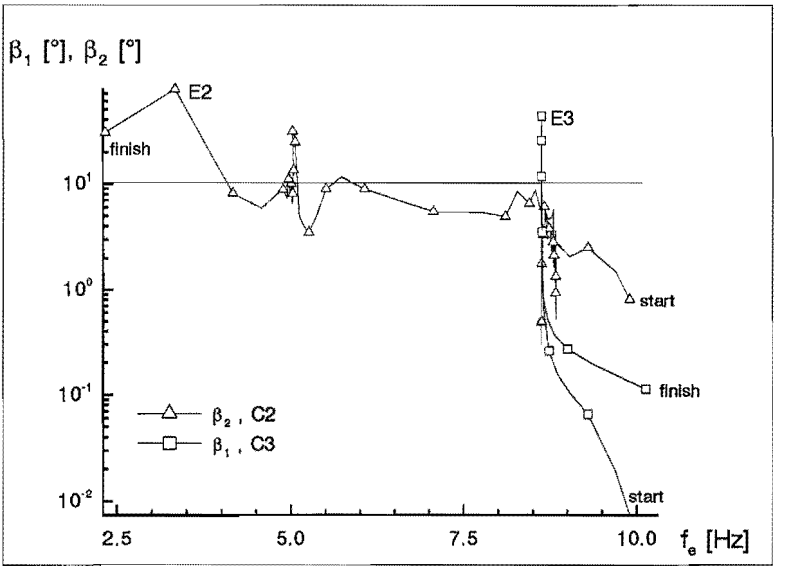

Figure 3.7: Uncontrolled angles β_1 and β_2 in the pf-process

Chapter 4

Local stability of periodic solutions

The *local stability* of a periodic solution $q(\tau) = q(\tau + 1)$ is investigated by linearizing the equations of motion around the periodic solution and examining the evolution in time of an infinitesimally small perturbation $[\delta q_0^t, \delta q_0'^t]^t$ introduced at a certain time τ_0. If higher order terms are neglected, substitution of the perturbed solution $q(\tau)+\delta q(\tau)$ in (2.46) using (3.2) gives the following set of linear differential equations with periodically time-varying coefficients:

$$\mathrm{f_p^2} M_\delta(\tau)\delta q''(\tau) + \mathrm{f_p} B_\delta(\tau)\delta q'(\tau) + K_\delta(\tau)\delta q(\tau) = 0 \tag{4.1}$$

where:

$$M_\delta(\tau) = M_\delta(\tau + 1) = M_q$$

$$B_\delta(\tau) = B_\delta(\tau + 1) = B_q + \mathrm{T_p}\frac{\partial f_{\mathrm{nl}}}{\partial q'}(\tau)$$

$$K_\delta(\tau) = K_\delta(\tau + 1) = K_q + \frac{\partial f_{\mathrm{nl}}}{\partial q}(\tau)$$

and with initial conditions:

$$\delta q(\tau_0) = \delta q_0$$

$$\delta q'(\tau_0) = \delta q_0'$$

By introducing the perturbed state $\delta s(\tau)$:

$$\delta s(\tau) := \begin{bmatrix} \delta q(\tau) \\ \mathrm{f_p}\delta q'(\tau) \end{bmatrix}$$

the equation (4.1) can be reformulated as a first order equation:

$$\delta s'(\tau) = \mathrm{T_p} A_\delta(\tau)\delta s(\tau) \tag{4.2}$$

with:

$$A_\delta(\tau) = A_\delta(\tau+1) = \begin{bmatrix} O & I \\ -M_\delta^{-1}K_\delta(\tau) & -M_\delta^{-1}B_\delta(\tau) \end{bmatrix}$$

and with initial conditions:

$$\delta s(\tau_0) = \delta s_0$$

The general solution of (4.2) is given by:

$$\delta s(\tau) = \Theta(\tau, \tau_0)\delta s_0 \tag{4.3}$$

with:

$$\Theta(\tau_0, \tau_0) = I$$

The theory for investigating the stability of periodic solutions is called after Floquet. It is summarized briefly here, based on Müller and Schiehlen [1985] and Seydel [1988] . The fundamental matrix $\Theta(\tau, \tau_0)$ of the periodically time-varying system (4.2) satisfies the equation:

$$\Theta(\tau+1, \tau_0) = \Theta(\tau, \tau_0)\Theta(\tau_0+1, \tau_0) \tag{4.4}$$

where $\Theta(\tau_0+1, \tau_0) = \Theta_\mu$ is a constant regular matrix, called the *monodromy* matrix. Using this property it can easily be shown that:

$$\Theta(\tau, \tau_0) = \Theta(\tau_0 + \tau^*, \tau_0)\Theta_\mu^\kappa \tag{4.5}$$

where:

$$\tau^* = \tau - \tau_0 - \kappa \quad ; \quad 0 \leqslant \tau^* < 1 \quad ; \quad \kappa \in \mathbb{Z}$$

It is assumed that all eigenvalues μ_i ($|\mu_i| \geqslant |\mu_{i+1}|$) of the monodromy matrix Θ_μ have geometric multiplicity one. This implies that there exists a spectral decomposition:

$$\Theta_\mu = \Psi_\mu \lceil \mu_i \rfloor \Psi_\mu^{-1} \tag{4.6}$$

Substitution of (4.6) in (4.5) gives:

$$\Theta(\tau, \tau_0) = \Theta(\tau_0 + \tau^*, \tau_0)\Psi_\mu \lceil \mu_i \rfloor^\kappa \Psi_\mu^{-1} \tag{4.7}$$

This equation shows that the long term behaviour of $\delta s(\tau)$ is predestinated by the eigenvalues μ_i of the monodromy matrix, the so-called *Floquet multipliers.*

Sometimes the fundamental matrix is written in the form:

$$\Theta(\tau, \tau_0) = \Upsilon(\tau) e^{\Theta_\eta T_p(\tau-\tau_0)} \tag{4.8}$$

with:

$$\Upsilon(\tau_0) = I$$

$$\Upsilon(\tau) = \Upsilon(\tau + 1)$$

The monodromy matrix follows from (4.8) for $\tau = \tau_0 + 1$:

$$\Theta_\mu = e^{\Theta_\eta T_p} = e^{\Psi_\eta T_p [\eta_i] \Psi_\eta^{-1}} \tag{4.9}$$

A comparison between (4.6) and (4.9) leads to the following relationship between the eigenvalues η_i of Θ_η, also called the *characteristic exponents*, and the Floquet multipliers μ_i:

$$\mu_i = e^{\eta_i T_p} \tag{4.10}$$

Note that if (4.10) is used to calculate η_i, $\Im(\eta_i)$ is not uniquely defined.

Now the local stability conditions can be formulated:

- A periodic solution is called *(asymptotically) stable*, if:

$$|\mu_i| < 1, \quad \forall i \quad \Leftrightarrow \quad \Re(\eta_i) < 0, \quad \forall i$$

- A periodic solution is called *marginally stable*, if:

$$|\mu_1| = 1 \quad \Leftrightarrow \quad \Re(\eta_1) = 0$$

- A periodic solution is called *unstable*, if:

$$|\mu_1| > 1 \quad \Leftrightarrow \quad \Re(\eta_1) > 0$$

In order to obtain an approximation of the monodromy matrix, (4.3) is substituted in (4.2):

$$\Theta'(\tau, \tau_0) = T_p A_\delta(\tau) \Theta(\tau, \tau_0) \tag{4.11}$$

with:

$$\Theta(\tau_0, \tau_0) = I$$

This initial value problem has to be integrated from $\tau = \tau_0$ to $\tau = \tau_0 + 1$. If the time discretization process, discussed in the previous chapter, is applied to calculate a periodic solution, the system matrix $A_\delta(\tau)$ is only available on discrete times τ_i. It is an obvious choice to integrate (4.11) with the same time step $\triangle\tau$, as was used in the calculation of the periodic solution.

Actually, in the computer program, which was developed to investigate the local stability of periodic solutions, the monodromy matrix was calculated by integrating the equations (4.1) using the constant-average-acceleration version of the Newmark method, see Bathe [1982] .

To give an illustrative example, the local stability of the harmonic periodic solutions shown in figure 3.6 is examined for excitation frequencies in the range 7.0-9.9 Hz. The branches a-b and d-f turned out to be stable, in contrast with the branch b-d.

In the figures of chapter 7 stable, marginally stable and unstable (branches of) periodic solutions will be indicated with the letters s, m and u respectively.

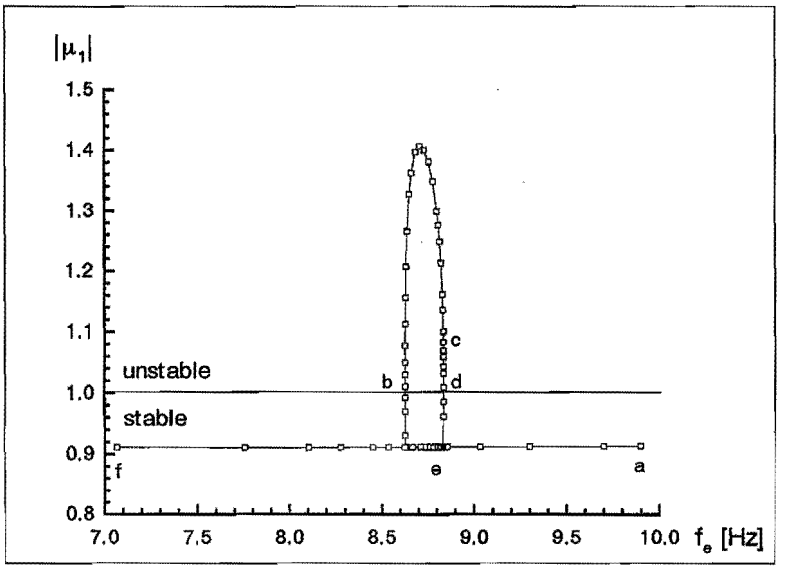

Figure 4.1: Investigation of the local stability of periodic solutions

Chapter 5

Local bifurcations

5.1 Introduction

In chapter 3 numerical methods have been described, by which branches of periodic solutions can be followed for varying values of a design variable r. In the previous chapter it has been shown, how the local stability of periodic solutions can be investigated. For some value $r = r_{bif}$ of the design variable a periodic solution can become marginally stable ($|\mu_1| = 1$). Simultaneously the Jacobian $J = \partial h/\partial z$ becomes singular. For $r = r_{bif}$ the system is not structurally stable, i.e. an infinitesimally small perturbation of the design variable can have drastic consequences for both the quantitative and qualitative steady-state behaviour. Bifurcation theory has to be applied to detect, in which way the changes in the quantitative and qualitative properties of the steady-state behaviour manifest themselves.

A value r_{bif}, at which a system is not structurally stable, is called a *bifurcation value.* When a bifurcation value is passed, the local stability of a steady-state, the number of (coexisting) steady-states and the type of steady-state behaviour may change. The bifurcation value and the marginally stable periodic solution z_{bif} together are called a *dynamic bifurcation point* of a periodic solution.

Bifurcation points are divided in *local* and *global* bifurcation points. In contrast to a global bifurcation point, a local bifurcation point can be identified by examining the evolution in time of small perturbations of periodic solutions as has been done in the previous chapter. In this chapter, we will use some useful parts from the local bifurcation theory. Global bifurcation points will not be discussed; for a detailed description of some global bifurcation points the reader is referred to Guckenheimer and Holmes [1983] and Thompson and Stewart [1986] .

Bifurcations are also divided in continuous and discontinuous bifurcations. A bifurcation is called *(dis)continuous*, if there exists a (dis)continuous path of attractors in the $[z^t, r]^t$-space, if the design variable r passes the bifurcation value r_{bif}. Discontinuous bifurcation points can be dangerous in practice, because the amplitude of steady-state solutions can suddenly change enormously. This explains why continuous (discontinuous) bifurca-

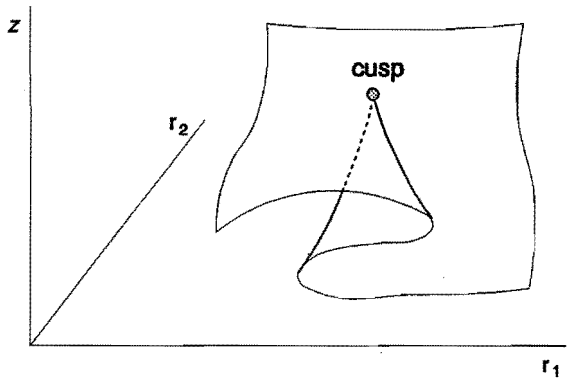

Figure 5.1: The cusp: a codimension 2 bifurcation point lying on a branch of codimension 1 cyclic fold bifurcation points

tions are sometimes called *safe (dangerous) boundaries.* If there exists a continuous version as well as a discontinuous version of the same type of bifurcation, the continuous version is called *supercritical* and the discontinous version is called *subcritical.*

The *codimension*, cod, of a bifurcation point is defined as the minimal number of design variables r, which is necessary to generically meet this bifurcation point in the augmented solution space spanned by $(z, r_1, \ldots, r_{cod})$. As an example figure 5.1 shows a part of the augmented solution space containing a codimension 2 cusp (or pitchfork) bifurcation point. Starting at an arbitrary solution, this bifurcation point in general will not be met by varying only one of the two design variables, in contrast to the codimension 1 cyclic fold bifurcation points on the thick branches. In the pf-method presented in chapter 3 only one design variable is varied at a time, so only codimension 1 bifurcation points will generically be met. Three local codimension 1 bifurcation points of periodic solutions are to be distinguished and will be discussed in the next sections: the *cyclic fold bifurcation*, the *flip bifurcation* and the *Neimark bifurcation.*

5.2 The cyclic fold bifurcation

The progress of a steady-state solution in the neighbourhood of a cyclic fold bifurcation point is sketched in figures 5.2a-5.2c. Just before the bifurcation point (figure 5.2a, $r = \bar{r_{bif}}, \mu_1 \uparrow 1$) two very nearby periodic solutions coexist; one of them is stable (thick closed curve), the other is unstable (thin closed curve). The curves of figure 5.2 have been drawn in the $2n_q + 1$ dimensional augmented state space. Time proceeds along the curves. The dashed curve represents a transient.

The towel-like planes in figure 5.2 are so-called *Poincaré sections.* The Poincaré section is defined as the $2n_q$ dimensional state space, *stroboscopically* lighted at times $t = (\phi_P/2\pi f_e) + i/f_e$ (i integer). In case the value of the phase angle ϕ_P is not explicitly

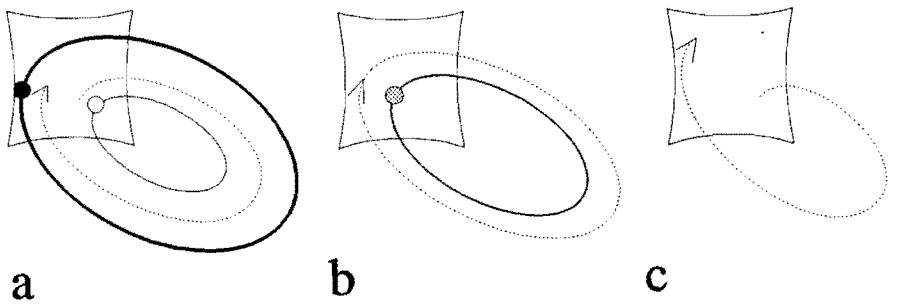

Figure 5.2: The progress of the cyclic fold bifurcation in the augmented state space

mentioned, its value is zero. As will appear later on, the Poincaré section is a very practical tool to recognize different types of steady-state behaviour. The Poincaré section of a (sub)harmonic solution of order $1/n$ ($n \in \mathbb{N}$) will contain n points (in figure 5.2a the black point belongs to the stable harmonic whereas the white point belongs to the unstable harmonic). The term Poincaré section will also be used in this thesis for the stroboscopically lighted twodimensional phase plane, which is actually a subspace of the Poincaré section.

At the bifurcation point (figure 5.2b, $r = r_{bif}, \mu_1 = 1$) the two solutions merge into one marginally stable periodic solution resulting in a single grey point in the Poincaré section. A trajectory, obtained via a perturbation of the marginally stable periodic solution in the direction of $\psi_{\mu 1}$, which is the first column of the matrix with eigenmodes Ψ_μ of the monodromy matrix (equation (4.6)), will be periodic with the same period as the marginally stable periodic solution. Just after the bifurcation point (figure 5.2c, $r = r_{bif}^+, \mu_1 \downarrow 1$) locally no periodic solution exists anymore. From the local information nothing can be said about the steady-state behaviour for $r = r_{bif}^+$: the steady-state attractor to which a trajectory will jump for $r = r_{bif}^+$ can differ much from the original periodic solution. Because of this jumping behaviour the cyclic fold bifurcation is a discontinuous bifurcation. Cyclic fold bifurcation points are also called *turning points*.

At the bifurcation point the Jacobian $J = \partial h/\partial z$ is singular. In general branch points $[z_s^t, r_s]^t$ will not lie so close to the turning point that the Jacobian becomes numerically singular; hence a turning point can be passed without difficulty in the path following process.

Figure 3.6 shows cyclic fold bifurcation points at f = 8.63 Hz (point b) and f = 8.83 Hz (point d). Investigation of the Floquet multipliers learns that harmonic solutions on the branch c-d are unstable and solutions on the branch d-e are stable. Figure 5.3 shows for 15 values of the excitation frequency the changes, which the Floquet multipliers undergo, in case the branch of figure 3.6 is travelled from point c via point d to point e. Because the Floquet multipliers occur in complex conjugate pairs, if they have an imaginary part unequal to zero, only the complex plane for non-negative imaginary values is shown. At

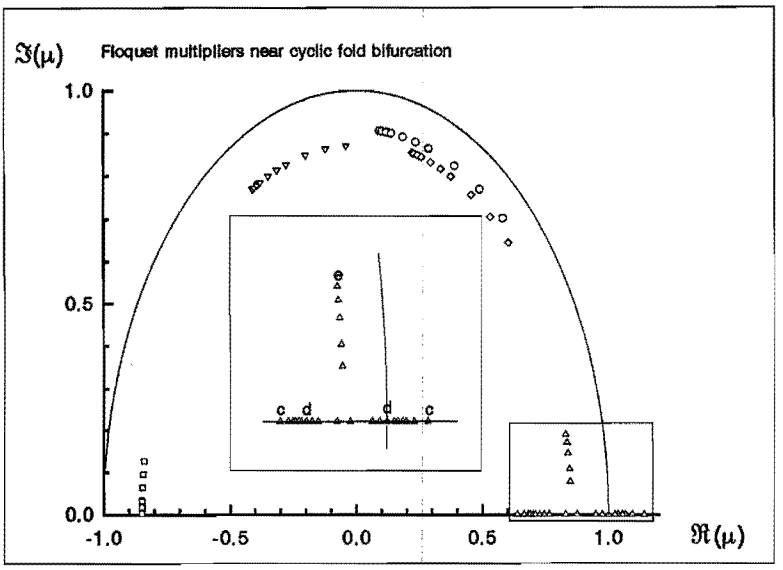

Figure 5.3: Floquet multipliers near the cyclic fold bifurcation point: $\mu_1 = +1$

point c and d six (out of ten) Floquet multipliers lie in this plane: four with non-zero imaginary parts (□, ▽, o and ◇) and two, which are real (both denoted by △). At point e only five Floquet multipliers with non-zero imaginary parts lie in this plane (one of the Floquet multipliers denoted by △ has disappeared because of its negative imaginary part). Note that at point d the unit circle in the complex plane is passed at the value +1.

5.3 The flip bifurcation

Figures 5.4a-5.4c show trajectories in the neighbourhood of a supercritical flip bifurcation point. Thus on both sides of the bifurcation value r_{bif} there exist locally stable steady-states. Just before the bifurcation point (figure 5.4a, $r = r_{bif}^{-}, \mu_1 \downarrow -1$) there exists one stable periodic solution. At the bifurcation point (figure 5.4b, $r = r_{bif}, \mu_1 = -1$), the magnitude of a perturbation in the direction of $\psi_{\mu 1}$ will take the same value after every period of the marginally stable solution. The orientation of the perturbation, however, will be opposite. So the perturbed solution has a double period and spans a Möbius strip, the center of which is the marginally stable periodic solution. This explains why the flip bifurcation is sometimes called a *period-doubling bifurcation* or a *subharmonic bifurcation*. After the bifurcation point (figure 5.4c, $r = r_{bif}^{+}, \mu_1 \uparrow -1$) the periodic solution with single period becomes unstable and two stable periodic solutions with double period, i.e. two 1/2 subharmonic solutions, arise. Actually the two stable periodic solutions are identical because they merge into one another if one solution is shifted over a single period. The stable 1/2 subharmonic solution results in two black points in the Poincaré

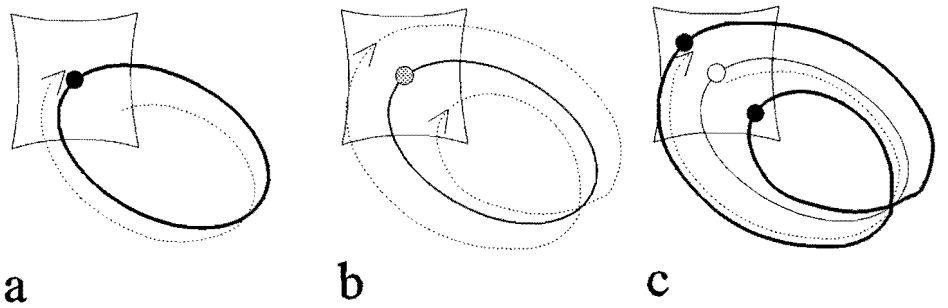

Figure 5.4: The progress of a supercritical flip bifurcation in the augmented state space

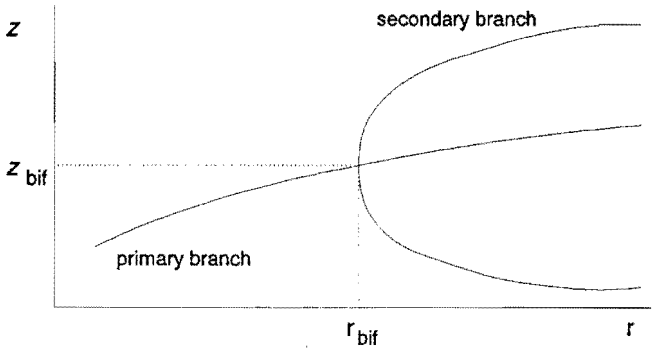

Figure 5.5: The primary and the secondary branch cross at the flip bifurcation point

section. The supercritical flip bifurcation is a continuous bifurcation. There also exist subcritical flip bifurcations, which are discontinuous. Figure 5.5 shows solution branches near a supercritical flip bifurcation point. The primary branch consists of solutions with a single period. This branch is crossed by a secondary branch with solutions with double period. If one looks for solutions with a single period, the path following process will follow the primary branch without difficulty, because at the flip bifurcation point the Jacobian is regular. If one looks for periodic solutions with double period, the solution space expands and the Jacobian becomes singular at the bifurcation point. If one starts on the primary branch, most of the time the bifurcation point still is passed without difficulty, if branch points do not lie too close to the bifurcation point. In general, however, the path following method will follow the primary branch after the bifurcation point. A numerical method developed by Rheinboldt [1978] can be applied to find a solution with double period on the secondary branch, starting from a point $[\tilde{z}^t_{\text{bif}}, \tilde{\mathrm{r}}_{\text{bif}}]^t$ on the primary branch lying close to the flip bifurcation point $[z^t_{\text{bif}}, \mathrm{r}_{\text{bif}}]^t$. At this bifurcation point, the null-space of $[\partial h/\partial z, \partial h/\partial \mathrm{r}]$

consists of $[p^t_{z,bif}, p_{r,bif}]^t$ and $[u^t, 0]^t$. The latter is perpendicular to the r-axis because of the symmetry in the flip bifurcation. An approximation $\tilde{u}$ of the null vector u of the Jacobian J can be found by applying the inverse power method to the regular Jacobian $\tilde{J}$ at the point $[\tilde{z}^t_{bif}, \tilde{r}_{bif}]^t$. Rheinboldt proved that under certain conditions there exists a (small) ϵ for which the following iterative scheme converges to a point on the secondary branch:

$$\begin{bmatrix} z_k \\ r_k \end{bmatrix} = \begin{bmatrix} \tilde{z}_{bif} \\ \tilde{r}_{bif} \end{bmatrix} + \epsilon\rho_k \begin{bmatrix} \partial z/\partial r(\tilde{z}_{bif}, \tilde{r}_{bif}) \\ 1 \end{bmatrix} + \frac{1}{2}\epsilon^2\rho_k^2 \begin{bmatrix} \partial^2 z/\partial r^2(\tilde{z}_{bif}, \tilde{r}_{bif}) \\ 0 \end{bmatrix} + \epsilon \begin{bmatrix} \tilde{u} \\ 0 \end{bmatrix} + \epsilon^2 \begin{bmatrix} \zeta_k \\ 0 \end{bmatrix} \tag{5.1}$$

$$\begin{bmatrix} \epsilon^2\tilde{J} & \epsilon d \\ 0^t & \epsilon\tilde{v}^t d \end{bmatrix} \begin{bmatrix} \zeta_{k+1} - \zeta_k \\ \rho_{k+1} - \rho_k \end{bmatrix} + \begin{bmatrix} h(z_k, r_k) \\ \epsilon\tilde{v}^t h(z_k, r_k) \end{bmatrix} = 0 \tag{5.2}$$

with:

$$\zeta_0 = 0 \quad ; \quad \rho_0 = 0 \quad ; \quad \tilde{u}^t\zeta_k = 0 \quad ;$$

$$\tilde{J}^t\tilde{v} = 0$$

d is a suitably chosen vector such that $\tilde{v}^t d \neq 0$. If a point on the secondary branch has been found, this branch with subharmonic solutions can be travelled again using the path following method.

A supercritical flip bifurcation point is met in the beam system introduced at page 51 with f_{ex} and f_n modified to:

$$f_{ex} = 200\cos(2\pi f_e t)$$

$$f_n = \begin{cases} 0 & \text{if } y \geq 0 \\ 10917y & \text{if } y < 0 \end{cases}$$

The stiffness of the one-sided linear spring, which is active only for negative displacements of the right end of the beam, is almost equal to the stiffness of the beam. The amplitude of the external load is just a scaling factor in this bilinear system. The linear, undamped system ($f_n = 0$) is modelled with four eigenmodes and one residual flexibility mode. Figure 5.6 shows Poincaré sections of harmonic and 1/2 subharmonic solutions for excitation frequencies f_e in the range 54-55 Hz. Investigation of the Floquet multipliers learns, that harmonic solutions are unstable in the range 54-54.4 Hz (points z-v) and stable in the range 54.5-55 Hz (points g-l), see figure 5.8. For excitation frequencies below the bifurcation value $f_{e,bif} \approx 54.46$ Hz there exists a branch with stable subharmonic solutions of order 1/2 (points a-f). Figure 5.7 shows the stable harmonic and 1/2 subharmonic solutions on both sides of the flip bifurcation point in the y-$\dot{y}$-f_e space. The numerical procedure of Rheinboldt was successfully applied to find a subharmonic solution on this branch.

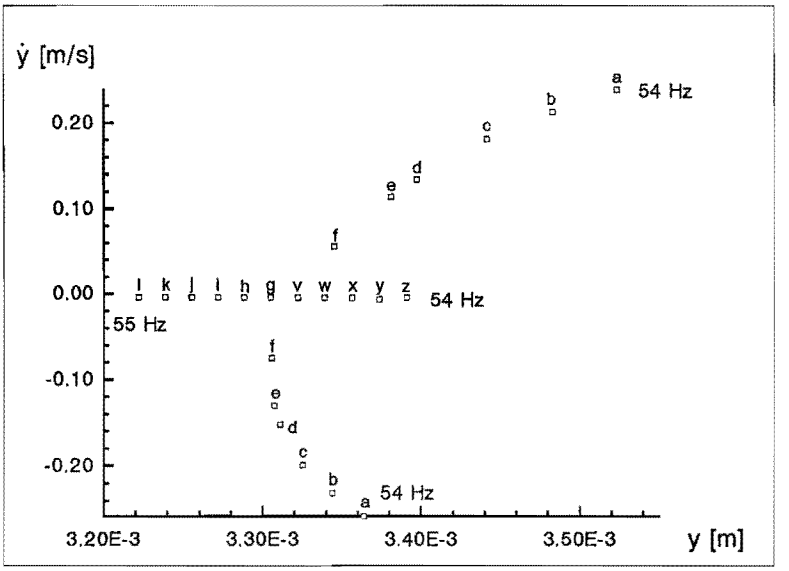

Figure 5.6: Poincaré sections on both sides of the flip bifurcation point

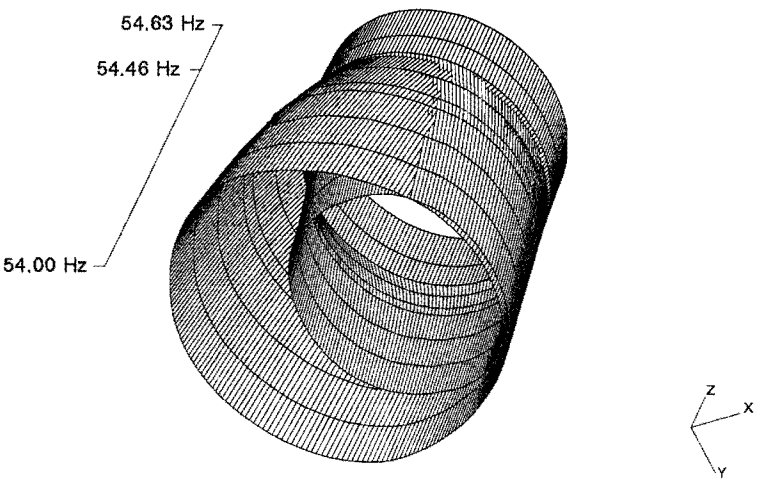

Figure 5.7: Stable harmonic and subharmonic solutions in y(X)-ẏ(Y)-f_e(Z) space

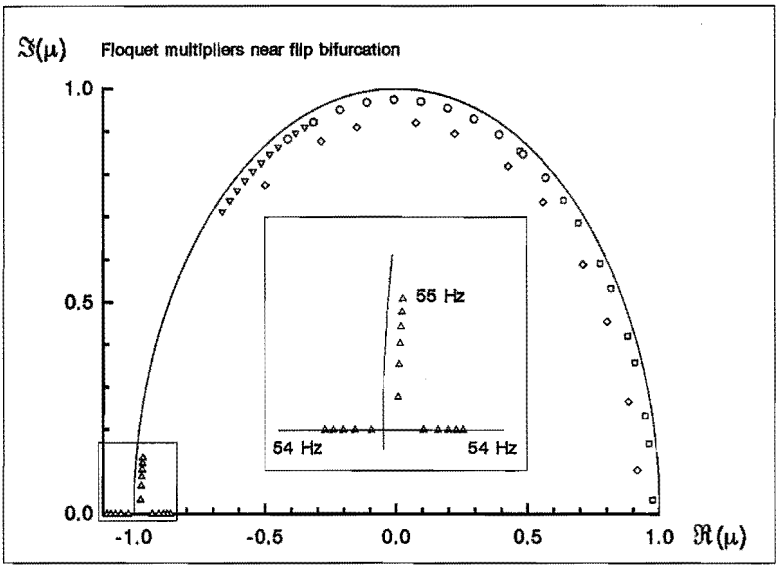

Figure 5.8: Floquet multipliers near the flip bifurcation point: $\mu_1 = -1$

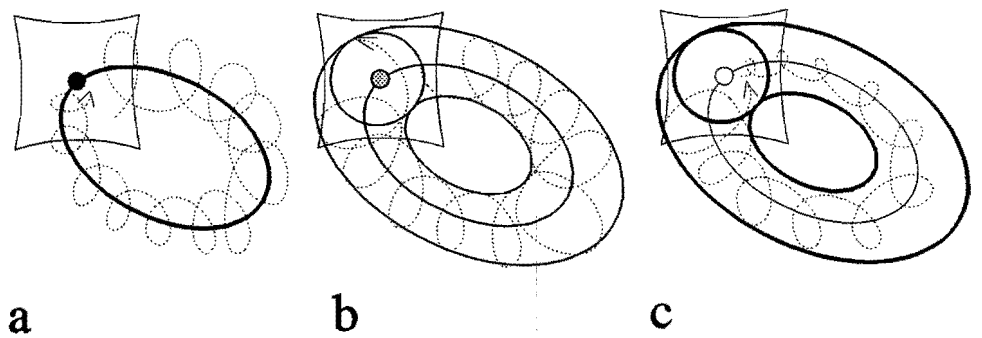

Figure 5.9: The progress of a supercritical Neimark bifurcation in the augmented state space

5.4 The Neimark bifurcation

The development of a supercritical Neimark bifurcation, also called a *secondary Hopf bifurcation*, is sketched in figures 5.9a-5.9c. Just before the bifurcation point (figure 5.9a, $r = r_{bif}^-$) there again exists one stable periodic solution. At the bifurcation point (figure 5.9b, $r = r_{bif}, \mu_1 = \bar{\mu}_2 = e^{\pi\varphi j}$), a solution, perturbed in the direction of $c\psi_{\mu 1} + \bar{c}\bar{\psi}_{\mu 1}$ will spiral around the marginally stable periodic solution with a frequency, which is unknown in advance. The magnitude of the perturbation will take the same value after every period of the marginally stable periodic solution. The orientation, however, is distorted over a certain angle. The perturbed solution moves over the surface of a torus, which has the marginally stable periodic solution as center. This surface will not be filled if $\varphi \in \mathbb{Q}$. Then after the bifurcation point a secondary branch of stable subharmonic periodic solutions will branch off the original branch of periodic solutions. The period of these periodic solutions can be very large. In general, however, $\varphi \in \mathbb{R} \setminus \mathbb{Q}$ and the surface of the torus will be filled. This means that a branch of stable quasi-periodic solutions arises after the bifurcation point. The quasi-periodic solution results in a closed curve in the Poincaré section (figure 5.9c, $r = r_{bif}^+$). The primary branch with periodic solutions becomes unstable after the bifurcation point. There also exist subcritical Neimark bifurcations.

A supercritical Neimark bifurcation point is found in the beam system defined at page 51 with f_{ex} and f_n modified to:

$$f_{ex} = 1000\cos(2\pi f_e t)$$

$$f_n = \begin{cases} 0 & \text{if } y \geqslant 0 \\ 76419y & \text{if } y < 0 \end{cases}$$

Again the amplitude of the external excitation is just a scaling factor and again the linear, undamped system is modelled by four eigenmodes and one residual flexibility mode. The symbols $\square$ in figure 5.10 show the Poincaré section of the stable quasi-periodic solution for $f_e = 228$ Hz (free frequency $f_f \approx 39.6$ Hz) and symbol $\triangle$ shows the Poincaré section of the stable harmonic solution for $f_e = 229$ Hz. For $f_e = 228$ Hz, the Poincaré section will eventually show a closed curve, which is the transection of a torus. In the quasi-periodic solution the first 7 successive symbols, obtained by integrating over 6 excitation periods, are connected by straight lines. The line corresponding to the first excitation period crosses the line corresponding to the sixth excitation period. In this way the free frequency is visualized: $228/6 \leqslant 39.6 \leqslant 228/5$. The quasi-periodic solution was calculated by solving an initial value problem ($s(0) = 0$). Harmonic solutions were calculated in the range 228-229 Hz using time discretization and path following. The Floquet multipliers in figure 5.11 show unstable harmonic solutions below the bifurcation value $f_{e,bif} \approx 228.55$ Hz and stable solutions above this excitation frequency.

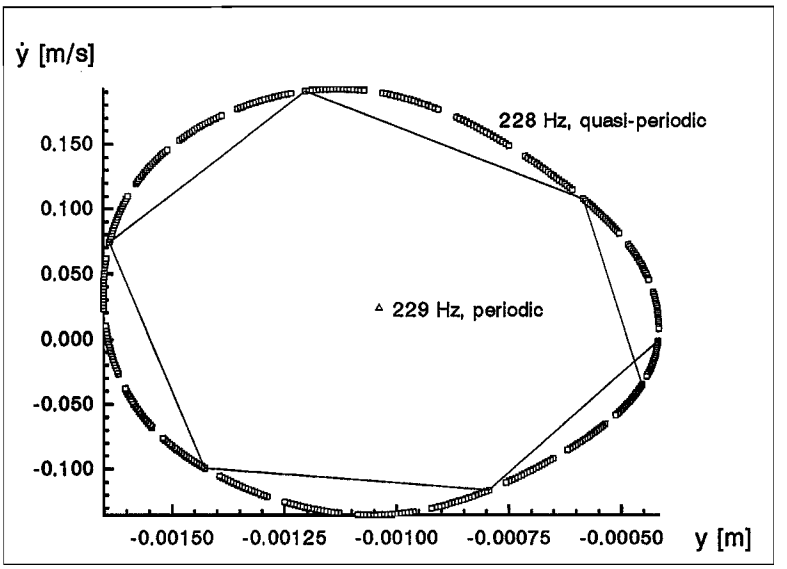

Figure 5.10: Poincaré sections of stable steady-states on both sides of the supercritical Neimark bifurcation point

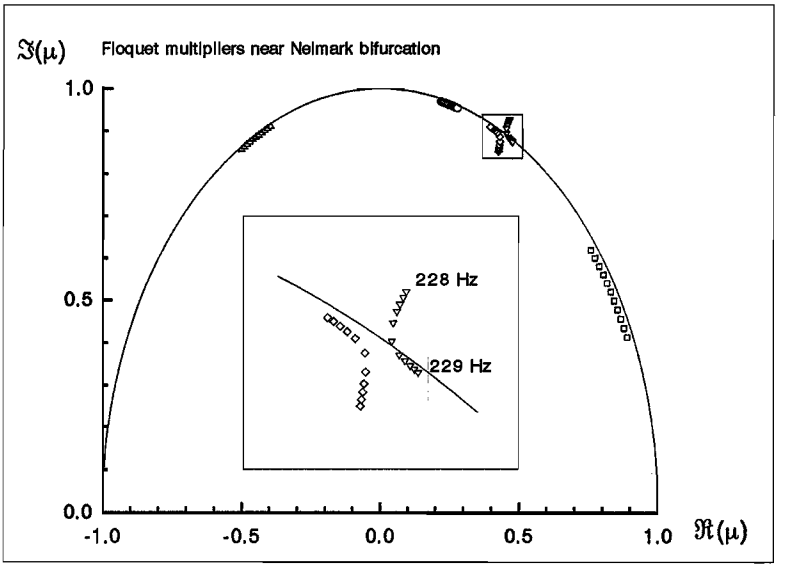

Figure 5.11: Floquet multipliers near the Neimark bifurcation point: $\mu_1 = \bar{\mu}_2$ (not visible) $= e^{\pi\varphi j}$

Chapter 6

Numerical integration

6.1 Introduction

Sometimes it is not easy to find a periodic attractor for certain values of the design variable using the time discretization method in combination with the path following method. In general subharmonic solutions of order 1/n will be more difficult to find using the damped Newton method (equation (3.24)) as n becomes large. Especially if subharmonic solutions and harmonic solutions coexist, it can be difficult to formulate an initial estimate z_0, which leads to the subharmonic solution instead of the harmonic solution. Naturally it is also possible, that for a given value of the design variable there exists no periodic attractor at all, but a quasi-periodic or chaotic attractor.

In case no periodic attractor can be found using time discretization and path following, numerical integration is applied to find an attractor. Two numerical integration algorithms of the NAG-library (NAG [1989]) have been used in this thesis to solve initial value problems: one is based on the Runge-Kutta-Merson method and the other on the Adams' method (Hall and Watt [1976]). The first is a variable-step method; the second is a variable-order, variable-step method. The desired accuracy can be given in terms of a number of correct significant digits or in terms of the number of correct decimal places. If a steady-state solution is calculated by means of numerical integration, *Lyapunov exponents* can be used to identify its character, which may be periodic, quasi-periodic or chaotic. Lyapunov exponents form the subject of the next section.

If a (sub)harmonic attractor is found from numerical integration and its order is not too small (say 1/10), the efficient path following method can again be applied to follow a branch of solutions, starting from the solution found with numerical integration.

6.2 Lyapunov exponents

Consider a solution $[s^t(t), \phi(t)]^t$ of the augmented system with an initial condition $[s_b^t, \phi_b]^t$ at $t = t_b$ lying in the domain of attraction of a steady-state solution. Assume that the transient has died out at $t = t_0 = t_b + t_t$. Now the equations of motion (2.46) are linearized

around the steady-state $s(t)$ for $t \geqslant t_0$:

$$\delta\dot{s}(t) = A_\delta(t)\delta s(t) \tag{6.1}$$

The system matrix $A_\delta(t)$, which was introduced in chapter 4, does not need to be periodic now. Given an initial condition $\delta s_0 = \delta s(t_0)$, the general solution of (6.1) is given by:

$$\delta s(t) = \Theta(t)\delta s_0, \tag{6.2}$$

where:

$$\Theta(t_0) = I$$

In order to compute approximations of Lyapunov exponents, which will be defined at the end of this section, firstly the following is noted: A direct computation of the fundamental solution $\Theta(t)$ would be a numerically unstable affair. Indeed, since (6.1) may be expected to have solutions of different growth behaviour, all (column) solutions of $\Theta(t)$ will asymptotically grow like the most dominantly growing one. This means that the directional information about the other fundamental modes is blurred (at least numerically). In order to avoid this problem, solutions are computed on smaller time intervals only, thereby retaining the proper information about the directions of the various fundamental modes through reorthonormalization. In fact a decomposition of the incremental fundamental matrix (over such an interval) is performed into an orthonormal matrix and an upper triangular matrix.

In practice we proceed as follows. Let the time t_k be defined as:

$$t_k := t_0 + kt_r, \tag{6.3}$$

where $k \in \{0, 1, 2, \ldots\}$ and t_r is some constant time increment, for example the period of the external excitation. Compute the fundamental solution $\Theta_1(t_1)$ of (6.1) on $[t_0, t_1]$ with $\Theta_1(t_0) = I$. Decompose this result as:

$$\Theta_1(t_1) = Q_1U_1, \tag{6.4}$$

where Q is an orthonormal matrix and U is an upper triangular matrix. Next compute a fundamental solution $\Theta_2(t_2)$ of (6.1) on $[t_1, t_2]$ with $\Theta_2(t_1) = Q_1$ and decompose:

$$\Theta_2(t_2) = Q_2U_2 \tag{6.5}$$

etc.. In general we thus have:

$$\Theta_k(t_k) = Q_kU_k. \tag{6.6}$$

Now for each k there clearly exists an upper triangular matrix W_k such that:

$$\Theta_k(t)W_k = \Theta(t), \qquad \forall t \tag{6.7}$$

It immediately can be seen that $W_1 = I$ since $\Theta_1(t_0) = \Theta(t_0)$. Next we find:

$$\Theta_2(t_1)U_1 = Q_1U_1 = \Theta_1(t_1) = \Theta(t_1) \Rightarrow W_2 = U_1 \tag{6.8}$$

$$\Theta_3(t_2)U_2U_1 = Q_2U_2U_1 = \Theta_2(t_2)U_1 = \Theta(t_2) \Rightarrow W_3 = U_2U_1 \tag{6.9}$$

In this way it easily follows that:

$$W_k = U_{k-1} \ldots U_1. \tag{6.10}$$

Concluding, we see that the increment over the interval $[t_0, t_k]$ can be obtained in a stable, factored form as:

$$\Theta(t_k) = Q_kU_k \ldots U_1. \tag{6.11}$$

Under fairly general, and often prevailing, conditions it can be shown that the matrices U_k contain asymptotically correct information about the growth of the fundamental modes on their diagonal in an ordered way, i.e. in nonincreasing modulus from left to right (Mattheij [1985]). The exponential growth of fundamental mode i is expressed by Lyapunov exponent λ_i, which is defined as:

$$\lambda_i = \lim_{t_k \to \infty} \frac{1}{t_k - t_0} \log_2 |U_{k,ii} \ldots U_{1,ii}|, \qquad i = 1, \ldots, 2n_q \tag{6.12}$$

$$\lambda_i \geqslant \lambda_{i+1}. \tag{6.13}$$

In (6.12) $U_{k,ii}$ is the i-th diagonal element of the upper triangular matrix U_k (Söderlind and Mattheij [1985]). A $\lambda_i > 0$ ($\lambda_i < 0$) can eventually result in an overflow (underflow) on a digital computer in the calculation of the product $U_{k,ii} \ldots U_{1,ii}$. This problem can be circumvented by calculating an approximation $\lambda_i(t_k)$ in the following way:

$$\lambda_i(t_k) = \frac{1}{kt_r} \sum_{j=1}^{k} \log_2 |U_{j,ii}|. \tag{6.14}$$

For reasons of numerical stability the QU-decompositions above should be performed through Householder's reflections or Givens' rotations (Bathe [1982]). In lower dimensional cases, however, a Gram-Schmidt reorthonormalization - though numerically less desirable - can be used in view of the relatively larger tolerances. Note that if the convergence rate of Lyapunov exponents is low, calculations can become very expensive, since the number of first order differential equations that must be solved simultaneously is equal to $2n_q(1 + 2n_q)$.

Because the trajectory $s(t)$ is an attractor, the volume of the $2n_q$-dimensional cube, spanned by the columns of $\Theta(t_0) = I$ must monotonically decrease as time proceeds, which implies:

$$\sum_{i=1}^{2n_q} \lambda_i < 0. \tag{6.15}$$

6.3 Characterization of attractors

If the attractor is a periodic solution, an arbitrary perturbation will damp out exponentially, which means that all Lyapunov exponents must be negative:

$$\lambda_i < 0, \quad \forall i \tag{6.16}$$

By comparing the way, in which Floquet multipliers and Lyapunov exponents are defined, the following relationship can be derived, if the attractor is periodic:

$$|\mu_i| = 2^{\lambda_i T_p} \tag{6.17}$$

As an example, consider the harmonic solution of the two-point boundary value problem:

$$\ddot{q} + 0.1\dot{q} + q + 0.7q^3 = \cos(2t) \tag{6.18}$$

with:

$$q(0) = q(\pi), \quad \dot{q}(0) = \dot{q}(\pi)$$

This periodic solution can also be obtained by solving the initial value problem (6.18) with initial conditions:

$$q(0) = \dot{q}(0) = 0$$

At first an $O(\Delta\tau^4)$ approximation of the solution of the two-point boundary value problem was calculated by application of the deferred correction method of chapter 4 ($n_\tau = 400$); calculation of the Floquet multipliers showed that the solution was stable: $|\mu_1| = |\mu_2| = 0.855$. Subsequently a point on the the harmonic attractor was calculated by solving the initial value problem using the Runge-Kutta-Merson algorithm (required precision: 7 significant digits). After 1000 excitation periods the transient was assumed to have damped out ($t_t = 1000\pi$). Then the linearized differential equations needed to calculate the Lyapunov exponents were added and the integration was continued over 4000 excitation periods. The time histories of the resulting Lyapunov exponents are shown in figure 6.1. Both Lyapunov exponents converged to the value -0.0721. In figure 6.1 equation (6.17) is verified. Note that the Lyapunov exponents and the quotient of the linear viscous damping coefficient ($b = 0.1$) and the mass ($m = 1$) are related by:

$$b/m = -(\lambda_1 + \lambda_2)\ln 2 \tag{6.19}$$

Incidentally, this relation shows that the Lyapunov exponents are independent of of the stiffness. Of course, the transient stage could have been skipped over in the numerical integration calculation, because a point of the harmonic attractor could have been taken from the solution of the two-point boundary value problem.

If the attractor is a quasi-periodic solution of dimension d ($d \in \mathbb{N} \setminus 1$), i.e. the solution contains d incommensurate frequencies corresponding to d time scales, the first $d - 1$ Lyapunov exponents will be equal to zero:

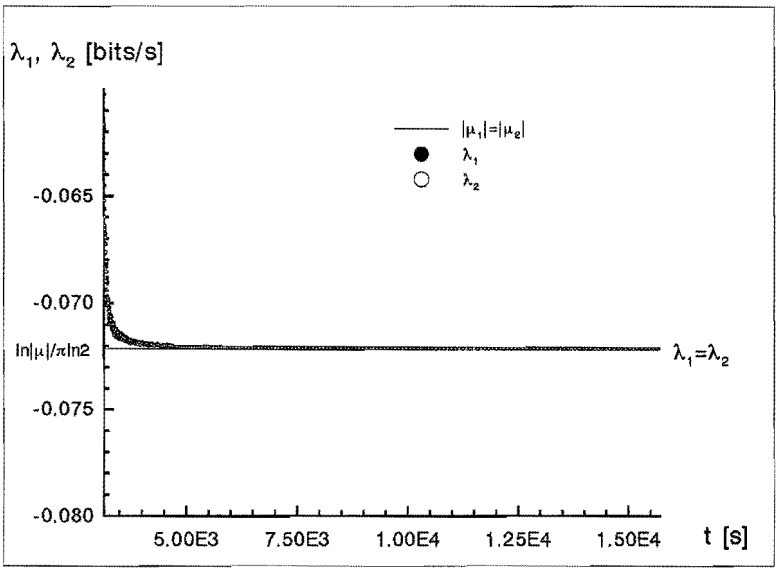

Figure 6.1: Lyapunov exponents of a periodic attractor

$$\lambda_i = 0, \quad i \in \{1, \ldots, d-1\} \tag{6.20}$$

$$\lambda_i < 0, \quad i \in \{d, \ldots, 2n_q\} \tag{6.21}$$

The phase of one time scale will be forced by the external load. The phases of the other time scales can be chosen freely. This implies that there exist $d-1$ directions in the phase space, which correspond to a phase shift over a free time scale. A perturbation of the quasi-periodic solution in such a direction neither damps out nor grows and leads to a Lyapunov exponent equal to zero. The converse is not true; a Lyapunov exponent equal to zero does not necessarily imply quasi-periodic behaviour, it can also be caused by a marginally stable periodic solution.

In case of a chaotic attractor, see page 3, at least one Lyapunov exponent will be positive:

$$\lambda_1 > 0 \tag{6.22}$$

So a trajectory $s(t) + \delta s(t)$ ($\delta s(t_0)$) is an infinitesimally small perturbation), will diverge, on average of time, from the trajectory $s(t)$ on the chaotic attractor with exponential rate for $t \geqslant t_0$. And yet the trajectory $s(t) + \delta s(t)$ will converge to the same chaotic attractor, i.e. in the limit $t \to \infty$ the trajectories $s(t)$ and $s(t) + \delta s(t)$ fill the same subspace in the state space. This seems to be a contradiction, but is possible, however, due to a kind of stretching and folding process.

In case of a chaotic attractor, the quotient of the level of accuracy (in [bits]), with which initial conditions are known, and λ_1 [bits/s] gives the mean time, after which nothing can

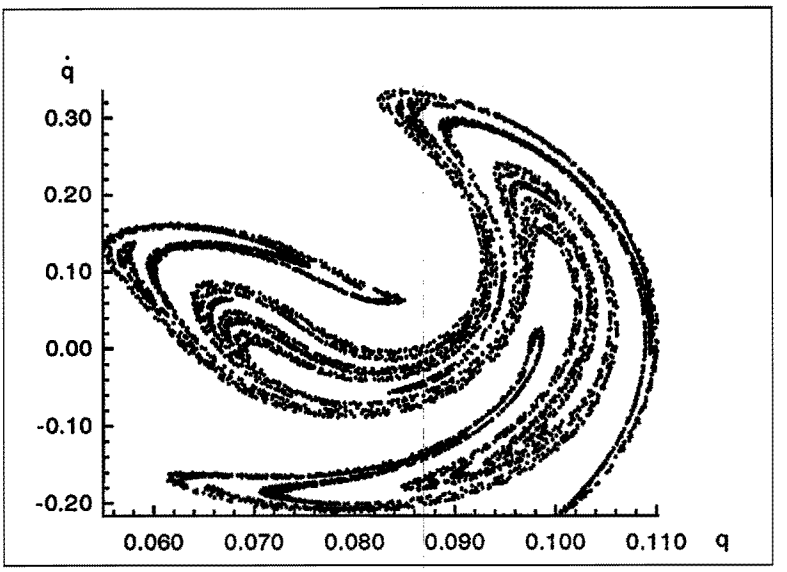

Figure 6.2: Poincaré section of a chaotic attractor

be said about the position of the trajectory on the attractor, even if it would be possible to integrate system equations exactly. This also holds for non-exact integration, as long as the accuracy of the integration process exceeds the accuracy, with which initial conditions are known. If the level of accuracy of the initial conditions exceeds the precision level, with which they can be represented in a digital computer, the latter will be decisive. With periodic solutions, λ_1 determines the rate of loss of information about the initial conditions.

Now, consider the attractor of the initial value problem:

$$\ddot{q} + 0.1\dot{q} + q + 3600q^3 = \cos(2t) \tag{6.23}$$

with:

$$q(0) = \dot{q}(0) = 0$$

A point on the attractor was determined by integrating very accurately (required precision: 12 decimal places) over 1000 excitation periods, after which the transient was assumed to be damped out. Then the attractor and the Lyapunov exponents were calculated simultaneously by integrating over 9000 excitation periods. Figure 6.2 shows the Poincaré section of the attractor. In figure 6.3 it can be seen that the first Lyapunov exponent converges to a positive value ($\lambda_1 \approx 0.225$, $\lambda_2 \approx -0.369$), indicating that the attractor has a chaotic nature. Consequently, the numerical method of section 3.2 will fail in this case. Note that the rate of convergence of the Lyapunov exponents is much lower than in figure 6.1. Note further that the Lyapunov exponents still satisfy equation (6.19).

The following state is a point of the Poincaré section shown in figure 6.2 and is thus a point on the chaotic attractor:

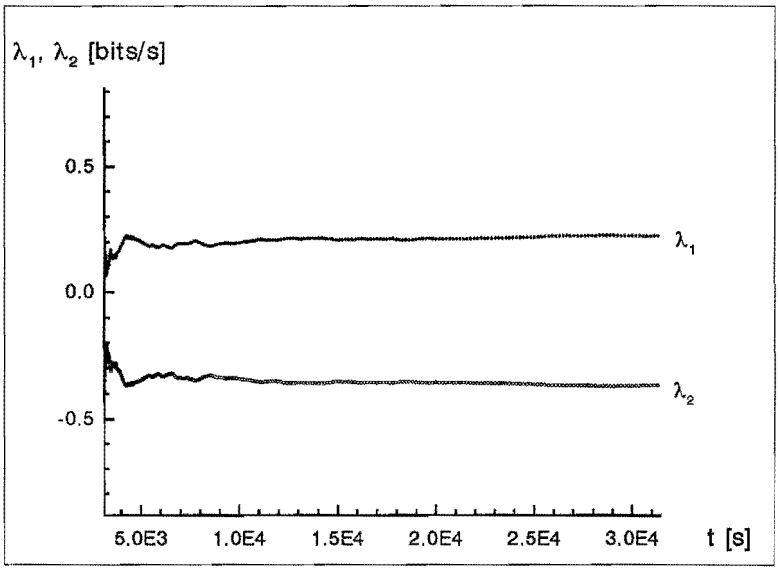

Figure 6.3: Lyapunov exponents of a chaotic attractor

$$s_{01} = \begin{bmatrix} q_{01} \\ \dot{q}_{01} \end{bmatrix} = \begin{bmatrix} 0.108690048277 \\ 0.102062238976 \end{bmatrix}$$

It is important to realize that q_{01} is very close to the maximum displacement (≈ 0.110) observed. This means that the first decimal of q_{01} is the most significant decimal. Now consider a perturbation of this state:

$$s_{02} = \begin{bmatrix} q_{02} \\ \dot{q}_{02} \end{bmatrix} = \begin{bmatrix} 0.108700000000 \\ 0.102062238976 \end{bmatrix}$$

The perturbation ($\approx 10^{-5}$) must be multiplied by $10^4 \approx 2^{13.3}$ to affect the most significant decimal. So if s_{01} and s_{02} are taken as initial conditions, on average the two resulting trajectories will have little in common after $13.3/0.225 \approx 59$ s, besides the fact that they are both on the chaotic attractor. Put differently, information about the initial conditions is totally lost after this time. This is confirmed by figure 6.4, which shows the time histories of the resulting displacements (required precision during integration: 12 decimal places). The solid line corresponds to initial condition s_{01}; the dotted line to initial condition s_{02}.

An attractor can also be characterized by its dimension. One of the concepts of dimension is the *Hausdorff dimension*:

$$D_H = \lim_{\delta \to 0} \frac{\ln N(\delta)}{-\ln \delta} \tag{6.24}$$

where $N(\delta)$ is the number of $2n_q + 1$ dimensional cubes of side δ that are required to cover the attractor in the augmented state space. According to this definition a static

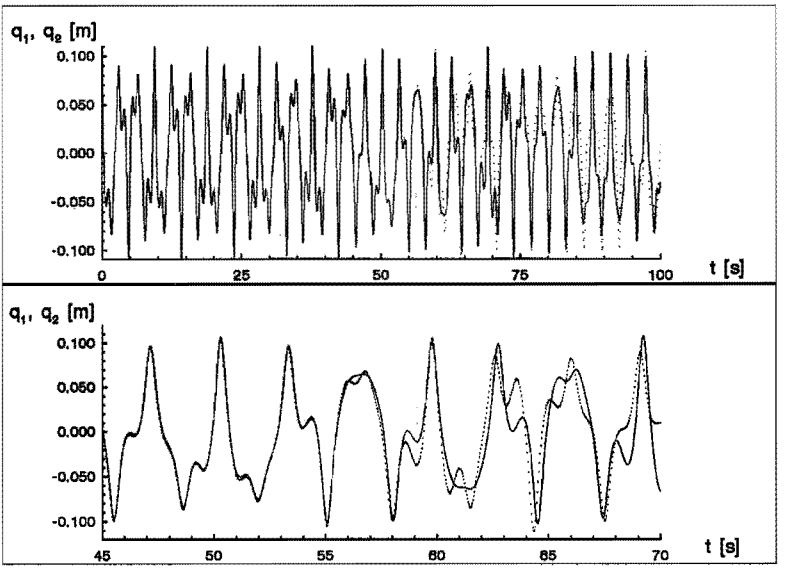

Figure 6.4: The most significant decimal is affected after 59 s

equilibrium point has dimension 0, a periodic attractor has dimension 1, a quasi-periodic attractor has an integer dimension greater than 1 and a chaotic attractor has a non-integer dimension. In practice it is inconvenient to use this definition to calculate the dimension of an attractor. Kaplan and Yorke [1978] conjectured that the Hausdorff dimension is equal to the *Lyapunov dimension* D_λ, which can be calculated from the Lyapunov exponents for maximal $D_{\lambda int}$:

$$D_{\lambda frac} = (\sum_{i=1}^{D_{\lambda int}} \lambda_i)/|\lambda_{D_{\lambda int}+1}| \geqslant 0 \tag{6.25}$$

$$D_\lambda = D_{\lambda int} + D_{\lambda frac} \tag{6.26}$$

This definition holds for Lyapunov exponents calculated in the $2n_q + 1$ dimensional augmented state space, which includes the phase angle $\phi(t)$ of the external load, which is related to time, see (1.5). In this case one of the Lyapunov exponents will always be equal to zero, see Haken [1983] , because there is no exponential growing or shrinking along the trajectory. If Lyapunov exponents are calculated in the $2n_q$ dimensional space as is done in section 6.2, equation (6.26) will give the dimension of the Poincaré section of the attractor. This dimension increased by 1 is equal to the dimension of the attractor. As an example, the Lyapunov dimension of the Poincaré section shown in figure 6.2 is equal to 1.61 and the Lyapunov dimension of the corresponding attractor is 2.62.

Chapter 7

Applications: beam with nonlinear support

7.1 Introduction

In this chapter the steady-state behaviour of the beam system with local nonlinear supports introduced in section 2.7 is investigated using the numerical methods developed in the previous chapters. The supporting linear spring is absent ($k = 0$ N/m). The length of the beam is $l = 1.5$ m. The amplitude of the external excitation is $F_{dy} = 19.693$ N:

$$f_{ex} = 19.693 \cos(2\pi f_e t + \phi_e)$$

The phase angle ϕ_e is equal to zero in all calculations, unless its value is explicitly mentioned. Three types of local nonlinearities are considered: a stiffening spring of Duffing type (stiffness $k_3 \geqslant 0$), a stiffening spring of Duffing type, which acts only under pressure (stiffness $k_{3p} \geqslant 0$), and a linear spring, which acts only under pressure (stiffness $k_p \geqslant 0$):

$$f_n = \begin{cases} k_3 y^3 & \text{if } y \geqslant 0 \\ (k_3 + k_{3p}) y^3 + k_p y & \text{if } y < 0 \end{cases}$$

Firstly, the effects of these three nonlinear supports on the steady-state behaviour will be investigated separately, i.e. only one of the variables k_3, k_{3p} and k_p is unequal to zero. Then attention will be paid to the combination of the two springs with stiffnesses k_3 and k_p.

The five design variables of the system are, next to k_3, k_{3p} and k_p, the excitation frequency f_e of the external load and the damping constant b of the linear damper.

Single dof as well as multi-dof models will be investigated. In the single dof model the displacement field of the beam is approximated by the first free-interface eigenmode. In almost all calculations of the single dof model the same number of discretization points is used: $n_\tau = 600$. Exceptions are explicitly mentioned. In the single dof model the five just mentioned design variables can be expressed in terms of the five dimensionless design variables μ, μ_p, α, ξ and Ω defined in appendix C ($m = 1.0358$ kg, $k = 3282.2$ N/m):

$k_3 = 9.1174\,10^7\,\mu$

$k_{3p} = 9.1174\,10^7\,\mu_p$

$k_p = 3282.2\,\alpha$

$b = 116.61\,\xi$

$f_e = 8.9592\,\Omega$

Subsequently four dof models will be used to investigate the influences of the higher eigenmodes on the steady-state behaviour in the low frequency range. In this four dof model the displacement field of the beam is approximated by three free-interface eigenmodes and one residual flexibility mode. An eight dof model (seven free-interface eigenmodes plus one residual flexibility mode) will be used to verify some of the results obtained with the four dof model. The eigenfrequencies of the reduced linear beam models are given in table 2.6 on page 41. In the multi-dof models also use will be made of dimensionless quantities of the single-dof system, in which only the first free interface eigenmode is used to describe the displacement field of the beam. In comparison with absolute quantities like k_3, k_{3p}, k_p and b they give more insight in the extent of nonlinearity and damping for frequencies in the neighbourhood of the first harmonic resonance peak.

7.2 Support by a stiffening spring

7.2.1 Single dof model: weakly nonlinear, undamped

The undamped case is studied to illustrate the different types of resonances occurring in a Duffing system. Asymptotically stable steady-state solutions do not exist, because the system is conservative. For the same reason, bifurcations in the system do not fall under the three types of local bifurcations, which were discussed in chapter 5. Therefore, in this subsection bifurcations in the system will be noticed, but they will not be named. Figure 7.1 shows the amplitude-frequency plot of the system ($\mu = 0.05$, $\mu_p = 0$, $\alpha = 0$, $\xi = 0$). The branches with harmonic solutions show (super)harmonic resonance peaks, which start at frequencies slightly above f_1/n ($n \in \mathbb{N}$, $f_1 = 8.9592$ Hz). From left to right figure 7.1 shows only the fifth, third and second superharmonic resonance peak (n=5,3,2) and finally the harmonic resonance peak (n=1). In the figure it is hardly visible, but for n=1,3,5 the resonance peaks consist of two unconnected branches, which amplitudes grow to infinity. The upper branch is marginally stable, whereas the lower branch is unstable. In the second superharmonic resonance peak, the marginally stable upper branch as well as the unstable lower branch are formed by two solution branches, which have exact the same absolute amplitudes. So the second resonance peak, which might appear as one branch in figure 7.1, actually consists of four branches. In contrast to the other harmonic solutions shown in figure 7.1, a periodic solution q_1 of the second superharmonic resonance peak is not point-symmetric: $q_1(t) \neq -q_1(t + T_e/2)$. However, two different solutions q_1 and q_2, which form

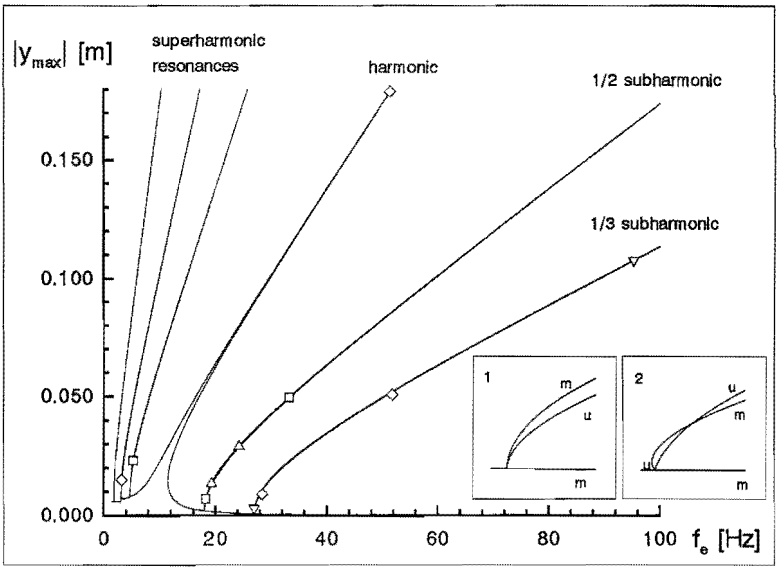

Figure 7.1: Resonances in the undamped, single dof Duffing system

the same point on the marginally stable curve or the unstable curve of the second harmonic resonance peak, are point-symmetric with respect to each other: $q_1(t) = -q_2(t + T_e/2)$. These symmetry aspects will be illustrated with a figure in the next subsection. From a geometrical point of view, it is logical that the not point-symmetric solutions occur in pairs, because the excitation force is point-symmetric ($f_{ex}(t) = -f_{ex}(t + T_e/2)$) just like the nonlinearity, which is an uneven function ($f_n(y) = -f_n(-y)$). The four branches, which form the second superharmonic resonance peak, are connected at one bifurcation point, where they arise from the branch containing the marginally stable harmonic resonance peak and the unstable third superharmonic resonance peak.

Apart from the branches with harmonic solutions there exist branches with subharmonic solutions of order $1/n$ ($n \in \mathbb{N} \setminus 1$), which start at frequencies slightly above nf_1. Figure 7.1 shows the subharmonic resonance peaks of order $1/2$ and $1/3$ only. The amplitudes of these peaks also grow to infinity. The branches with subharmonic solutions bifurcate from the marginally stable low amplitude branch with harmonic solutions. Inset 1 of figure 7.1 shows the bifurcation of the $1/2$ subharmonic branches and inset 2 the bifurcation of the $1/3$ subharmonic branches. Inset 1 shows that the upper branch of the $1/2$ subharmonic resonance peak is marginally stable and the lower branch is unstable. With respect to the point-symmetry the same holds for the $1/2$ subharmonic solutions as for the harmonic solutions on the second superharmonic resonance peak. So in fact both the marginally stable curve and the unstable curve again originate from two branches of solutions. Inset 2 shows that for higher values of the excitation frequency the upper $1/3$ subharmonic branch is unstable and the lower $1/3$ subharmonic branch is marginally stable.

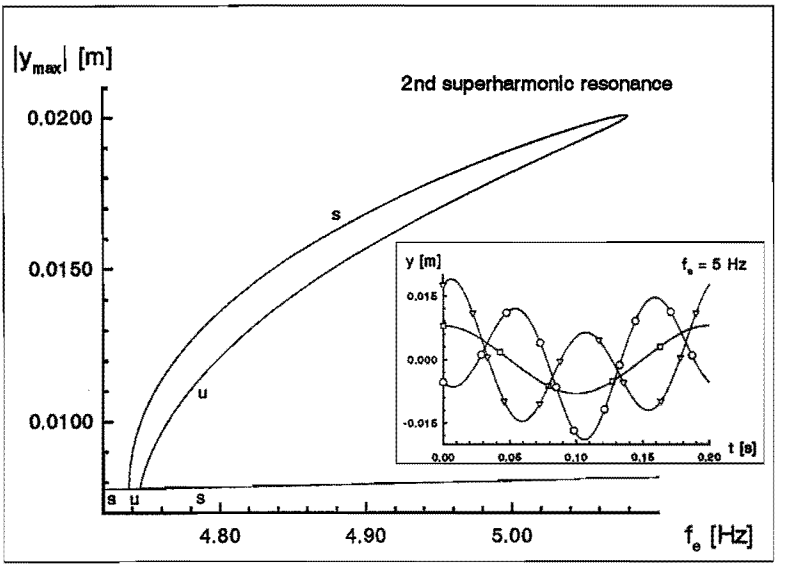

Figure 7.2: The second superharmonic resonance peak arises via two pitchfork bifurcations

7.2.2 Single dof model: weakly nonlinear, slightly damped

Addition of damping makes the height of resonance peaks finite. The branches which form the (super)harmonic resonance peaks are connected by means of cyclic fold bifurcation points. The upper branches, which were marginally stable in the undamped case, are stable now. The lower branches remain unstable. The stable and unstable branches, which form the second superharmonic resonance peak, do not bifurcate from the same point on the low amplitude harmonic branch as they did in the undamped case, see figure 7.2 ($\xi = 0.0002$). The two bifurcation points at $f_e = 4.738$ Hz and $f_e = 4.745$ Hz are symmetry-breaking pitchfork bifurcation points of codimension 2. The left pitchfork bifurcation point is supercritical; the right pitchfork bifurcation point is subcritical. Although pitchfork bifurcation points are not generic, if only one design variable (here the excitation frequency) is varied, they are occasionally seen according to Seydel [1988] due to a perfect symmetry in the nonlinearity, which is the case in the system under consideration. If the symmetry in the nonlinearity is only very slightly destroyed, the left pitchfork bifurcation point will totally disappear and the right pitchfork bifurcation point will change to a codimension 1 cyclic fold bifurcation point; the pitchfork bifurcation points are not structurally stable. For $f_e = 5$ Hz the time histories of the three stable solutions of figure 7.2 are shown in its inset. Note that the low amplitude stable solution is point-symmetric with respect to the origin and the the two stable high amplitude solutions are point-symmetric with respect to each other.

Due to damping the branches with subharmonic solutions do not bifurcate anymore from the low amplitude branch with harmonic solutions (Tsuda et al. [1984]): the sub-

harmonic branches become closed curves (islands) and only exist in a certain frequency interval. The boundaries of such an interval are formed by two cyclic fold bifurcation points, where the stability of the subharmonic solutions changes.

The symbols in figure 7.1 mark the cyclic fold bifurcation points for different values of damping: $\xi = 0.0001(\square), \xi = 0.0003(\triangle), \xi = 0.001(\triangledown)$ and $\xi = 0.003(\diamond)$. Note that an increase of damping destroys the second superharmonic resonance peak and 1/2 subharmonic solutions first, subsequently the third superharmonic resonance peak and 1/3 subharmonic solutions and finally the harmonic resonance peak. Obviously, the reason for this behaviour is that the nonlinearity is a function with an uneven power.

For weakly nonlinear systems there exist a number of classical analytical methods such as perturbation methods and averaging methods, which can be used to determine periodic solutions (Jordan and Smith [1977] and Nayfeh and Mook [1979]). For strongly nonlinear systems or in the case of multi-dof these methods become cumbersome. However, in some recent papers (Burton and Hamdan [1983] , Burton [1984] and Burton and Rahman [1986]) a variation on the method of multiple scales (a perturbation method) is presented, which is also able to calculate the harmonic resonances of strong nonlinear single-dof systems. In appendix E the method of harmonic balance (an averaging method) is used to verify some of the numerical results of the amplitude-frequency plot for $\mu = 0.05$ and $\xi = 0.003$.

7.2.3 Single dof model: strongly nonlinear, slightly damped

Figure 7.3 shows the influence of increasing the cubic stiffness μ on the superharmonic resonances (n uneven) for a fixed value of the damping: $\xi = 0.01$. Obviously, in general the amplitude of the solutions decreases because the system becomes more stiff. The n-th superharmonic resonance peak, which can be found near frequencies f_1/n in a weakly nonlinear system, moves to a higher frequency. The amplitudes of the higher superharmonic peaks (n=5,7,9,...) gain in height in comparison with the third superharmonic resonance peak. For $\mu = 0.05$ the amplitude-frequency plot in figure 7.3 shows no bifurcation points; all solutions are stable. For higher values of μ cyclic fold bifurcation points are introduced and the superharmonic resonance peaks widen. For $\mu = 0.70$ cyclic fold bifurcation points are found at $f_e \approx 2.306$ Hz and $f_e \approx 2.309$ Hz (n=5 peak) and at $f_e \approx 3.92$ Hz and $f_e \approx 3.92$ Hz (n=3 peak). For $\mu = 7.00$ they are found at $f_e \approx 1.77$ Hz and $f_e \approx 1.80$ Hz (n=9 peak), at $f_e \approx 2.25$ Hz and $f_e \approx 2.32$ Hz (n=7 peak), at $f_e \approx 3.11$ Hz and $f_e \approx 3.26$ Hz (n=5 peak) and at $f_e \approx 5.18$ Hz and $f_e \approx 5.69$ Hz (n=3 peak). In the frequency ranges, where three periodic solutions exist, the maximum amplitude solution appeared to be unstable.

Figure 7.4 shows the influence of increasing the cubic stiffness on the 1/3 subharmonic resonances for $\xi = 0.01$. Again the amplitude of the solutions decreases. The frequency interval, in which subharmonic solutions can be found, grows for increasing μ. The left boundary of the frequency interval does hardly change in contrast with the right boundary of the frequency interval.

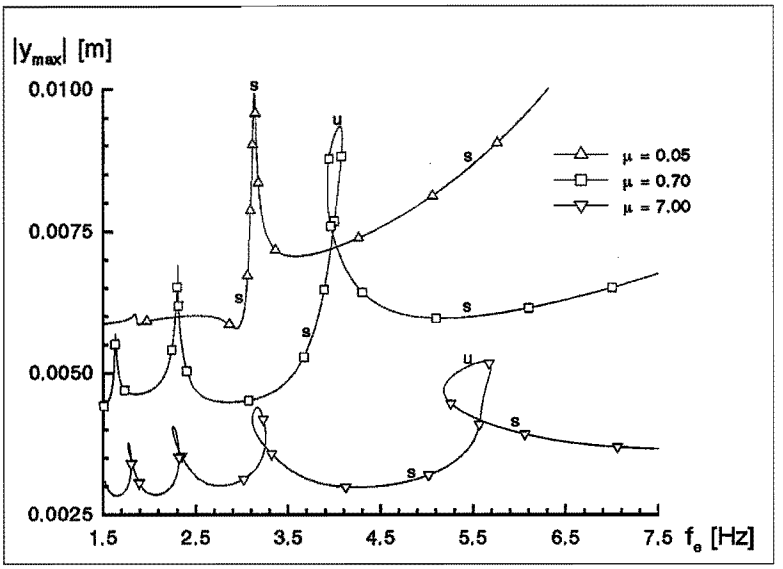

Figure 7.3: Influence of cubic stiffness on superharmonic resonances

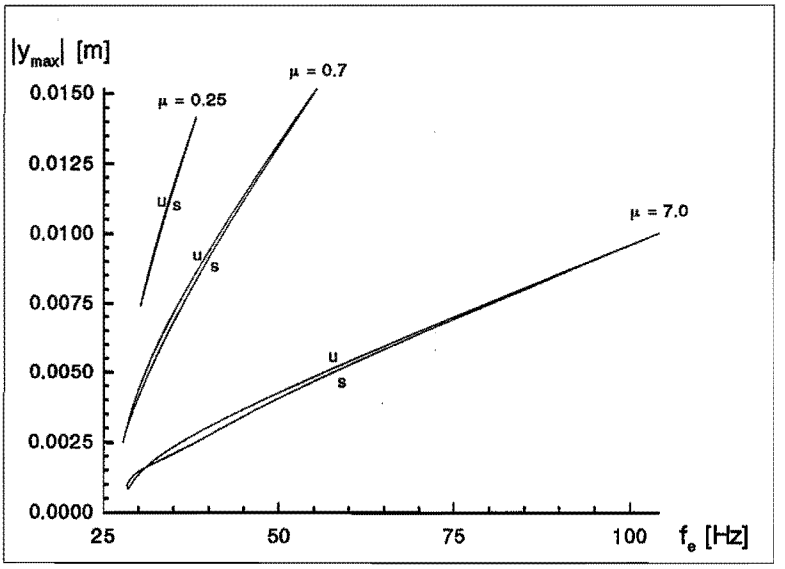

Figure 7.4: Influence of cubic stiffness on 1/3 subharmonic resonances

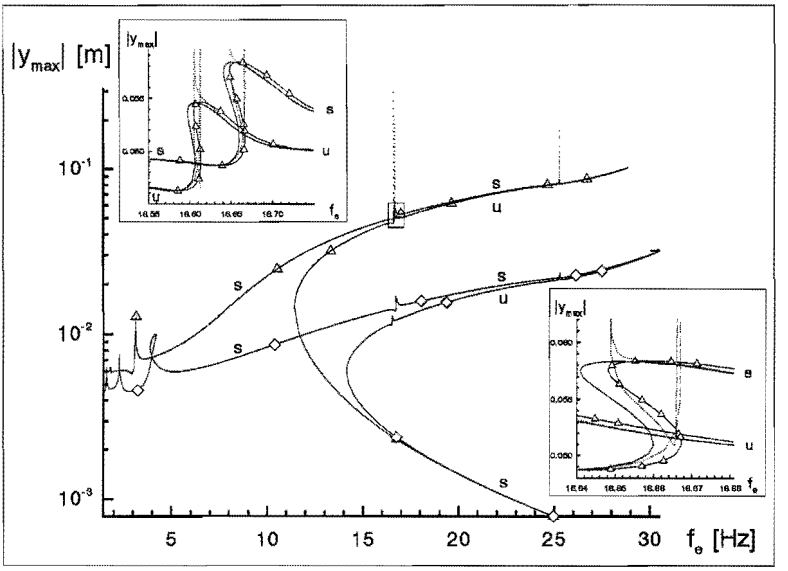

Figure 7.5: Internal resonances on the first harmonic resonance peak in the four dof model ($\mu = 0.05$ ($\triangle$), $\mu = 0.7$ ($\diamond$))

7.2.4 Four dof model: slightly damped

Figure 7.5 shows the amplitude-frequency plot of harmonic solutions of the slightly damped ($\xi = 0.005$) four dof model for the weakly ($\mu = 0.05$ ($\triangle$)) and strongly ($\mu = 0.7$ ($\diamond$)) nonlinear case. In both cases small superharmonic resonance peaks appear near $f_e = 16.66 \approx f_2/5$ and $f_e = 25.28 \approx f_3/9$ in the first harmonic resonance peak. Obviously these resonances, also called *internal resonances* (Chen et al. [1989]), are lacking in the single dof model. The weakly nonlinear case is calculated in three ways ($n_\tau = 320$): using an $O(\triangle\tau^2)$ scheme (solid line with $\triangle$ symbols, 1402 s. CPU-time, 450 pf-steps), the deferred correction method (dotted line, 1502 s. CPU-time, 450 pf-steps) and the $O(\triangle\tau^4)$ scheme (solid line without symbols, 2064 s. CPU-time). Differences between the three lines are not visible in figure 7.5, with the exception of regions, where cyclic fold bifurcations occur. The upper left inset shows a detail of the internal resonance near $f_e = 16.66 \approx f_2/5$ and the lower right inset shows a further detail. The cyclic fold bifurcation points are slightly shifted to lower frequencies if the $O(\triangle\tau^4)$ branch is compared with the $O(\triangle\tau^2)$ branch. Because the deferred correction method only corrects the periodic solution for a constant value of the design variable f_e, erroneous corrections can be expected near cyclic fold bifurcation points.

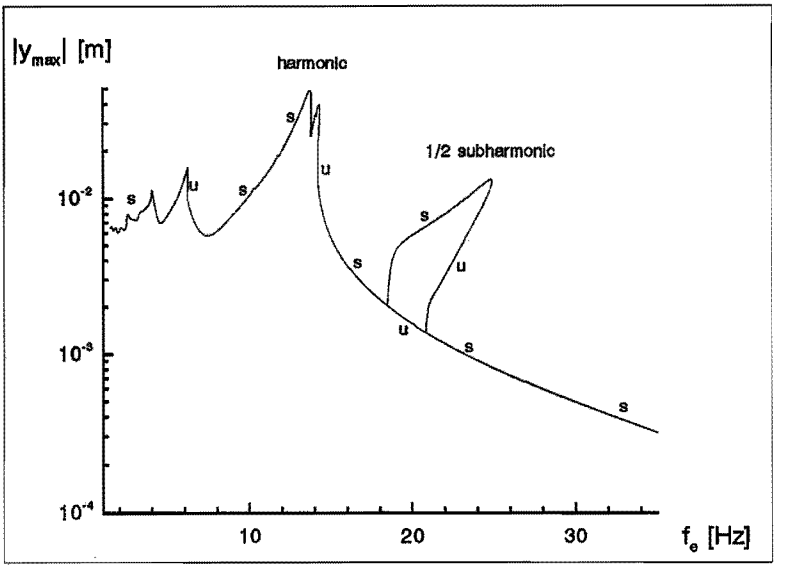

Figure 7.6: Amplitude-frequency plot of four dof system with stiffening pressure spring

7.3 Support by a one-sided stiffening spring

This system is investigated using the four dof model for the strongly nonlinear case: $\mu = 0$, $\mu_p = 7$, $\alpha = 0$. Figure 7.6 shows the amplitude-frequency plot for $\xi = 0.05$. The branch with harmonic solutions ($n_\tau = 400$) shows two harmonic resonance peaks at $f_e = 13.72$ Hz and $f_e = 14.29$ Hz. Two flip bifurcation points are found at $f_e = 18.43$ Hz and $f_e = 20.84$ Hz, which frequencies form the boundaries of a branch with 1/2 subharmonic solutions. The flip bifurcation point at $f_e = 18.43$ Hz, from which a stable 1/2 subharmonic branch sets off ($n_\tau = 800$), is supercritical. Conversely, the flip bifurcation point at $f_e = 20.84$ Hz, from which a branch with unstable 1/2 subharmonic solutions departs, is subcritical. The stability of the branch with 1/2 subharmonic solutions changes at the cyclic fold bifurcation point at $f_e = 24.90$ Hz. The damping level ($b = 5.8$ Ns/m) in the system is too high to meet subharmonic solutions of order 1/3. Figure 7.7 shows the amplitude-damping plot of branches of 1/3 subharmonic solutions for several excitation frequencies. For high values of the damping, the branches cease to exist via cyclic fold bifurcation points. For each excitation frequency holds that the high amplitude branch is stable and the low amplitude branch is unstable.

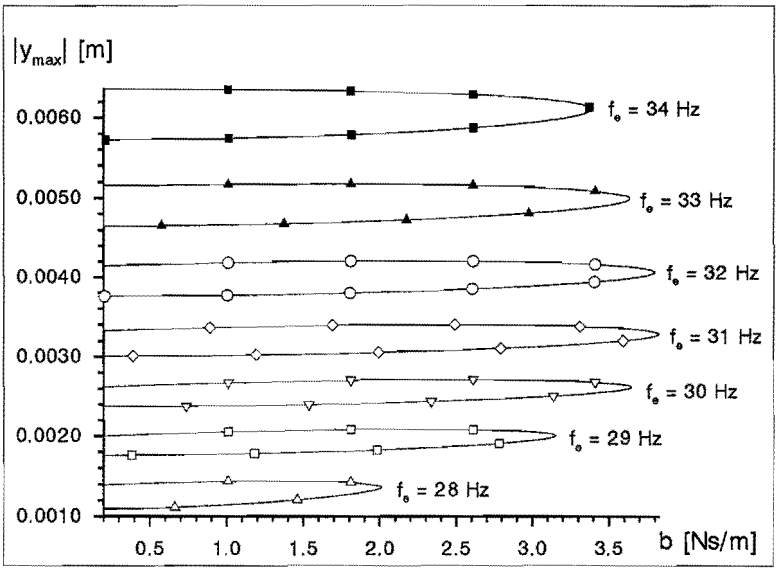

Figure 7.7: Amplitude-damping plot of 1/3 subharmonic solutions for several values of the excitation frequency f_e

7.4 Support by a one-sided linear spring

7.4.1 Single dof model: moderately nonlinear

In this bilinear system ($\mu = 0$, $\mu_p = 0$) harmonic resonance occurs near the bilinear eigenfrequency f_b of the unforced, undamped system (Shaw and Holmes [1983]):

$$f_b = \frac{2\sqrt{1+\alpha}}{1+\sqrt{1+\alpha}} f_1$$

In contrast to the Duffing system the amplitude of the external load F_{dy} is nothing but a scaling factor and therefore does not appear in the dimensionless quantities involved. Figure 7.8 shows for two values of damping ($\xi = 0.01$ and $\xi = 0.1$) the amplitude-frequency plot of the bilinear system for the case that the stiffness of the supporting spring is equal to the contribution of the first free-interface eigenmode to the stiffness of the beam: $\alpha = 1$ ($f_b = 10.49$ Hz). For $\xi = 0.01$ two branches of 1/2 subharmonic solutions are found in the frequency intervals 6.66-7.12 Hz and 17.97-23.58 Hz, which bifurcate from the harmonic branch via flip bifurcations at the boundaries of the intervals. On the 1/2 subharmonic branch between the second superharmonic resonance and the harmonic resonance peak also two cyclic fold bifurcation points are found. Because the nonlinearity is not point-symmetric, the second superharmonic resonance peak now does not bifurcate from the low amplitude harmonic branch via a pitchfork bifurcation. A small closed branch with

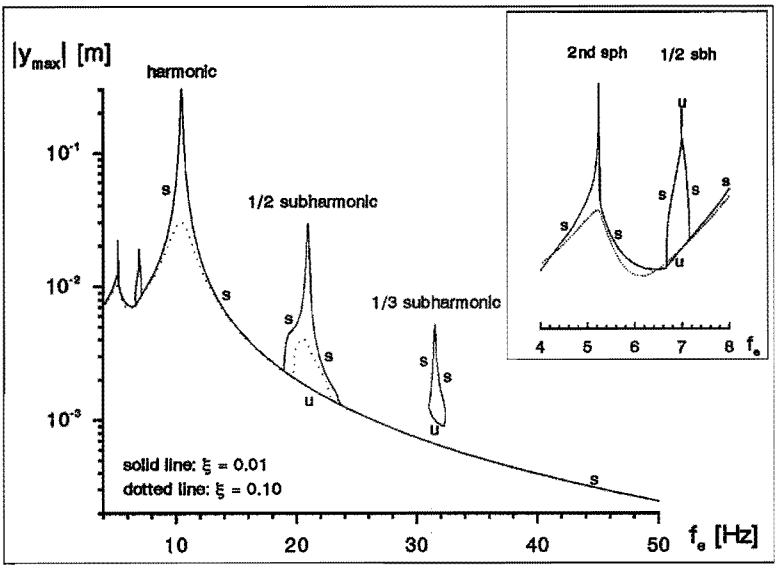

Figure 7.8: Amplitude-frequency plot of bilinear single dof system ($\alpha = 1$)

1/3 subharmonic solutions is found. The frequency interval, in which 1/3 subharmonic solutions are found, is bounded by two cyclic fold bifurcation points at $f_e = 31.01$ Hz and $f_e = 32.37$ Hz.

For $\xi = 0.1$ the height of the resonance peaks diminishes. The low frequency interval with 1/2 subharmonic solutions has disappeared. The high frequency interval with 1/2 subharmonic solutions becomes smaller. A branch with 1/3 subharmonic solutions was not found.

In table 7.1 flip bifurcation values ξ_{bif}^{F}, obtained with the numerical methods of chapters 3 and 4 ($n_\tau = 600$, $0(\Delta\tau^2)$ scheme), are compared for four values of α with bifurcation values ξ_{bif}^{SH} presented by Shaw and Holmes [1983] , who used analytical integration for the two linear regions $y \geqslant 0$ and $y < 0$ for the determination of periodic solutions. For values of the damping above the bifurcation value no 1/2 subharmonic solutions exist. There exists a good agreement between the results.

7.4.2 Single dof model: strongly nonlinear

Figure 7.9 shows for two values of damping ($\xi = 0.01$ and $\xi = 0.1$) the amplitude-frequency plot for the case that $\alpha = 6$ ($f_b = 13.00$ Hz). Compared to the case $\alpha = 1$, the frequency intervals, in which subharmonic solutions occur, widen. For $\xi = 0.01$ the boundaries of the largest frequency interval with 1/2 subharmonic solutions are formed by the flip bifurcation values $f_e = 20.64$ Hz and $f_e = 38.50$ Hz; the boundaries of the frequency interval with 1/3 subharmonic solutions are formed by the cyclic fold bifurcation values $f_e = 36.06$ Hz and

α [-]	$f_e = 2f_b$ [Hz]	ξ_{bif}^{F} [-]	ξ_{bif}^{SH} [-]
0.44	19.55	0.063	0.066 ± 0.002
0.96	20.90	0.129	0.128 ± 0.002
1.56	22.05	0.193	0.190 ± 0.002
2.24	23.04	0.255	0.250 ± 0.002

Table 7.1: Comparison between flip bifurcation values ξ_{bif}^{F} found with present method and values ξ_{bif}^{SH} found by Shaw and Holmes [SH83]

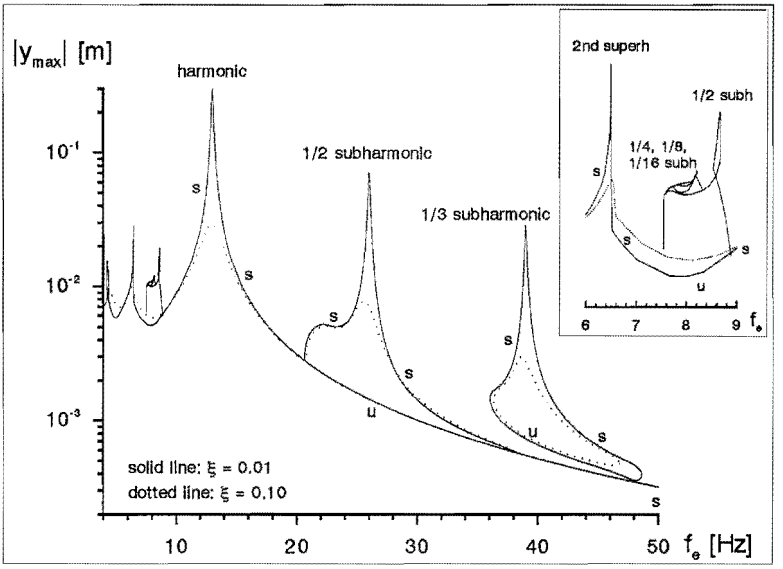

Figure 7.9: Amplitude-frequency plot of bilinear single dof system ($\alpha = 6$)

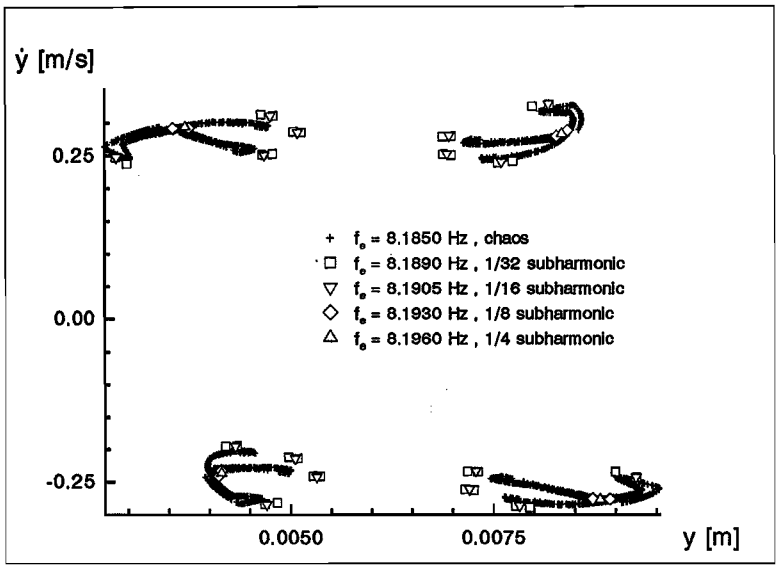

Figure 7.10: Poincaré section: period doublings leading to chaos

f_e = 48.65 Hz. The sub- and superharmonic resonance peaks become higher, while the height of the harmonic resonance peak approximately remains the same. Because of the higher value of the eigenfrequency of the bilinear system, also sub- and superharmonic resonance peaks occur at higher excitation frequencies: the third superharmonic resonance peak near 4.35 Hz has entered the investigated frequency range ($\xi = 0.01$). Investigation of the stability of the branch with 1/2 subharmonic solutions for the case $\xi = 0.01$ in the frequency interval $f_e = 7.55 - 8.69$ Hz learns that the branch contains quite a number of stable and unstable regions: flip bifurcation points as well as cyclic fold bifurcation points are met. In small frequency intervals also 1/4, 1/8 (n_τ = 800) and 1/16 (n_τ = 1600) subharmonic branches were calculated, see the inset of figure 7.9.

For f_e = 8.185 Hz no stable periodic solution could be found. Figure 7.10 shows the Poincaré sections of steady-state attractors calculated for this excitation frequency and 4 excitation frequencies, which were a fraction higher. These attractors were calculated by numerical integration using the Runge-Kutta-Merson method requiring a precision of 10 digits. All initial conditions were set to zero at t = 0. All solutions were recorded only after 6000 excitation periods, to ensure that the transient had damped out. Each solution contains 4000 points. If f_e is decreased from 8.1960 Hz to 8.1890 Hz a sequence of period doublings is observed from an 1/4 subharmonic solution, via an 1/8 and 1/16 subharmonic to a 1/32 subharmonic solution. For f_e = 8.1850 Hz a chaotic solution was calculated. The Lyapunov exponents ($\lambda_1 = 0.842$, $\lambda_2 = -2.47$) again satisfy equation (6.19) (m = 1.0358 kg, b = 1.1661 Ns/m). The results obtained strongly suggest that the transition to the chaotic motion is an infinite cascade of period doublings leading to a solution with an

i	f_i reduced [Hz]	f_i original [Hz]
1	22.809	22.809
2	83.723	83.723
3	225.07	225.07
4	538.98	439.56

Table 7.2: Eigenfrequencies of reduced and original linear model with linear spring attached ($\alpha = 6$)

$\alpha = 6 \rightarrow$ $\alpha = 0 \downarrow$	mode 1	mode 2	mode 3	mode 4
mode 1	0.824	0.030	0.003	0.001
mode 2	0.138	0.945	0.007	0.001
mode 3	0.027	0.018	0.986	0.002
mode 4	0.011	0.007	0.005	0.996

Table 7.3: Contributions of eigenmodes of system without spring ($\alpha = 0$) to eigenmodes of system with spring attached ($\alpha = 6$)

infinite period (Feigenbaum [1983]).

If the damping is increased to $\xi = 0.1$ the subharmonic and chaotic solutions in the frequency interval 7.55-8.69 Hz disappear and the harmonic solution becomes stable.

In agreement with the theoretical results of Shaw and Holmes [1983] and Natsiavas [1990] no Neimark bifurcation points were observed in the bilinear single dof system.

7.4.3 Four dof model: strongly nonlinear

If the supporting spring ($\alpha = 6$) is attached to the beam, the bilinear system becomes linear. In table 7.2 the eigenfrequencies of the reduced linear four dof model are compared with the four lowest eigenfrequencies of the original model, both models with the supporting spring attached ($\alpha = 6$). It is important to realize that the reduced model is derived for $\alpha = 0$ (for the eigenfrequencies see table 2.6 on page 41) and coupled with the supporting spring afterwards. The first three eigenfrequencies agree very well, so in the bilinear case of the one-sided spring the first three eigenfrequencies and eigenmodes are very accurate for $y \geqslant 0$ as well as $y < 0$. The contributions of the four eigenmodes of the reduced system for $\alpha = 0$ to the four eigenmodes of the reduced system with the spring attached ($\alpha = 6$) are given in table 7.3. The contribution of an $\alpha = 0$ eigenmode is expressed in terms of the quotient of the Euclidian norm of the contribution of this eigenmode and the sum of the Euclidian norms of the contributions of the four $\alpha = 0$ eigenmodes.

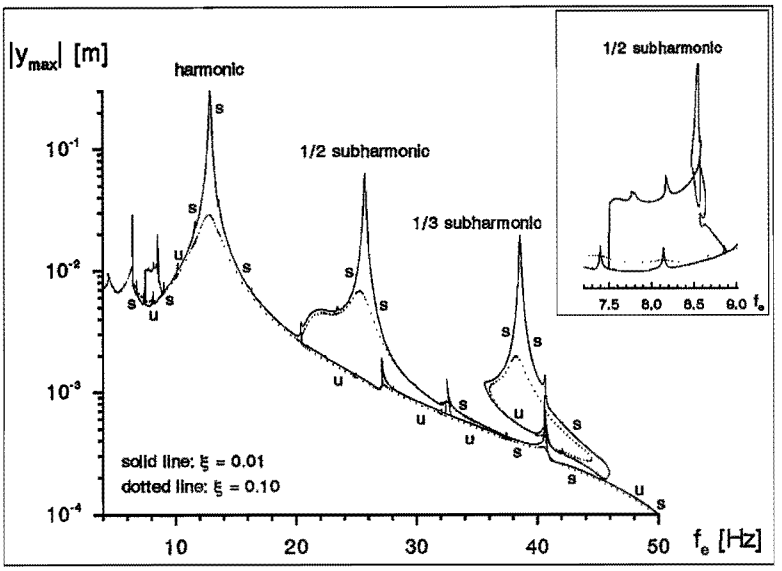

Figure 7.11: Amplitude-frequency plot of bilinear four dof system ($\alpha = 6$)

Figure 7.11 shows the amplitude-frequency plot for two values of the damping ($\xi = 0.01$ and $\xi = 0.1$) for the bilinear system ($\alpha = 6$). The stability indications (s(table) and u(nstable)) refer to the case $\xi = 0.01$. Globally it is very similar to figure 7.9. A closer look, however, reveals a number of differences between the two figures.

Firstly, a large number of superharmonic resonance peaks with moderate to small amplitudes are found in figure 7.11, which are caused by the higher bilinear eigenfrequencies. The superharmonic resonance peaks near 1/2 f_{b2}, 1/3 f_{b2} and 1/4 f_{b2} ($f_{b2} \approx 82$ Hz) can be clearly recognized.

In contrast to the single dof model no cascade of period doublings is found near $f_e = 8.19$ Hz. Investigation of the Floquet multipliers learns, that the branch with 1/2 subharmonic solutions is stable in the interval $f_e = 8.165 - 8.332$ Hz, where a small superharmonic resonance peak occurs on the branch with 1/2 subharmonics (see inset figure 7.11), which is missing in the one dof model (see inset figure 7.9). Numerical integration calculations for the excitation frequencies shown in figure 7.10 confirm the stability of the 1/2 subharmonic solutions in the interval. The branch with 1/2 subharmonics shown in the inset of figure 7.11 exposes many small intervals with stable and unstable solutions and shows not only cyclic fold and flip bifurcation points, but also Neimark bifurcation points. A more detailed investigation of this branch is out of the scope of this thesis and is therefore omitted.

Figure 7.12 shows, that near $f_e = 32.5$ Hz there is a small frequency interval, where no stable periodic solutions could be found using the time discretization method in combination with the path following method for $\xi = 0.01$. In this interval the branch with 1/2 subharmonic solutions is interrupted in contrast to the single dof model. For higher values

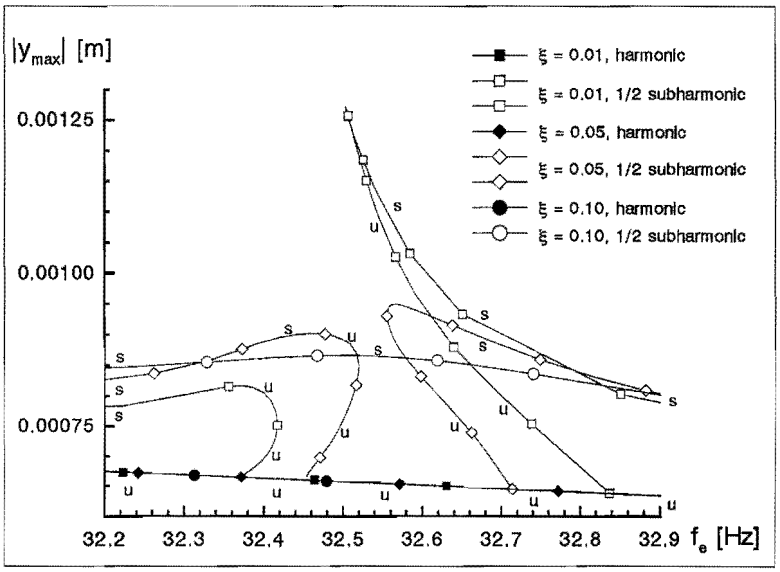

Figure 7.12: No stable periodic solutions near $f_e = 32.5$ Hz for low values of the damping

of the damping ($\xi = 0.05$) the interval decreases and eventually disappears ($\xi = 0.1$). In the latter case the 1/2 subharmonic branch becomes stable. For the case $\xi = 0.05$ numerical integration (Adams' method, accuracy of 9 significant digits, $t_t = 6000T_e$, initial conditions zero at $t = 0$) is applied to investigate the character of the stable steady-state solutions in this frequency range. Firstly, in figure 7.13 the phase-portrait of the stable 1/2 subharmonic for $f_e = 32.6$ Hz (just outside the frequency interval) calculated with the time discretization method ($n_\tau = 800$, $O(\triangle\tau^2)$, black dots) is verified with the numerical integration (solid line) method. Figure 7.14 shows the Poincaré sections ($\phi_P = \phi_e = -\pi/2$) of steady-states calculated with numerical integration for four different values of f_e (4000 points for each calculation). For $f_e = 32.6$ Hz, $f_e = 32.58$ Hz and $f_e = 32.56$ Hz the Poincaré section shows two points, i.e. two groups of 2000 coinciding points, indicating a 1/2 subharmonic solution. If the excitation frequency is further reduced, the frequency interval of interest is entered. This results in a break-down of the stable 1/2 subharmonic solution. However, for $f_e = 32.552$ Hz, the largest part of the 4000 points still cluster around two points in the Poincaré section. So, although the steady-state is not periodic anymore, one could say that the ghost of the 1/2 subharmonic solution is still abroad. Figures 7.15 and 7.16 show the time histories of y for $f_e = 32.552$ Hz and $f_e = 32.55$ Hz respectively in the time interval $t = 6000T_e - 6500T_e$. In a large part of this time interval the solution seems to be a 1/2 subharmonic, see insets 1 (8 excitation periods) of figure 7.15 and 7.16. Then, suddenly, there appears a burst in the signal for a short period of time, see insets 2 (8 excitation periods), after which the signal recovers again. This behaviour is called *intermittency* (Pomeau and Manneville [1980]). The Poincaré section in figure 7.14 for

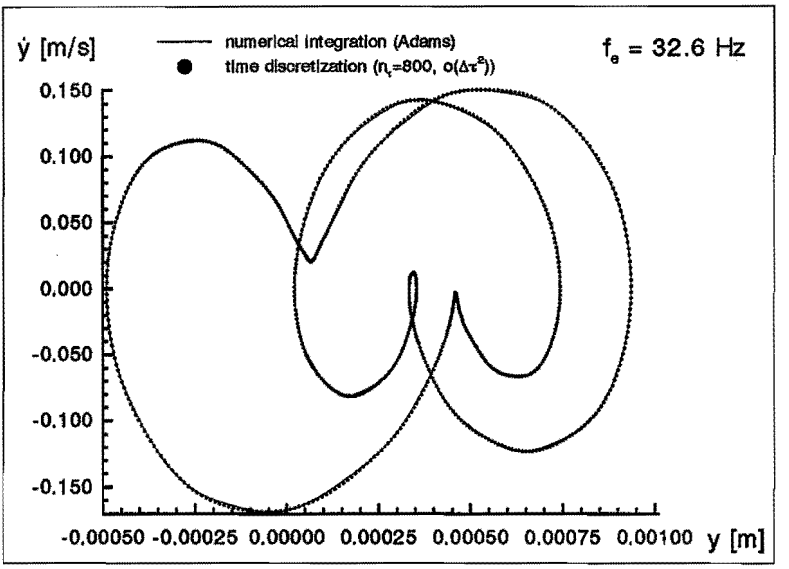

Figure 7.13: Comparison between stable 1/2 subharmonic solutions obtained with time discretization and numerical integration in the phase-plane

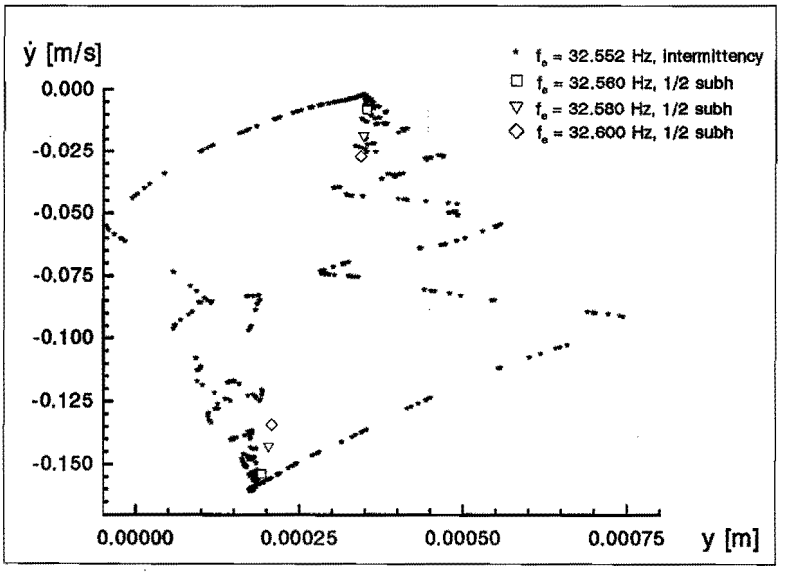

Figure 7.14: Poincaré sections for four different values of f_e

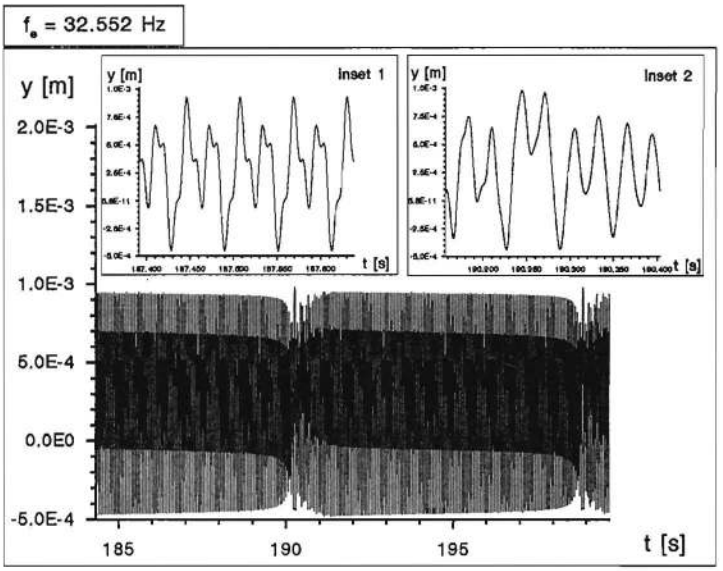

Figure 7.15: Intermittency

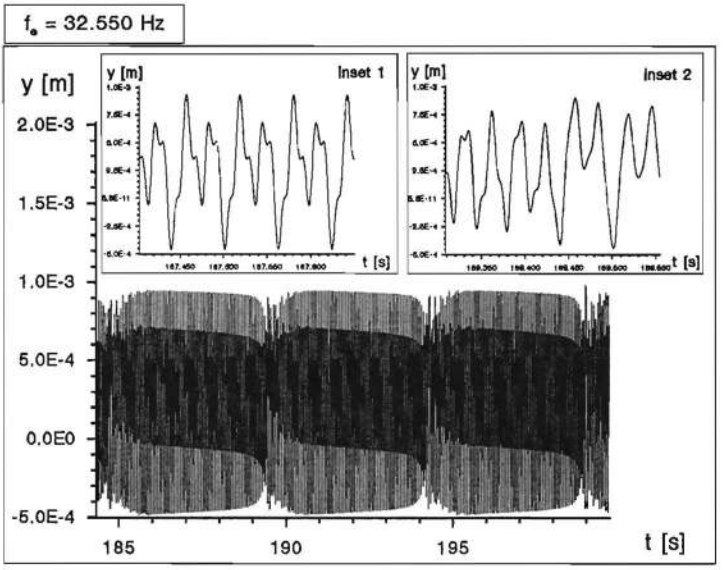

Figure 7.16: Intermittency

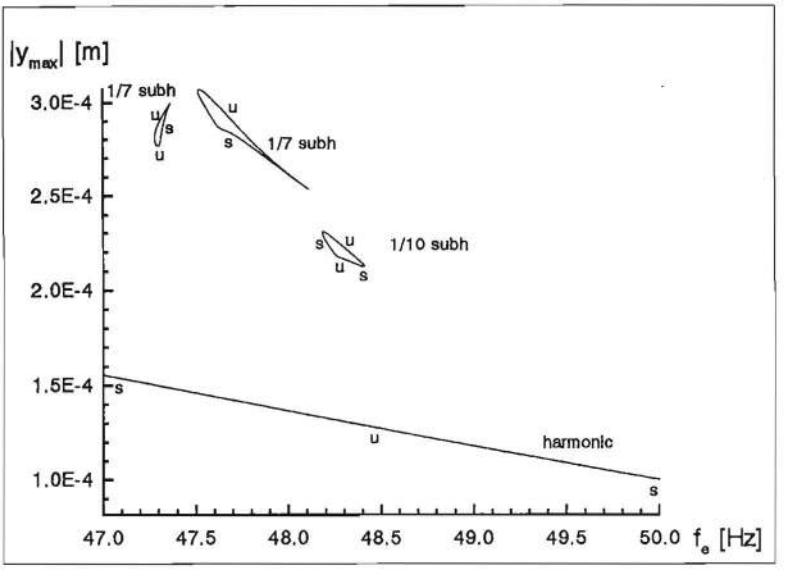

Figure 7.17: Amplitude-frequency plot near the Neimark bifurcation points

$f_e = 32.552$ Hz shows a weakly chaotic attractor (weakly because the time signal still shows much regularity). As the chaotic region is entered further, the time intervals between two subsequent bursts become shorter, compare figures 7.15 and 7.16. Eventually the intervals with almost periodic behaviour will disappear. According to Pomeau and Manneville (1980) (but see also Schuster [1989]) there exist three mechanisms, by which intermittency can be introduced: via a cyclic fold bifurcation, a flip bifurcation or a Neimark bifurcation. In this case the right branch with 1/2 subharmonic solutions becomes unstable via a cyclic fold bifurcation (turning point) at $f_e \approx 32.555$ Hz. The left branch with 1/2 subharmonic solutions already becomes unstable at $f_e \approx 32.48$ Hz via a Neimark bifurcation before the turning point occurs at $f_e \approx 32.52$ Hz.

For $f_e = 50$ Hz there is a large relative difference between the amplitudes of the single dof model (0.0003 m, figure 7.9) and the four dof model (0.0001 m, figure 7.11). This is caused by the anti-resonance near $f_e = 56$ Hz in the four-dof model, which of course does not exist in the single dof model. Before the anti-resonance the branch with harmonic periodic solutions becomes unstable via Neimark bifurcations in the interval 47.33-49.53 Hz, see figure 7.17 ($\xi = 0.05$). In this interval a *quasi-periodic→locked→chaotic sequence* (Newhouse et al. [1978] , Thompson and Stewart [1986] , Schuster [1989]) is observed, which is described below. Again numerical integration is used to investigate the steady-state behaviour (Adams' method, accuracy of 9 significant digits, $t_t = 6000T_e$, initial conditions zero at $t = 0$). The upper picture of figure 7.18 and figure 7.19 show the time history (50 T_e) and the Poincaré section respectively ($\phi_P = \phi_e = -\pi/2$) of the stable, harmonic solution at $f_e = 49.58$ Hz (all Poincaré sections shown in figures 7.19, 7.20 and

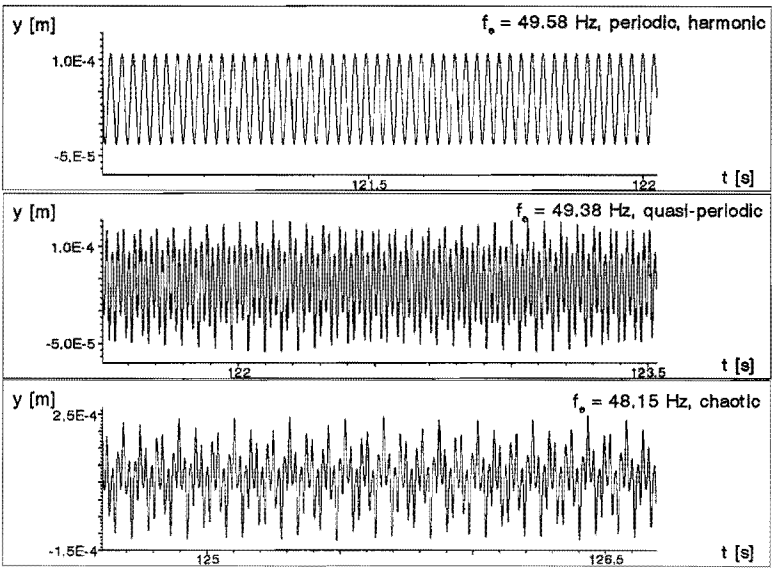

Figure 7.18: Periodic, quasi-periodic and chaotic time histories

7.21 contain 4000 points per attractor). If the excitation frequency is reduced, the solution becomes quasi-periodic. The Poincaré sections (figure 7.19) show closed curves (transections of a 2D torus), which amplitudes grow for decreasing f_e. The middle picture of figure 7.18 shows the time history (100 T_e) of the quasi-periodic solution at $f_e = 49.38$ Hz. Shaw et al. [1989] reported quasi-periodic motion in a two dof system with a cubic stiffening spring for excitation frequencies $f_e \approx (f_1 + f_2)/2$ (f_1 and f_2 being the eigenfrequencies of the system without the nonlinear spring). In fact, this is also the frequency range under consideration here. A further reduction of the excitation frequency to $f_e = 49.05$ Hz results in a subharmonic solution of order 1/22, see figure 7.20. This phenomenon, in which the ratio of the forced frequency and the free frequency becomes rational, is called frequency-locking or mode-locking. For $f_e = 48.70$ Hz the attractor is quasi-periodic again, but starts to develop wrinkles, which are most clearly seen in the lower left part of figure 7.20. Wrinkles arise in the 2D torus if the onset of chaos is approached (Thompson and Stewart [1986]). For $f_e = 48.55$ Hz the attractor is weakly chaotic. Figure 7.21 shows that a further reduction of the excitation frequency again results in a locked state (subharmonic of order 1/10 for $f_e = 48.40$ Hz) and finally in a truely chaotic attractor for $f_e = 48.15$ Hz. Using the 1/10 subharmonic solution obtained with the numerical integration method as starting solution, the path following method is applied to follow a branch of subharmonic solutions of order 1/10. The result, see figure 7.17, is a very small closed branch in the frequency range 48.18-48.41 Hz, which boundaries are formed by cyclic fold bifurcation points. The high amplitude branch is unstable and the low amplitude branch is stable in the ranges 48.18-48.20 Hz and 48.39-48.41 Hz and unstable in the range 48.20-48.39 Hz via

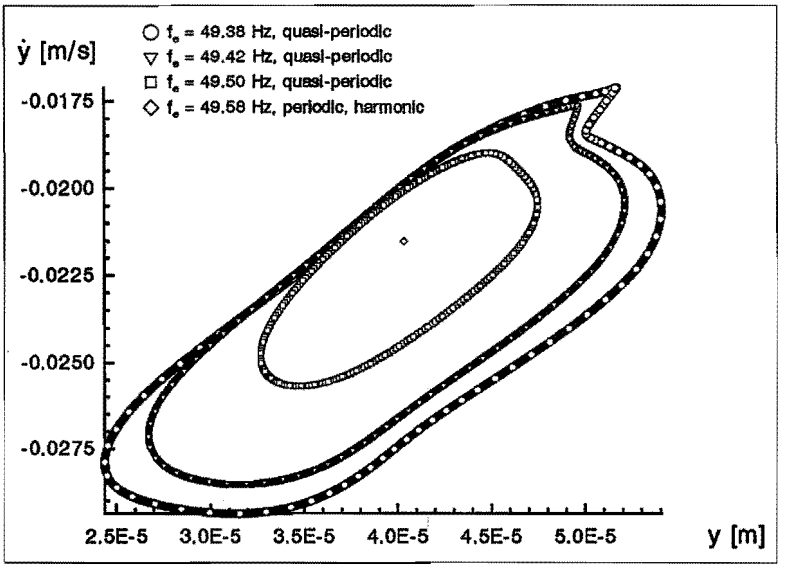

Figure 7.19: Poincaré sections showing a periodic and quasi-periodic solutions on both sides of the right Neimark bifurcation point

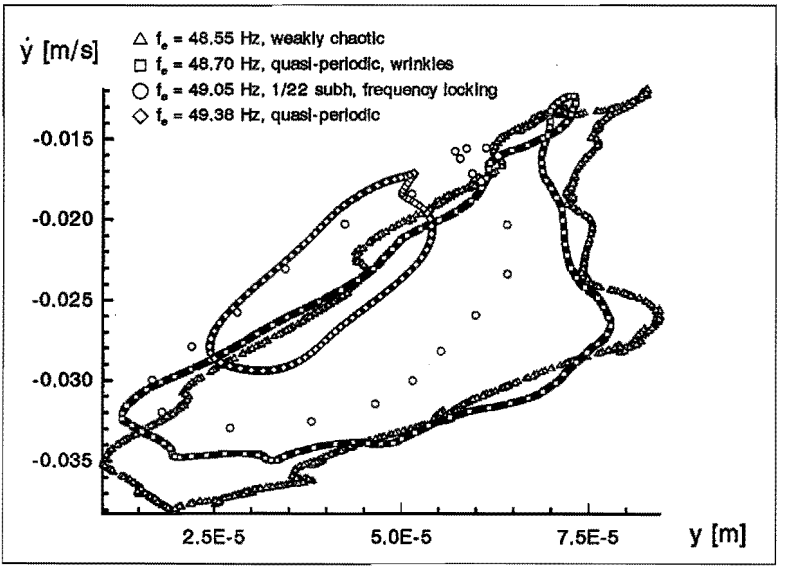

Figure 7.20: Poincaré sections showing frequency locking and the break-down of the quasi-periodic solutions

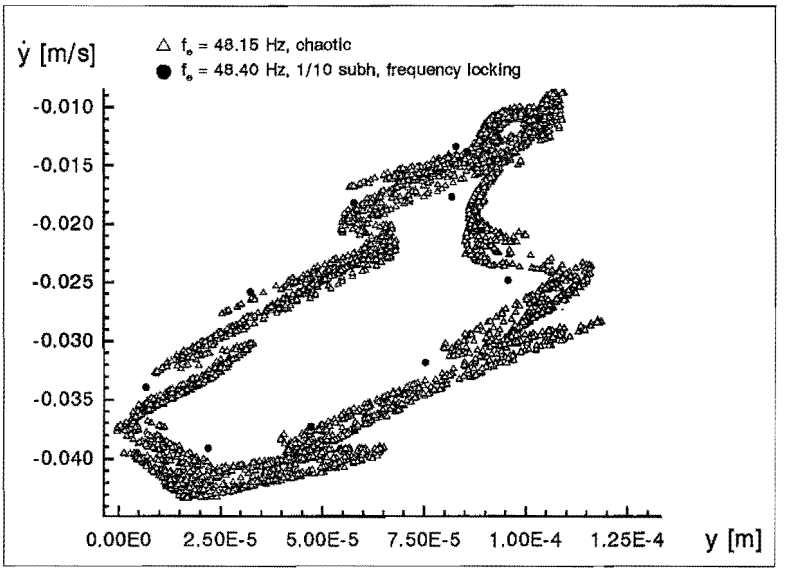

Figure 7.21: Poincaré sections showing frequency-locking and chaos

flip bifurcations. The lower picture of figure 7.18 shows the time history (100 T_e) of the chaotic attractor for $f_e = 48.15$ Hz. Figure 7.22 shows the time history of the 8 Lyapunov exponents of this attractor, which are calculated using the Runge-Kutta-Merson method (accuracy of 9 significant digits, $t_t = 6000T_e$, initial conditions zero at $t = 0$) in the interval $6000T_e$-$10000T_e$. At $t = 10000T_e$ all Lyapunov exponents appear to be converged. The Poincaré section of the chaotic attractor at $f_e = 48.15$ Hz, shown in figure 7.21, was calculated using the Adams' method. The Poincaré section was verified by the Runge-Kutta-Merson method. Using equations (6.25) and (6.26) the Lyapunov dimension of the Poincaré section this attractor can be estimated. This dimension increased by 1 gives an estimate of the Lyapunov dimension of the attractor: $D_\lambda \approx 3.15$. This means that this attractor (rather an approximation of this attractor) can not be found in the one-dof model of the previous subsection on principle, because the augmented state space of this model is only threedimensional. It costed 80000 (!) s. of CPU-time to calculate the attractor and all the Lyapunov exponents simultaneously, whereas the calculation of the attractor alone costed only 1600 s. of CPU-time. Figure 7.23 shows the frequency spectra of the harmonic solution at $f_e = 49.58$ Hz, the quasi-periodic solution at $f_e = 49.38$ Hz and the chaotic solution at $f_e = 48.15$ Hz. In the case of the harmonic solution only peaks are found at 0 Hz, indicating the off-set in the signal, at the excitation frequency f_e and multiples of it. The spectrum of the quasi-periodic solution shows peaks at combinations of the forced frequency f_e and the free frequency f_f. The frequency spectrum of the chaotic signal is characterized by a broad-band noise. For $f_e = 47.95$ Hz, $f_e = 47.80$ Hz and $f_e = 47.30$ Hz subharmonics of order 1/7 are calculated (frequency locking). Again using one of these 1/7

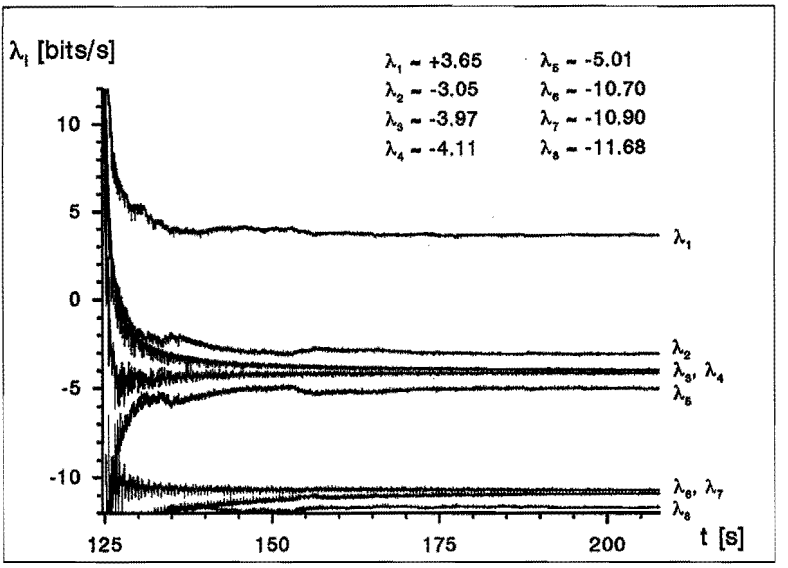

Figure 7.22: Converging Lyapunov exponents of the chaotic attractor at $f_e = 48.15$ Hz

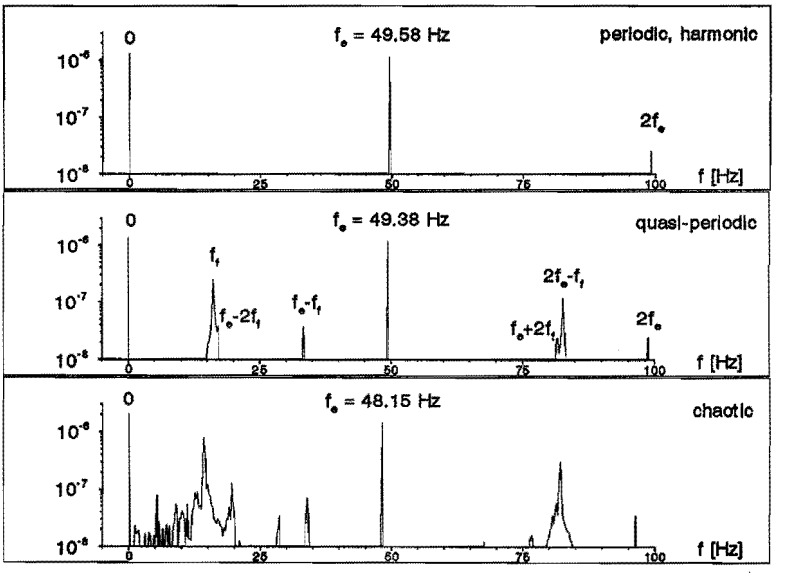

Figure 7.23: Frequency spectra of a periodic, a quasi-periodic and a chaotic attractor

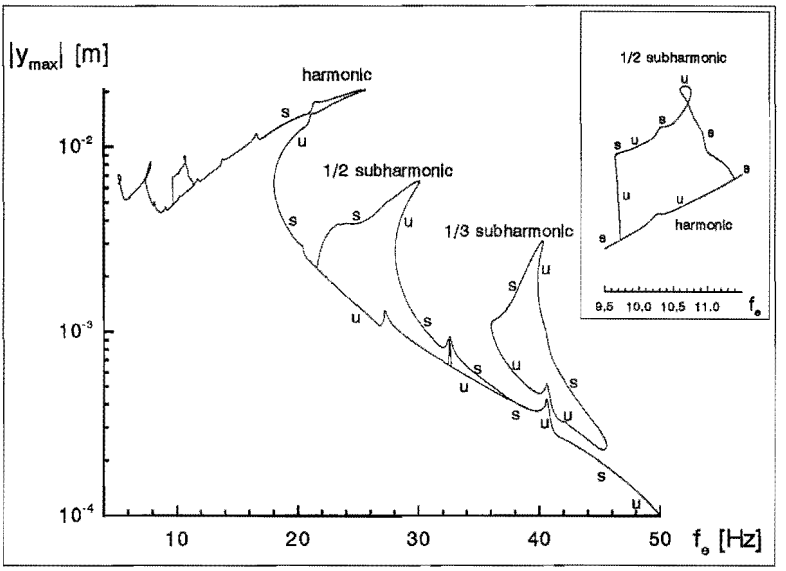

Figure 7.24: Amplitude-frequency plot of a beam supported by a stiffening and a one-sided linear spring

subharmonic solutions as starting solution, the path following method is applied to follow subharmonic solutions of order 1/7 for varying excitation frequency. There appear to be two closed branches of subharmonic solutions of order 1/7, see figure 7.17. In the interval 47.36-47.51 Hz, lying inbetween, a chaotic attractor is found for $f_e = 47.46$ Hz.

The numbers of time discretization points n_τ used in this subsection to calculate the several branches with periodic solutions are: 400 for the harmonic solutions, 800 for the 1/2 subharmonic solutions, 750 for the 1/3 subharmonic solutions, 1050 for the 1/7 subharmonic solutions and 1500 for the 1/10 subharmonic solutions.

7.5 Support by a stiffening and a one-sided linear spring

Only the strongly nonlinear ($\mu = 0.7$, $\mu_p = 0$, $\alpha = 6$) case with moderate damping ($\xi = 0.05$) is considered. Figure 7.24 shows the amplitude-frequency plot for the four dof model (solid curves) and the eight dof model (dotted curve). For the latter model only the branch with harmonic solutions is calculated in the frequency range 11.3-50.0 Hz was calculated. The difference between the results of the four dof and the eight dof is neglectable. The CPU-times, however, differ very much: 6319 s. for the calculation of the solutions and 2454 s. for the stability analysis for the four dof model (1197 pf-steps), against 41898 s. for the calculation of the solutions and 17362 s for the stability

analysis for the eight dof model (1500 pf-steps) for the same frequency range. Of course, all calculations were carried out under the same path following conditions (most important parameters: $\beta_1 = \beta_2 = 5°$, $\sigma_{max} = 0.25$). The conclusion is that the four dof model may be preferred in this frequency range. For high amplitude responses the effect of the cubic stiffening spring is clearly visible: the first harmonic resonance peak and both the subharmonic resonance peaks bend over to the right. Cyclic fold bifurcation points are found at $f_e \approx 18.04$ Hz and $f_e \approx 25.60$ Hz (harmonic resonance peak), $f_e \approx 30.09$ Hz and $f_e \approx 28.08$ Hz (1/2 subharmonic resonance peak) and $f_e \approx 39.86$ Hz and $f_e \approx 40.34$ Hz (1/3 subharmonic resonance peak). For low amplitude responses the presence of the cubic stiffening spring is, as could be expected, hardly noticeable. The frequency intervals, which showed intermittency and a quasi-periodic→locked→chaotic sequence in subsection 7.4.3, still exist (Schouten [1991]). The branch with 1/2 subharmonic solutions before the first harmonic resonance peak has been shifted to a higher frequency interval (compare the insets of figures 7.11 and 7.24). The left flip bifurcation point shown in the inset of figure 7.24 at $f_e = 9.73$ Hz is subcritical, whereas the right flip bifurcation point at $f_e = 11.35$ Hz is supercritical.

The numbers of time discretization points n_τ used in this section to calculate the branches with periodic solutions are: 400 for the harmonic solutions, 800 for the 1/2 subharmonic solutions and 750 for the 1/3 subharmonic solutions.

Chapter 8

Conclusions and recommendations

In this last chapter, some major conclusions are drawn and some recommendations for further research are given.

For linear systems the component mode synthesis technique based on free-interface eigenmodes and residual flexibility modes gives accurate results at system level below the cut-off frequency, used to reduce the number of dof of the components. For systems, consisting of linear components and local nonlinearities, this is not true in general. The accuracy of the solution of a reduced nonlinear system for a certain excitation frequency can be checked, however, by examining the frequency spectrum of the external loads minus the internal loads, caused by the local nonlinearities and examining the influence of additional modes on this spectrum. By using the cms method based on free-interface eigenmodes and residual flexibility modes, reduced linear component models can (almost) totally be obtained by experiments, at least in principle.

By application of the time discretization method in combination with the path following method branches of periodic solutions can be followed for varying design variable. By combining these methods with the reduction method the steady-state behaviour of complex dynamic systems with local nonlinearities can be analyzed very efficiently. By means of a deferred correction technique an $O(\triangle\tau^2)$ solution can be improved to an $O(\triangle\tau^4)$ solution; moreover the global error of the $O(\triangle\tau^2)$ solution can be estimated. In the example given in chapter 3, 50% more CPU-time would be needed to obtain the same mean global error by applying a direct $O(\triangle\tau^4)$ discretization scheme. However, the deferred correction technique can give erroneous corrections in the neighbourhood of cyclic fold bifurcation points. The local stability of the periodic solutions can be investigated by means of the Floquet multipliers. Moreover, for marginally stable periodic solutions the Floquet multipliers indicate the type of the bifurcation point, which may be a cyclic fold, a flip or a Neimark bifurcation point. CPU-time consuming numerical integration techniques for calculating the steady-state behaviour have to be applied only in those regions of the design variable, where no stable periodic solutions can be found through time discretization. The character of these attractors, which may be periodic, quasi-periodic or chaotic, can be determined by calculating the Lyapunov exponents. These Lyapunov exponents can be used to calculate the Lyapunov dimension of an attractor. The dimension of an attractor determines

the minimal dimension of the augmented state space, which is neccessary to generally observe this attractor. In case of multi-dof models the calculation of all Lyapunov exponents becomes very expensive, whereas only a number of the highest Lyapunov exponents are needed to calculate the Lyapunov dimension of the attractor. Therefore, if one has an idea about the dimension of a chaotic attractor, one should use this information by calculating only the Lyapunov exponents of interest.

In contrast to numerical integration techniques, the time discretization technique gives no information about the domains of attraction of steady-state attractors. If information about domains of attraction is required, the cell-to-cell mapping technique (Hsu [1980] , Hsu and Guttalu [1980] , Hsu [1981] and Tongue [1989]), which is based on numerical integration, can be used. However, direct numerical integration is different from the cell-to-cell mapping technique as it combines the information obtained with the present numerical integration run with the information obtained from preceding numerical integration calculations (with different initial conditions). The cell-to-cell mapping technique is only capable of finding (sub)harmonic solutions of order 1/n with n greater than 1 and lower than or equal to the total number of cells. Quasi-periodic and chaotic attractors will in general be identified with subharmonic solutions of very low order. The cell-to-cell mapping technique is mostly applied to systems with an augmented state-space of dimension three. Naturally, computational costs quickly rise if the dimension of the augmented state space increases. The results obtained with the cell-to-cell mapping technique, which can be found in the literature, are promising and further investigation of the possibilities of the technique is recommended.

The application of the various numerical tools to the beam system with nonlinear support leads to the following major conclusions. Super- and subharmonic resonances can be suppressed by addition of damping. If the power of the nonlinearity is even (uneven), the damping will destroy the n-th superharmonic and the 1/n subharmonic resonances, where n is uneven (even), before it destroys the m-th superharmonic and the 1/m subharmonic resonances, where m is even (uneven). If damping is increased, subharmonic solutions persist longer for strongly nonlinear systems than for weakly nonlinear systems. Three different routes to chaos can be found in the beam system with a supporting one-sided linear spring: the period doubling route, the intermittency route and the quasi-periodic→locked→chaotic route. The Lyapunov dimension of a chaotic solution arising via the latter route pointed out that (an approximation of) this chaotic attractor cannot be found in a single dof model. Very probably there will be much more (small) frequency intervals, in which frequency locking occurs, in the quasi-periodic→locked→chaotic route to chaos than the intervals detected so far. A detailed investigation of all these intervals could be very expensive.

The beam system, which was investigated in the previous chapter, consisted of one linear component only. The approach of a system, consisting of several linear components with local nonlinearities is not substantially different.

The steady-state behaviour of the beam system presented in chapter 7 has not yet been verified by experiments. Especially to show the relevancy of chaos theory to engineering practice, it is important that this will be done in the near future. The simple geometry of the beam system gives the possibility to concentrate specifically on chaos phenomena.

Because the exitation frequency ranges, where chaotic attractors occur, are rather small in the beam systems investigated, it is advisable to define such an experiment for values of the design variables, for which the frequency regions with chaotic attractors are larger. At present there is not much experience with the experimental determination of Lyapunov exponents, although Wolf et al. [1985] presented an algorithm for the experimental determination of positive Lyapunov exponents. To distinguish the deterministic chaos from external noise, a reasonable amount of accurate data should be available. A successful verification of numerical results of the rather academic beam system by experiments would be an important step forward in the direction of industrial applications.

Appendix A

The effect of adding residual flexibility

In this appendix the positive effect of a residual flexibility mode on the accuracy of displacements and strains is shown by a simple example. Consider the 1D continuous system shown in figure A.1: The equation of motion of this system is given by the following partial differential equation:

$$\rho A \frac{\partial^2 q}{\partial t^2} + EA \frac{\partial^2 q}{\partial x^2} = F\delta(x - L)\cos(\omega t) \tag{A.1}$$

with boundary conditions:

$$q(0, t) = 0$$

The angular eigenfrequencies ω_k and eigenmodes φ_k, the solutions of the homogeneous part of (A.1), are ($k = \{1, 2, 3, \ldots, \infty\}$):

$$\omega_k = (2k - 1)\frac{\pi}{2L}\sqrt{\frac{E}{\rho}} \tag{A.2}$$

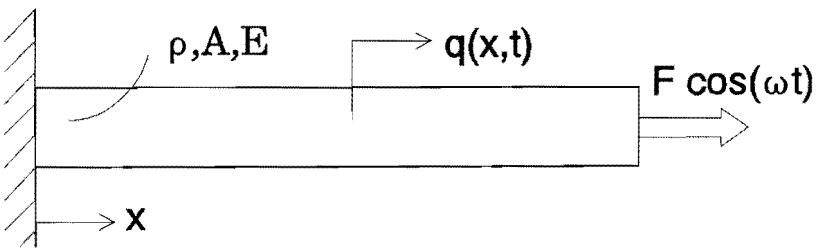

Figure A.1: Rod

$$\varphi_k(x) = \sin(\frac{(2k-1)\pi x}{2L}) \tag{A.3}$$

The static solution of (A.1) ($\omega = 0$), which can be identified with the flexibility mode of the system, is:

$$q(\tilde{x}, t) = \frac{FL}{EA}\tilde{x} \tag{A.4}$$

with:

$$\tilde{x} = x/L \tag{A.5}$$

The angular excitation frequency ω is expressed in terms of the first angular eigenfrequency ω_1:

$$\omega = \Omega\omega_1 \tag{A.6}$$

Solutions of (A.1) can be written in the form:

$$q(x, t) = \sum_{k=1}^{\infty} \varphi_k(x) p_k(t) \tag{A.7}$$

For steady-state solutions the functions $p_k(t)$ are:

$$p_k(t) = \frac{8}{\pi^2} \frac{(-1)^{k+1}}{(2k-1)^2 - \Omega^2} \frac{FL}{EA} \cos(\omega t) \tag{A.8}$$

Naturally, (A.7) is equal to (A.4) for $\Omega = 0$. Now three different 2-dof approximate solutions will be introduced. In the first approximation only the first two terms of (A.7) are kept:

$$q_1^s(\tilde{x}, t) = \frac{8}{\pi^2} \left[\frac{\sin(\frac{\pi\tilde{x}}{2})}{1-\Omega^2} - \frac{\sin(\frac{3\pi\tilde{x}}{2})}{9-\Omega^2} \right] \frac{FL}{EA} \cos(\omega t) \tag{A.9}$$

In the second approximation the second term between the brackets of (A.9) is replaced by the residual flexibility mode, defined as the flexibility mode (A.4) minus the contribution of the first eigenmode to the flexibility mode. So the second approximation becomes:

$$q_2^s(\tilde{x}, t) = \left[\tilde{x} + \frac{8}{\pi^2} \sin(\frac{\pi\tilde{x}}{2}) \frac{\Omega^2}{1-\Omega^2} \right] \frac{FL}{EA} \cos(\omega t) \tag{A.10}$$

Now the Rayleigh quotient is used to calculate an artificial angular eigenfrequency ω^* for the residual flexibility mode. Because the residual flexibility mode is a linear combination of all eigenmodes but the first, this artificial eigenfrequency will be greater than ω_2. The result is (compare with (A.2)):

$$\omega^* = \sqrt{\frac{12\pi^2 - 96}{\pi^4 - 96}} \frac{\pi}{2L} \sqrt{\frac{E}{\rho}} \approx 1.33\omega_2 \tag{A.11}$$

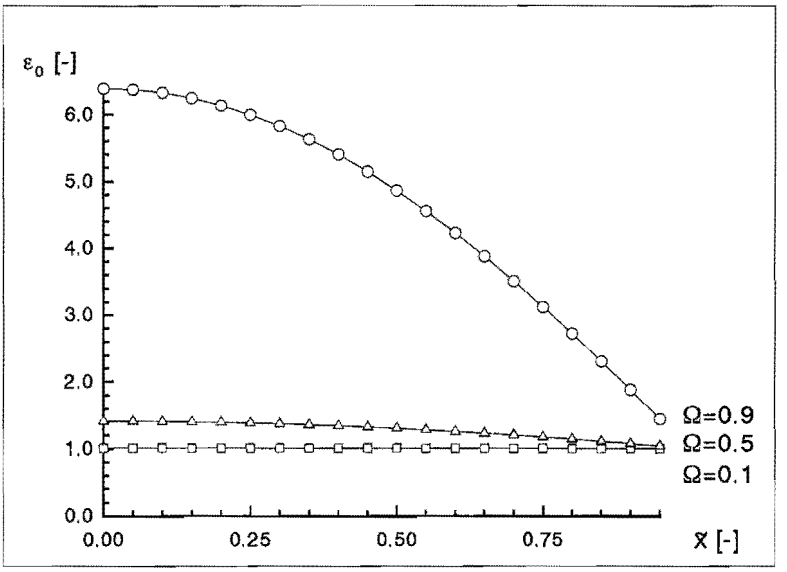

Figure A.2: Strains $\varepsilon_0(\tilde{x})$

Thus the third approximation is:

$$q_3^a(\tilde{x},t) = \left[\tilde{x} + \frac{8}{\pi^2}\sin(\frac{\pi\tilde{x}}{2})(\frac{1}{1-\Omega^2} - \frac{12\pi^2-96}{12\pi^2-96-(\pi^4-96)\Omega^2})\right]\frac{FL}{EA}\cos(\omega t) \quad (A.12)$$

Strains $\varepsilon(x,t)$, $\varepsilon_1^a(x,t)$, $\varepsilon_2^a(x,t)$ and $\varepsilon_3^a(x,t)$ are calculated by differentiation of (A.7), (A.9), (A.10) and (A.12) respectively to x. Now the following dimensionless functions are introduced (i=1,2,3):

$$q_0(\tilde{x}) = \frac{EA}{FL\cos(\omega t)}q(\tilde{x},t) \quad (A.13)$$

$$q_i(\tilde{x}) = \frac{EA}{FL\cos(\omega t)}q_i^a(\tilde{x},t) \quad (A.14)$$

$$\varepsilon_0(\tilde{x}) = \frac{EA}{FL\cos(\omega t)}\frac{dq(\tilde{x},t)}{d\tilde{x}} = \frac{EA}{FL\cos(\omega t)}\varepsilon(\tilde{x},t) \quad (A.15)$$

$$\varepsilon_i(\tilde{x}) = \frac{EA}{FL\cos(\omega t)}\frac{dq_i^a(\tilde{x},t)}{d\tilde{x}} = \frac{EA}{FL\cos(\omega t)}\varepsilon_i^a(\tilde{x},t) \quad (A.16)$$

Figure A.2 shows $\varepsilon_0(\tilde{x})$ (the upper bound for k is set to 100000). The relative errors in the dimensionless displacements and in the strains are defined as:

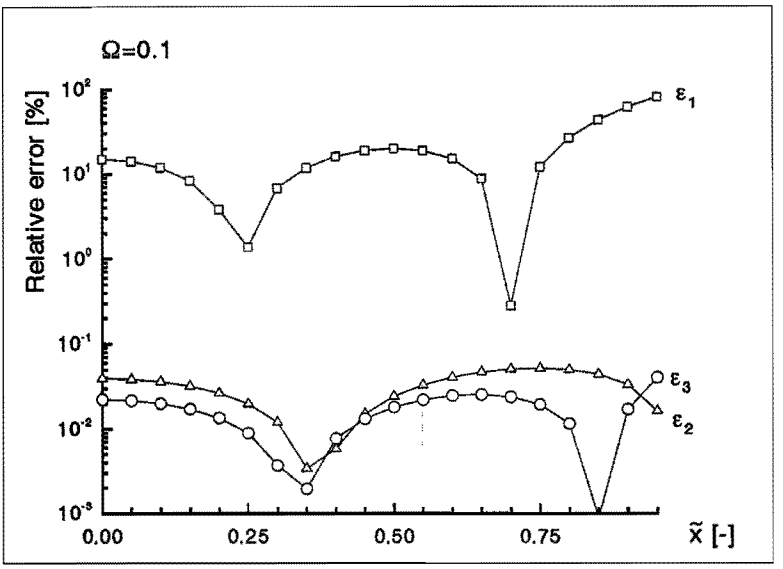

Figure A.3: Relative errors in strains for $\Omega = 0.1$

$$\frac{|q_i(\tilde{x}) - q_0(\tilde{x})|}{|q_0(\tilde{x})|} * 100\%$$

and:

$$\frac{|\varepsilon_i(\tilde{x}) - \varepsilon_0(\tilde{x})|}{|\varepsilon_0(\tilde{x})|} * 100\%$$

One might expect that the three different approximations would give accurate results for $0 \leqslant \Omega < 1$. Figures A.3-A.5 show the relative errors in the strains as a function of $\tilde{x}$ for three different values of Ω. The relative error in ε_1 becomes smaller if Ω approaches 1, where the contribution of the first eigenmode dominates. However, the relative errors in ε_1 near the point of application of the external force remain very large. This is due to the very slow convergence of the series, by which $\varepsilon_0(\tilde{x})$ is calculated, for $\tilde{x}$ close to 1. The relative errors in ε_2 and ε_3, which are zero for $\Omega = 0$, grow for increasing Ω, but remain smaller than the errors in ε_1, except for $\tilde{x} = 0.7$. The relative errors in ε_2 and ε_3 are much lower than the relative error in ε_1 for $\tilde{x}$ close to 1. This can be explained by the fact that in the calculation of the (residual) flexibility mode the series for $\varepsilon_0(\tilde{x})$ is calculated for $\Omega = 0$. The overall conclusion is that approximations $\varepsilon_2^a(\tilde{x}, t)$ and $\varepsilon_3^a(\tilde{x}, t)$ give better results than $\varepsilon_1^a(\tilde{x}, t)$, with $\varepsilon_3^a(\tilde{x}, t)$ slightly superior to $\varepsilon_2^a(\tilde{x}, t)$. Investigation of the relative errors in the three approximate displacement functions $q_i^a(\tilde{x}, t)$ leads to the same conclusion. For $\tilde{x}$ approaching to 1, however, no strong growth in the relative errors of the three approximate displacements is observed.

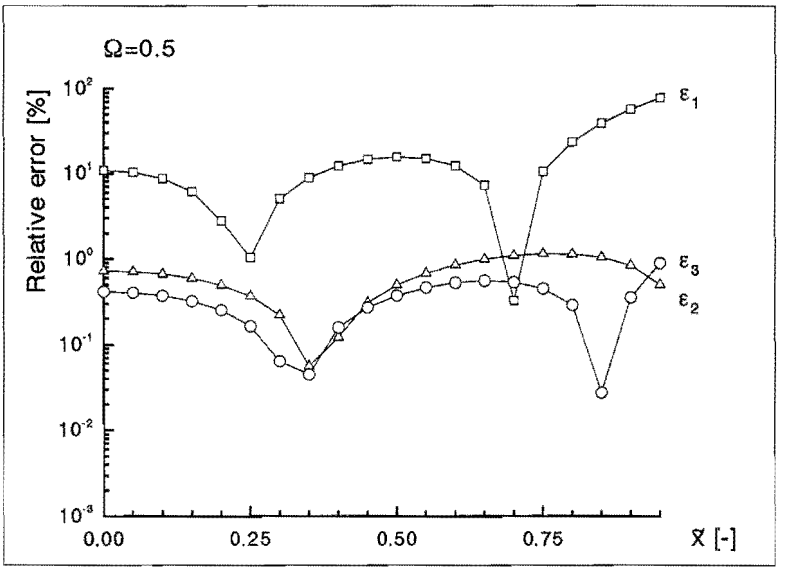

Figure A.4: Relative errors in strains for $\Omega = 0.5$

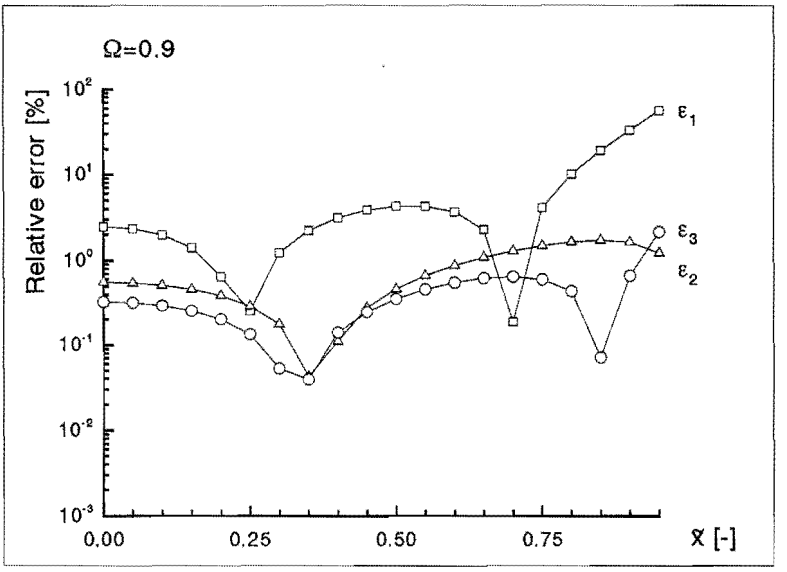

Figure A.5: Relative errors in strains for $\Omega = 0.9$

Appendix B

Alternative component modes

In this appendix alternative component mode sets are defined, which can also be used to compose a dynamic component mode set. For a definition of various sets of dofs one is referred to table 2.1.

B.1 Fixed-interface eigenmodes

Fixed-interface eigenmodes are calculated by solving the eigenvalue problem of the component with a suppressed $\mathcal{H}$ set:

$$(-(\omega_i^{fx})^2 M_{GG} + K_{GG})\varphi_{Gi}^{fx} = 0 \qquad i = 1, \ldots, n_G \qquad \text{(B.1)}$$

Fixed-interface eigenmodes are normalized on the mass matrix. The n_G angular eigenfrequencies ω_i^{fx} and corresponding fixed-interface eigenmodes φ_{Gi}^{fx} are stored in $\lceil\Omega^{fx}\rfloor$ and Φ_G^{fx} respectively. Fixed-interface eigenmodes with eigenfrequencies below the cut-off frequency f_c are stored columnwise in Φ_k^{fx}; the corresponding angular eigenfrequencies are stored on the diagonal of $\lceil\Omega_{kk}^{fx}\rfloor$. The remaining fixed-interface eigenmodes are stored columnwise in Φ_d^{fx}; the corresponding angular eigenfrequencies are stored on the diagonal of $\lceil\Omega_{dd}^{fx}\rfloor$:

$$\Phi^{fx} = \begin{bmatrix} \Phi_k^{fx} & \Phi_d^{fx} \end{bmatrix} = \begin{bmatrix} O_{Hk} & O_{Hd} \\ \Phi_{Gk}^{fx} & \Phi_{Gd}^{fx} \end{bmatrix} \qquad \text{(B.2)}$$

$$\lceil\Omega^{fx}\rfloor = \begin{bmatrix} \lceil\Omega_{kk}^{fx}\rfloor & O_{kd} \\ O_{dk} & \lceil\Omega_{dd}^{fx}\rfloor \end{bmatrix} \qquad \text{(B.3)}$$

B.2 Constraint modes

Constraint modes are defined for a set $\mathcal{C}$. A constraint mode is defined as the static displacement field which results as a unit displacement or -rotation is imposed on one of the dof in $\mathcal{C}$, whereas the other dof in $\mathcal{C}$ are suppressed. $\mathcal{C}$ will be chosen equal to $\mathcal{V}$ or $\mathcal{B}$. If $\mathcal{C}$ is equal to $\mathcal{V}$, $\mathcal{R}$ is suppressed and the matrix of (redundant) constraint modes Φ^{C1} is defined by:

$$\begin{bmatrix} K_{RR} & K_{RC} & K_{RI} \\ K_{CR} & K_{CC} & K_{CI} \\ K_{IR} & K_{IC} & K_{II} \end{bmatrix} \begin{bmatrix} O_{RC} \\ I_{CC} \\ \Phi_{IC} \end{bmatrix} = \begin{bmatrix} R_{RC} \\ R_{CC} \\ O_{IC} \end{bmatrix} \tag{B.4}$$

$$\Phi^{C1} = \begin{bmatrix} O_{RC} \\ I_{CC} \\ \Phi_{IC} \end{bmatrix} = \begin{bmatrix} O_{RC} \\ I_{CC} \\ -K_{II}^{-1} K_{IC} \end{bmatrix} \tag{B.5}$$

If C is equal to B the matrix of constraint modes Φ^{C2} is defined by:

$$\begin{bmatrix} K_{CC} & K_{CI} \\ K_{IC} & K_{II} \end{bmatrix} \begin{bmatrix} I_{CC} \\ \Phi_{IC} \end{bmatrix} = \begin{bmatrix} R_{CC} \\ O_{IC} \end{bmatrix} \tag{B.6}$$

$$\Phi^{C2} = \begin{bmatrix} I_{CC} \\ \Phi_{IC} \end{bmatrix} = \begin{bmatrix} I_{CC} \\ -K_{II}^{-1} K_{IC} \end{bmatrix} \tag{B.7}$$

B.3 Attachment modes

Attachment modes are defined for a set $\mathcal{A}$. An attachment mode is defined as the static displacement field which results, as one of the dof in $\mathcal{A}$ is loaded by a unit load, whereas the other dof in $\mathcal{A}$ are not loaded. The $\mathcal{R}$ set is suppressed. The $\mathcal{A}$ set is chosen equal to the $\mathcal{V}$ set. The matrix of attachment modes Φ^{A} is defined by:

$$\begin{bmatrix} K_{RR} & K_{RA} & K_{RI} \\ K_{AR} & K_{AA} & K_{AI} \\ K_{IR} & K_{IA} & K_{II} \end{bmatrix} \begin{bmatrix} O_{RA} \\ \Phi_{AA} \\ \Phi_{IA} \end{bmatrix} = \begin{bmatrix} R_{RA} \\ I_{AA} \\ O_{IA} \end{bmatrix} \tag{B.8}$$

$$\Phi^{A} = \begin{bmatrix} O_{RA} \\ \Phi_{AA} \\ \Phi_{IA} \end{bmatrix} = \begin{bmatrix} O_{RA} \\ (K_{AA} - K_{AI} K_{II}^{-1} K_{IA})^{-1} \\ -K_{II} K_{IA} (K_{AA} - K_{AI} K_{II}^{-1} K_{IA})^{-1} \end{bmatrix} \tag{B.9}$$

B.4 Inertia relief modes

If, given an initial state $s(t_0) = 0$, constant accelerations $\Phi_{RR} a_{RR}$ are prescribed for the $\mathcal{R}$ set for $t \geqslant t_0$, the total displacement of the component will be a linear combination of a rigid body displacement x_r and a quasi-static elastic displacement field x_e after transients have died out. The rigid body displacement will be a linear combination of the rigid body modes Φ^{R}; the quasi-static elastic displacement will be a linear combination of inertia relief modes Φ^{M}:

$$x = \begin{bmatrix} x_R \\ x_V \\ x_I \end{bmatrix} = x_r + x_e \tag{B.10}$$

$$x_r = \frac{1}{2}(t - t_0)^2 \Phi^R a_{RR} \tag{B.11}$$

$$\lim_{t\to\infty} x_e = \lim_{t\to\infty} \int_{t_0}^{t_0+t} \int_{t_0}^{t_0+\tau_1} \ddot{x}_e d(\tau_2 - t_0) d(\tau_1 - t_0) = \Phi^M a_{RR} = \begin{bmatrix} O_{RM} \\ \Phi_{VM} \\ \Phi_{IM} \end{bmatrix} a_{RR} \tag{B.12}$$

The number of independent inertia relief modes is equal to the number of rigid body modes. If transients are neglected ($\lim_{t\to\infty} \ddot{x}_e = \lim_{t\to\infty} \dot{x}_e = 0$) inertia relief modes Φ^M can be calculated by substituting (B.11) and (B.12) in (B.10) and substituting the result of this in (2.2):

$$\begin{bmatrix} K_{RR} & K_{RV} & K_{RI} \\ K_{VR} & K_{VV} & K_{VI} \\ K_{IR} & K_{IV} & K_{II} \end{bmatrix} \begin{bmatrix} O_{RM} \\ \Phi_{VM} \\ \Phi_{IM} \end{bmatrix} = - \begin{bmatrix} M_{RR} & M_{RV} & M_{RI} \\ M_{VR} & M_{VV} & M_{VI} \\ M_{IR} & M_{IV} & M_{II} \end{bmatrix} \Phi^R + \begin{bmatrix} R_{RR} \\ R_{VR} \\ O_{IR} \end{bmatrix} \tag{B.13}$$

R_{RR} are unknown loads necessary to prescribe accelerations Φ_{RR}. Inertia relief modes will always be accompanied by attachment modes or constraint modes in the Ritz reduction matrix. So an arbitrary choice of loads R_{VR} will not affect the linear subspace spanned by Φ^M and Φ^A or Φ^{C1}. The solution of (B.13) is given by:

$$\begin{bmatrix} \Phi_{VM} \\ \Phi_{IM} \end{bmatrix} = - \begin{bmatrix} \Phi_{AA} & -(K_{VV} - K_{VI}K_{II}^{-1}K_{IV})^{-1}K_{VI}K_{II}^{-1} \\ \Phi_{IA} & (K_{II} - K_{IV}K_{VV}^{-1}K_{VI})^{-1} \end{bmatrix} \left\{ \begin{bmatrix} M_{VR} & M_{VV} & M_{VI} \\ M_{IR} & M_{IV} & M_{II} \end{bmatrix} \Phi^R + \begin{bmatrix} R_{VR} \\ O_{IR} \end{bmatrix} \right\} \tag{B.14}$$

R_{VR} is chosen so that $\Phi_{VM} = O_{VM}$. The reason for this choice is that inertia relief modes now become orthogonal to Φ^A and Φ^{C1} with respect to the stiffness matrix. Finally, the matrix of inertia relief modes Φ^M becomes:

$$\Phi^M = \begin{bmatrix} O_{RM} \\ O_{VM} \\ \Phi_{IM} \end{bmatrix} = \begin{bmatrix} O_{RM} \\ O_{VM} \\ -K_{II}^{-1} \begin{bmatrix} M_{IR} & M_{IV} & M_{II} \end{bmatrix} \Phi^R \end{bmatrix} \tag{B.15}$$

Appendix C

The dimensionless nonlinear single dof model

Consider a linear, undamped component with dof x:

$$x = \begin{bmatrix} x_I \\ x_B \end{bmatrix} \tag{C.1}$$

x_B is a boundary dof, which is loaded by an external load f_{ex} and internal loads $f_{nl}(\dot{x}_B, x_B)$ caused by adjacent local nonlinearities. The dof x_I are not loaded. The equations of motion of the system are:

$$M\ddot{x} + K\dot{x} = [\ 0_I^t,\ \ f_{ex} - f_{nl}(\dot{x}_B, x_B)\ ]^t \tag{C.2}$$

The displacement field of the linear component is approximated by a single mode φ:

$$x = \begin{bmatrix} x_I \\ x_B \end{bmatrix} = \begin{bmatrix} \varphi_I \\ \varphi_B \end{bmatrix} p = \begin{bmatrix} \varphi_I/\varphi_B \\ 1 \end{bmatrix} x_B \tag{C.3}$$

Using this transformation the equations of motion can be reduced to the following single dof model based on dof $q = x_B$:

$$m\ddot{q} + kq = f_{ex} - f_{nl}(\dot{q}, q) \tag{C.4}$$

with:

$$m = \frac{\varphi^t M \varphi}{\varphi_B^2}$$

$$k = \frac{\varphi^t K \varphi}{\varphi_B^2}$$

Assume that the local nonlinearities consist of a spring with cubic stiffness k_3, a one-sided linear spring with stiffness k_p and a one-sided spring with cubic stiffness k_{3p}. Furthermore dof q is internally loaded by a linear viscous damper with damping constant b and externally loaded by a harmonic load with amplitude F_{dy} and frequency f_e. Then the resulting equation of motion of the single dof system is given by:

$$m\ddot{q} + b\dot{q} + kq + k_s q^3 + \sigma(q)(k_p q + k_{3p} q^3) = F_{dy}\cos(2\pi f_e t) \tag{C.5}$$

with:

$$\sigma(q) = \begin{cases} 0 & \text{if } q \geqslant 0 \\ 1 & \text{if } q < 0 \end{cases}$$

In this equation ten quantities are involved. Three quantities can be eliminated by making equation (C.5) dimensionless. Hereto the dimensionless displacement ζ and the dimensionless time θ (not to be confused with the dimensionless time τ introduced in (3.2)) are introduced:

$$q = \frac{F_{dy}}{k}\zeta \tag{C.6}$$

$$t = \theta\sqrt{\frac{m}{k}} \tag{C.7}$$

Substitution of (C.6) and (C.7) in (C.5) followed by division by F_{dy} results in the dimensionless equation of motion ($' = d/d\theta$):

$$\zeta'' + 2\xi\zeta' + \zeta + \mu\zeta^3 + \sigma(\zeta)(\alpha\zeta + \mu_p\zeta^3) = \cos(\Omega\theta) \tag{C.8}$$

and the 5 dimensionless parameters:

$$\xi = \frac{b}{2\sqrt{mk}} \tag{C.9}$$

$$\mu = \frac{k_s F_{dy}^2}{k^3} \tag{C.10}$$

$$\alpha = \frac{k_p}{k} \tag{C.11}$$

$$\mu_p = \frac{k_{3p} F_{dy}^2}{k^3} \tag{C.12}$$

$$\Omega = 2\pi f_e\sqrt{\frac{m}{k}} \tag{C.13}$$

Appendix D

The structure of the Jacobian

After the application of the central difference scheme (3.8), (3.9) with a consistency of $0(\triangle\tau^2)$, in (3.24),(3.36),(3.43) and (3.50)-(3.51) equations must be solved of the type:

$$\frac{\partial h}{\partial z}a = b \tag{D.1}$$

Equation (D.1) can be solved efficiently using the special structure of the Jacobian $J = \partial h/\partial z$. If a, b and J are partitioned like z in the following equations:

$$z = \begin{bmatrix} z_\alpha \\ z_\beta \end{bmatrix}$$

$$z_\alpha = [q_0^t, \ldots, q_{\mathrm{n}_\tau-2}^t]^t$$

$$z_\beta = q_{\mathrm{n}_\tau-1}$$

the upper left block of the Jacobian $J_{\alpha\alpha}$ will have a bandstructure with a bandwidth $\mathrm{b}_J = 2\mathrm{n}_q - 1$ and the solution of (D.1) can be calculated with:

$$a_\beta = (J_{\beta\beta} - J_{\beta\alpha}J_{\alpha\alpha}^{-1}J_{\alpha\beta})^{-1}(b_\beta - J_{\beta\alpha}J_{\alpha\alpha}^{-1}b_\alpha) \tag{D.2a}$$

$$a_\alpha = J_{\alpha\alpha}^{-1}(b_\alpha - J_{\alpha\beta}a_\beta) \tag{D.2b}$$

The CPU-time, needed for decomposing $J_{\alpha\alpha}$, is approximately proportional to $(\mathrm{n}_\tau - 1) * \mathrm{n}_q * (2\mathrm{b}_J + 1)^2$, whereas the CPU-time, needed for the decomposition of J is approximately proportional to $(\mathrm{n}_\tau * \mathrm{n}_q)^3$, see the description of routine F01LBF of the NAG library [1989]

.

If the central difference scheme (3.38), (3.39) is used with a consistency of $0(\triangle\tau^4)$, z_α and z_β must be defined as:

$$z_\alpha = [q_0^t, \ldots, q_{\mathrm{n}_\tau-3}^t]^t$$

$$z_\beta = [q_{\mathrm{n}_\tau-2}^t, q_{\mathrm{n}_\tau-1}^t]^t$$

to realize a bandstructure for $J_{\alpha\alpha}$. The bandwidth of $J_{\alpha\alpha}$ now becomes $\mathrm{b}_J = 3\mathrm{n}_q - 1$.

Appendix E

The method of harmonic balance

The method of harmonic balance (Jordan and Smith [1977]) is an analytical/numerical method, by which estimates of periodic solutions of nonlinear dynamic systems in closed form can be obtained. Here the method is applied to estimate the harmonic and 1/3 subharmonic solutions of the single dof Duffing system:

$$\zeta'' + 2\xi\zeta' + \zeta + \mu\zeta^3 = \cos(\Omega\theta) \tag{E.1}$$

The harmonic solution is assumed to be of the form:

$$\zeta(\theta) = c_1\cos(\Omega\theta) + s_1\sin(\Omega\theta) + c_3\cos(3\Omega\theta) + s_3\sin(3\Omega\theta) \tag{E.2}$$

Substitution of this expression in (E.1) gives:

$$\begin{aligned} &C_1(\xi,\Omega,\mu,c_1,s_1,c_3,s_3)\cos(\Omega\theta) + S_1(\xi,\Omega,\mu,c_1,s_1,c_3,s_3)\sin(\Omega\theta) + \\ &C_3(\xi,\Omega,\mu,c_1,s_1,c_3,s_3)\cos(3\Omega\theta) + S_3(\xi,\Omega,\mu,c_1,s_1,c_3,s_3)\sin(3\Omega\theta) = \\ &\mu C_H(c_1,s_1,c_3,s_3,\cos(5\Omega\theta),\sin(5\Omega\theta),\cos(7\Omega\theta),\sin(7\Omega\theta),\cos(9\Omega\theta),\sin(9\Omega\theta)) \end{aligned} \tag{E.3}$$

This equation must be satisfied for all θ. This implies, neglecting the right hand side of (E.3), that the functions C_1, S_1, C_3 and S_3 must be equal to zero:

$$\begin{aligned} C_1 &= c_1 + 2\xi\Omega s_1 - \Omega^2 c_1 + \\ &\quad (\mu/4)(3c_1^2(c_1+c_3) + 3s_1^2(c_1-c_3) + 6c_1(c_3^2+s_3^2+s_1s_3)) - 1 = 0 && \text{(E.4a)} \\ S_1 &= s_1 - 2\xi\Omega c_1 - \Omega^2 s_1 + \\ &\quad (\mu/4)(3c_1^2(s_1+s_3) + 3s_1^2(s_1-s_3) + 6s_1(c_3^2+s_3^2-c_1c_3)) = 0 && \text{(E.4b)} \\ C_2 &= c_3 + 6\xi\Omega s_3 - 9\Omega^2 c_3 + \\ &\quad (\mu/4)(c_1^3 + 3c_3^3 + 6c_1^2c_3 - 3s_1^2c_1 + 6s_1^2c_3 + 3s_3^2c_3) = 0 && \text{(E.4c)} \\ S_2 &= s_3 - 6\xi\Omega c_3 - 9\Omega^2 s_3 + \\ &\quad (\mu/4)(-s_1^3 + 3s_3^3 + 3c_1^2s_1 + 6c_1^2s_3 + 6s_1^2s_3 + 3c_3^2s_3) = 0 && \text{(E.4d)} \end{aligned}$$

This set of nonlinear, algebraic equations can be solved numerically for c_1, s_1, c_3 and s_3. For values of Ω far away from resonance (E.4) has one (stable) solution ($\xi \neq 0$). For appropriate values of ξ and μ equations (E.4) can have three solutions for $\Omega \downarrow 1$ (near harmonic

resonance) and $\Omega \downarrow 1/3$ (near superharmonic resonance). Two of these solutions are stable and one is unstable.

In an analogous way an estimate of the 1/3 subharmonic solution can be obtained, which is assumed to be of the form:

$$\zeta(\theta) = c_{1/3}\cos(\Omega\theta/3) + s_{1/3}\sin(\Omega\theta/3) + c_1\cos(\Omega\theta) + s_1\sin(\Omega\theta) \tag{E.5}$$

This leads to the following set of equations:

$$\begin{aligned}
C_1 &= c_{1/3} + 2\xi\Omega s_{1/3}/3 - \Omega^2 c_{1/3}/9 + \\
&\quad (\mu/4)(3c_{1/3}^2(c_{1/3}+c_1) + 3s_{1/3}^2(c_{1/3}-c_1) + 6c_{1/3}(c_1^2+s_1^2+s_{1/3}s_1)) = 0 \quad \text{(E.6a)} \\
S_1 &= s_{1/3} - 2\xi\Omega c_{1/3}/3 - \Omega^2 s_{1/3}/9 + \\
&\quad (\mu/4)(3c_{1/3}^2(s_{1/3}+s_1) + 3s_{1/3}^2(s_{1/3}-s_1) + 6s_{1/3}(c_1^2+s_1^2-c_{1/3}c_1)) = 0 \quad \text{(E.6b)} \\
C_2 &= c_1 + 2\xi\Omega s_1 - \Omega^2 c_1 + \\
&\quad (\mu/4)(c_{1/3}^3 + 3c_1^3 + 6c_{1/3}^2 c_1 - 3s_{1/3}^2 c_{1/3} + 6s_{1/3}^2 c_1 + 3s_1^2 c_1) - 1 = 0 \quad \text{(E.6c)} \\
S_2 &= s_1 - 2\xi\Omega c_1 - \Omega^2 s_1 + \\
&\quad (\mu/4)(-s_{1/3}^3 + 3s_1^3 + 3c_{1/3}^2 s_{1/3} + 6c_{1/3}^2 s_1 + 6s_{1/3}^2 s_1 + 3c_1^2 s_1) = 0 \quad \text{(E.6d)}
\end{aligned}$$

Note that the choice $c_{1/3} = s_{1/3} = 0$ solves the first two equations of (E.6), but will lead to an estimate of a harmonic solution instead of a 1/3 subharmonic solution. Usually equations (E.6) only have two solutions with $c_{1/3} \neq 0$ and/or $s_{1/3} \neq 0$ for $\Omega > 3$ (near subharmonic resonance). These solutions have opposite stability. However, it is also possible that there exist no subharmonic solutions for any Ω.

In figure E.1 solutions (E.2) and (E.5) are compared with solutions obtained with the numerical methods described in chapter 3. The results are comparative ($\mu = 0.05$, $\xi = 0.003$, $\Omega = 0 - 6$, $f_e = 8.9592\Omega$, $y = 0.006\zeta$).

In general, the solutions obtained above will be accurate only for $\mu \ll 1$. For $\mu = o(1)$ many more superharmonic terms must be added to (E.2) and (E.5) in order to get an accurate solution. It is clear that in this case, but also in the case of more dof, the method of harmonic balance becomes cumbersome.

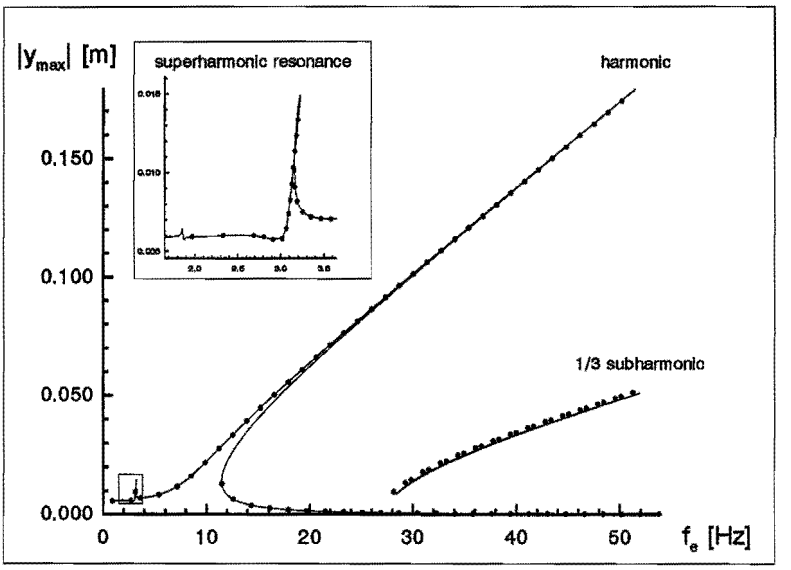

Figure E.1: Comparison between analytical (dots) and numerical results (lines)

Bibliography

E.L. Allgower. A survey of homotopy methods for smooth mappings. In Glashoff Allgower and Peitgen, editors, *Numerical Solutions of Nonlinear Equations*, pages 1–29, Springer-Verlag, 1981.

ASKA Saab-Scania/Ikoss User's Manual. 1986.

Klaus-Jürgen Bathe. *Finite Element Procedures in Engineering Analysis.* Prentice-Hall, 1982.

Klaus-Jürgen Bathe and Sheryl Gracewski. On nonlinear dynamic analysis using substructuring and mode superposition. *Computers & Structures*, 13:699–707, 1981.

W.A. Benfield and R.F. Hruda. Vibration analysis of substructures by component mode substitution. *AIAA Journal*, 9(7):1255–1261, July 1971.

T.D. Burton. A perturbation method for certain non-linear oscillators. *Int. J. Non-Linear Mechanics*, 19(5):397–407, 1984.

T.D. Burton and M.N. Hamdan. Analysis of non-linear autonomous conservative oscillators by a time transformation method. *Journal of Sound and Vibration*, 87(4):543–554, 1983.

T.D. Burton and Z. Rahman. On the multi-scale analysis of strongly non-linear forced oscillators. *Int. J. Non-Linear Mechanics*, 21(2):135–146, 1986.

C.J. Chang. *A General Procedure for Substructure Coupling in Dynamic Analysis.* PhD thesis, University of Texas, Austin, December 1977.

S.H. Chen, Y.K. Cheung, and S.L. Lau. On the internal resonance of multi-degree-of-freedom systems with cubic non-linearity. *Journal of Sound and Vibration*, 128(1):13–24, 1989.

Roy R. Craig, Jr. A review of time-domain and frequency-domain component mode synthesis methods. In David R. Martinez and A. Keith Miller, editors, *Combined Experimental/Analytical Modeling of Dynamic Structural Systems Using Substructure Synthesis*, pages 1–31, June 1985.

Roy R. Craig Jr. and Mervin C.C. Bampton. Coupling of substructures for dynamic analyses. *AIAA Journal*, 6(7):1313–1319, July 1968.

M.T.M. Crooijmans. *On the Computation of Stationary Deterministic Behaviour of Non-Linear Dynamic Systems with Applications to Rotor-Bearing Structures.* PhD thesis, Eindhoven University of Technology, 1987.

Mitchell J. Feigenbaum. Universal behavior in nonlinear systems. *Physica*, 7D:16–39, 1983.

R.H.B. Fey, A. de Kraker, D.H. van Campen, and G.J. Meijer. Stable and unstable periodic solutions of reduced dynamic systems with local nonlinearities. In J.F. Dijksman and F.T.M. Nieuwstadt, editors, *Integration of Theory and Applications in Applied Mechanics*, pages 247–254, April 1990.

Isaac Fried. Orthogonal trajectory accession to the nonlinear equilibrium curve. *Computer Methods in Applied Mechanics and Engineering*, 47:283–297, 1984.

John Guckenheimer and Philip Holmes. *Nonlinear Oscillations, Dynamical Systems, and Bifurcations of Vector Fields. Applied Mathematical Sciences 42*, Springer-Verlag, 1983.

H. Haken. At least one Lyapunov exponent vanishes if the trajectory of an attractor does not contain a fixed point. *Phys. Lett.*, 94A:71, 1983.

G. Hall and J.M. Watt. *Modern Numerical Methods for Ordinary Differential Equations.* Oxford, 1976.

D.N. Herting. A general purpose, multi-stage, component modal synthesis method. *Finite Elements in Analysis and Design*, 1:153–164, 1985.

Robert Morris Hintz. Analytical methods in component modal synthesis. *AIAA Journal*, 13(8):1007–1016, August 1975.

C.S. Hsu. A generalized theory of cell-to-cell mapping of nonlinear dynamical systems. *Journal of Applied Mechanics*, 48:634–642, September 1981.

C.S. Hsu. A theory of cell-to-cell mapping dynamical systems. *Journal of Applied Mechanics*, 47:931–939, December 1980.

C.S. Hsu and R.S. Guttalu. An unravelling algorithm for global analysis of dynamical systems: an application of cell-to-cell mappings. *Journal of Applied Mechanics*, 47:940–948, December 1980.

Walter C. Hurty. Dynamic analysis of structural systems using component modes. *AIAA Journal*, 3(4):678–685, April 1965.

D.W. Jordan and P. Smith. *Nonlinear Ordinary Differential Equations.* Oxford University Press, 1977.

J.L. Kaplan and J.A. Yorke. Chaotic behavior of multidimensional difference equations. In Heinz-Otto Peitgen and Hans-Otto Walther, editors, *Functional Differential Equations and Approximation of Fixed Points*, pages 204–227, July 1978.

A. de Kraker, R.H.B. Fey, D.H. van Campen, and C.J. Langeveld. Some aspects of the analysis of systems with local nonlinearities. In W. Schiehlen, editor, *Nonlinear Dynamics in Engineering Systems*, pages 165–172, IUTAM, Springer-Verlag, August 1989.

Anant R. Kukreti and Hadi I. Issa. Dynamic analysis of nonlinear structures by pseudo-normal mode superposition method. *Computers & Structures*, 19(4):653–663, 1984.

LMS CADA X User's Manual. 1990.

Richard H. Macneal. A hybrid method of component mode synthesis. *Computers & Structures*, 1:581–601, 1971.

R.M.M. Mattheij. Decoupling and stability of algorithms for boundary value problems. *SIAM Review*, 27(1):1–44, March 1985.

Nicholas F. Morris. The use of modal superposition in nonlinear dynamics. *Computers & Structures*, 7:65–72, 1977.

P.C. Müller and W.O. Schiehlen. *Linear Vibrations. Mechanics: Dynamical Systems*, Martinus Nijhoff Publishers, 1985.

NAG Fortran Library. mark 13 edition, 1989.

S. Natsiavas. On the dynamics of oscillators with bi-linear damping and stiffness. *Int. J. Non-Linear Mechanics*, 25(5):535–554, 1990.

Ali H. Nayfeh and Dean T. Mook. *Nonlinear Oscillations.* John Wiley & Sons Ltd., 1979.

S. Newhouse, D. Ruelle, and F. Takens. Occurence of strange axiom-a attractors near quasi-periodic flow on T^m, $m \leqslant 3$. *Commun. Math. Phys.*, 64:35–40, 1978.

R.E. Nickell. Nonlinear dynamics by mode superposition. *Computer Methods in Applied Mechanics and Engineering*, 7:107–129, 1976.

Victor Pereyra. On improving an approximate solution of a functional equation by deferred corrections. *Numerische Mathematik*, 8:376–391, 1966.

Y. Pomeau and P. Manneville. Intermittent transition to turbulence in dissipative dynamical systems. *Commun. Math. Phys.*, 74:189–197, 1980.

S.N. Remseth. Nonlinear static and dynamic analysis of framed structures. *Computers & Structures*, 10:879–897, 1979.

Werner C. Rheinboldt. Numerical methods for a class of finite dimensional bifurcation problems. *SIAM J. Numer. Anal.*, 15(1):1–11, February 1978.

J. Schouten. *Steady-State Gedrag van een Opgelegde Balk met Niet-lineaire Ondersteuning.* Master's thesis, Eindhoven University of Technology, August 1991. In Dutch.

Heinz Georg Schuster. *Deterministic Chaos: An Introduction.* VCH Publishers, 1989.

Rüdiger Seydel. *From Equilibrium to Chaos, Practical Bifurcation and Stability Analysis.* Elsevier Science Publishing Co., Inc., 1988.

V.N. Shah, G.J. Bohm, and A.N. Nahavandi. Modal superposition method for computationally economical nonlinear structural analysis. *Journal of Pressure Vessel Technology*, 101:134–141, May 1979.

Jinsiang Shaw, Steven W. Shaw, and Alan G. Haddow. On the response of the nonlinear vibration absorber. *Int. J. Non-Linear Mechanics*, 24(4):281–293, 1989.

S.W. Shaw and P.J. Holmes. A periodically forced piecewise linear oscillator. *Journal of Sound and Vibration*, 90(1):129–155, 1983.

Gustaf Söderlind and Robert M.M. Mattheij. Stability and asymptotic estimates in nonautonomous linear differential systems. *SIAM J. Math. Anal.*, 16(1):69–92, January 1985.

J.J. Stoker. *Nonlinear Vibrations.* Interscience Publishers, 1966.

James A. Stricklin and Walter E. Haisler. Formulations and solution procedures for nonlinear structural analysis. *Computers & Structures*, 7:125–136, 1977.

J.M.T. Thompson and H.B. Stewart. *Nonlinear Dynamics and Chaos.* John Wiley & Sons Ltd., 1986.

Benson H. Tongue. Calculation of stability characteristics through interpolated mapping. In W. Schiehlen, editor, *Nonlinear Dynamics in Engineering Systems*, pages 321–328, IUTAM, Springer-Verlag, August 1989.

Yoshihiro Tsuda, Junkichi Inoue, Hideyuki Tamura, and Atsuo Sueoka. On the 1/2-th subharmonic vibrations of a non-linear vibrating system with a hard duffing type restoring characteristic. *Bulletin of the JSME*, 27(228):1280–1287, June 1984.

P. van der Varst. *On the Normal Mode Vibrations of Nonlinear Conservative Systems.* PhD thesis, Eindhoven University of Technology, 1982.

Alan Wolf, Jack B. Swift, Harry L. Swinney, and John A. Vastano. Determining Lyapunov exponents from a time series. *Physica*, 16D:285–317, 1985.

The author wishes to acknowledge his appreciation to TNO Building and Construction Research for the financial support of this project, to all who contributed to the research and to all who assisted in the preparation of this thesis.

Levensbericht

17-3-1964	Geboren te Eindhoven
1976-1982	Gymnasium β aan het Van der Puttlyceum te Eindhoven
1982-1987	Studie Werktuigbouwkunde aan de Technische Universiteit Eindhoven
1987-1992	Assistent in Opleiding aan de Technische Universiteit Eindhoven, faculteit Werktuigbouwkunde

STELLINGEN

behorende bij het proefschrift

STEADY-STATE BEHAVIOUR OF REDUCED DYNAMIC SYSTEMS WITH LOCAL NONLINEARITIES

1. Het ontbreken van numerieke algoritmen voor het gedeeltelijk oplossen van eigenwaardeproblemen, waarbij het imaginaire deel van de eigenwaarde fungeert als selectiecriterium, is een gemis bij de ontwikkeling van reductietechnieken voor lineaire, algemeen gedempte dynamische systemen met veel vrijheidsgraden.

2. Indien de periodetijd van een periodieke oplossing van een dynamisch systeem groter is dan de gebruiksduur van het dynamische systeem, kan deze oplossing vanuit praktisch oogpunt chaotisch genoemd worden.

   - H.W. Broer en F. Takens. Wegen naar chaos en vreemde aantrekking. In H.W. Broer en F. Verhulst (red.), *Dynamische Systemen en Chaos, een revolutie uit de wiskunde*, Epsilon Uitgaven, Utrecht 1990.

3. In zijn onderzoek naar subharmonische oplossingen van orde 1/3 van een zwak gedempte, sterk niet-lineaire Duffing vergelijking stelt Riganti dat de tak met de maximale amplitude instabiel en de tak met minimale amplitude stabiel is. Dit is niet correct voor excitatiefrequenties nabij het linker cyclic fold bifurcatiepunt.

   - R. Riganti. Subharmonic solutions of the Duffing equation with large nonlinearity. *Int. J. Non-Linear Mechanics*, Vol. 13, No. 1, pp. 21-31, 1978.
   - Dit proefschrift, hoofdstuk 7.

4. Door veel auteurs wordt de term Hopf-bifurcatie oneigenlijk gebruikt voor de bifurcatie van een periodieke naar een quasi-periodieke oplossing, terwijl de eigenlijke betekenis de bifurcatie van een statisch evenwicht naar een periodieke oplossing is.

   - E. Hopf. Abzweigung einer periodischen Lösung von einer stationären Lösung eines Differentialsystems. *Ber. Math.-Phys. Klasse Sachs. Akad. Wiss. Leipzig*, Vol. 94, pp. 1-22, 1942.
   - S. Natsiavas. On the dynamics of oscillators with bi-linear damping and stiffness. *Int. J. Non-Linear Mechanics*, Vol. 25, No. 5, pp. 535-554, 1990.

5. De vraag "Kunt u toepassingen geven van de chaos-theorie in de praktijk ?" zal in de toekomst steeds minder gesteld worden, mede dankzij de multidisciplinaire toepasbaarheid van deze theorie.

   - J.M.T. Thompson. Chaotic dynamics and the Newtonian legacy. *Appl. Mech. Rev.*, Vol. 42, No. 1, pp. 15-24, 1989.

6. Bij de uitvoering van een naar de plaats gediscretiseerde berekening is het vaak mogelijk om op basis van fysisch inzicht vooraf te bepalen, waar een meshverfijning noodzakelijk zal zijn, ter verkrijging van resultaten met een zekere nauwkeurigheid. Bij de uitvoering van een naar de tijd gediscretiseerde berekening ter bepaling van periodieke oplossingen is dit veel minder vaak het geval.

7. Hoe hoger de codimensie van een bifurcatie is, des te lager is zijn praktische relevantie.

8. Deskundigheid op het gebied van onderzochte niet-lineaire dynamische fenomenen gaat vooraf aan deskundigheid op het gebied van de niet-lineaire dynamica.

9. De numerieke methoden voor het analyseren van het lange termijn gedrag van een niet-lineair dynamisch systeem vallen slechts ten dele te automatiseren.

10. Het met een te hoog adrenalinegehalte in het bloed besturen van een auto kan net zo onverantwoord zijn als het met een te hoog alcoholpromillage in het bloed besturen van een auto.

11. De taak van de coach van een jeugdig sportteam bestaat niet alleen uit het leren winnen van wedstrijden, maar ook uit het leren verliezen van wedstrijden.

Eindhoven, oktober 1991 Rob Fey